Lawrence Berkeley Laboratory

UNIVERSITY OF CALIFORNIA

Accelerator & Fusion Research Division

$Cs^+ + Cs^+$ CHARGE TRANSFER AND IONIZATION CROSS SECTION MEASUREMENTS BY A PLASMA TARGET TECHNIQUE

Kenneth Reed Stalder
(Ph.D. thesis)

May 1982

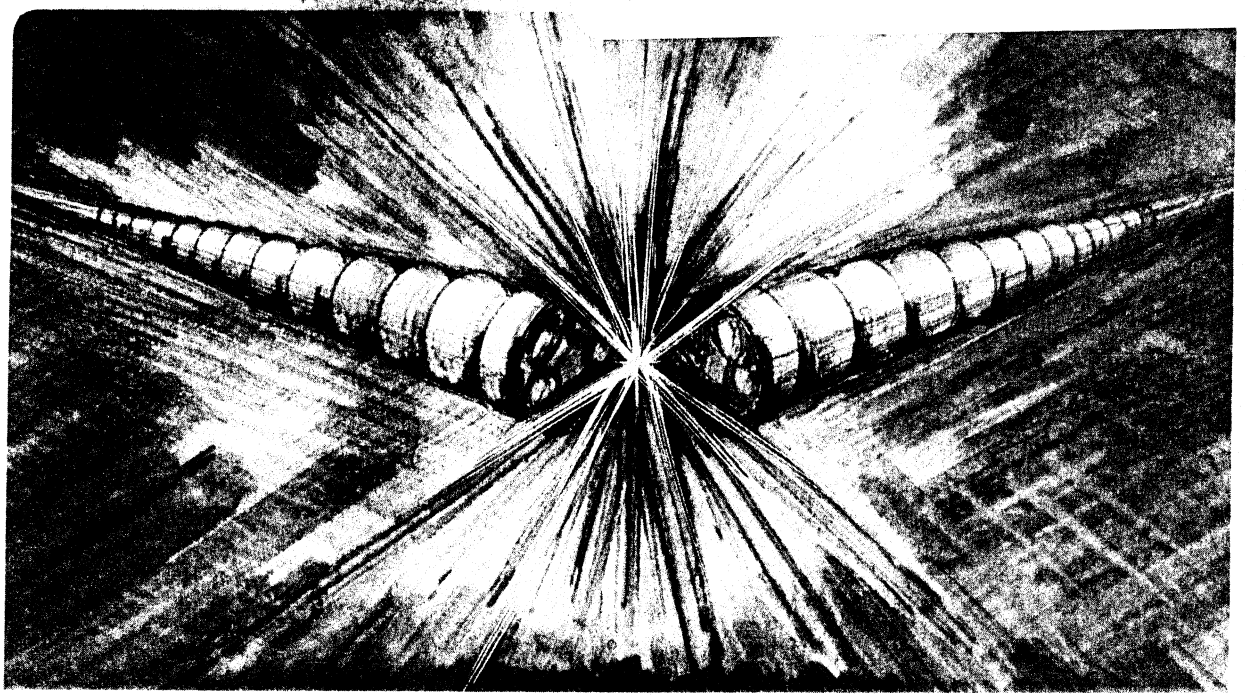

Prepared for the U.S. Department of Energy under Contract DE-AC03-76SF00098

LBL-14487

$Cs^+ + Cs^+$ CHARGE TRANSFER AND IONIZATION CROSS SECTION MEASUREMENTS BY A PLASMA TARGET TECHNIQUE*

Kenneth Reed Stalder

Ph.D. Thesis

Lawrence Berkeley Laboratory
University of California
Berkeley, CA 94720

May 1982

---

* This work was supported, in part by a grant from the Director's Program Development Fund, Lawrence Berkeley Laboratory, and by the Director, Office of Fusion Energy, Applied Plasma Physics Division of the U.S. Department of Energy under Contract No. DE-AC03-76SF00098.

$Cs^+ + Cs^+$ CHARGE TRANSFER AND IONIZATION CROSS SECTION MEASUREMENTS BY A PLASMA TARGET TECHNIQUE*

Kenneth Reed Stalder

Ph.D. Thesis

Lawrence Berkeley Laboratory
University of California
Berkeley, CA 94720

May 1982

ABSTRACT

Ion-ion collisions relevant to the heavy-ion fusion program have been studied by a plasma target technique. These collisions may limit the allowable storage times for high energy beams in storage rings. If ion-ion collisions lead to charge-changed product ions then the lost ions will lead to lost beam intensity and perhaps damage to beamlines. The interaction of desorbed wall material with the beam might catastrophically disrupt the beam.

Cs^+ is a candidate for a driver in a heavy-ion fusion reactor. Therefore a study of $Cs^+ + Cs^+$ collisions were undertaken in this thesis to determine the cross section for charge transfer and ionization. The range of center of mass energies for these collisions were from 50-110 keV.

A Q machine plasma target using cesium was constructed to serve as a target for a beam of Cs^+ ions. The sum of charge transfer and ionization cross sections was determined by measuring the growth of the Cs^{++} component of the beam as a function of the plasma radial line density. The measured cross section varies approxi-

mately linearly with energy between 50 and 110 keV. This loss cross section is $0.47 \pm .11 \times 10^{-16}$ cm^2 at 50 keV and rises to $1.87 \pm .18 \times 10^{-16} cm^2$ at 110 keV. These results have been compared to the cross section determined by a crossed-beam technique. The agreement between the results of the experiments is good at energies above 75 keV. A discrepancy between the results at lower energies indicated a systematic error in one of the techniques. Theoretical estimates of the cross section recently have begun to agree with the magnitude of the cross section but have not fully explained the energy dependence.

Plasma targets may also be useful as a neutralizer for intense D^- beams for advanced neutral beam injection for magnetic confinement. The Q machine plasma target was investigated as a candidate for neutralization studies but was not used due to small target densities and beam dispersion problems.

R. V. Pyle
Committee Chairman

$Cs^+ + Cs^+$ CHARGE TRANSFER AND IONIZATION CROSS SECTION MEASUREMENTS BY A PLASMA TARGET TECHNIQUE*

Table of Contents

10. Appendices

DEDICATION

To my mother, Virginia

ACKNOWLEDGMENTS

The undertaking of a Ph.D. thesis requires a lot of work and necessitates working with many individuals. I am grateful for the help that most of my acquaintences have given me. Those that have been most helpful include the following: I wish to thank Dr. Klaus H. Berkner for suggesting this problem and maintaining a keen interest until completion. My thesis advisor, Prof. Robert V. Pyle, deserves special thanks for supporting me through this project. His advice was particularly good at the times when I was stuck for new ideas to try.

Staff scientists usually had many good suggestions. Dr. W. F. Steele was extremely helpful with the computer system. Drs. W. G. Graham, D. J. Markevich, R. H. McFarland, A. S. Schlachter and J. A. Tanis and Mr. J. W. Stearns were good sources of useful criticism at times.

Student colleagues were very helpful in maintaining a good working environment as well as actually helping out in some of the experimental measurements. These include John Trow, Gen Wada and Jon Bechtel.

The shop personnel were very helpful in constructing a lot of the experimental equipment. My sincere thanks to Harlan Hughes, Harvey Owren and Lou Biagi probably is insufficient praise for the fine work done in their shops.

The secretarial staff led by Ms. Augustine Aitkens always were appreciated for their conscientious work. I thank them for typing this thesis.

Finally, I would like to thank my wife, Patricia, for her support and understanding during the last stages of this project. My entire family and set of close friends always were supportive and this gave me a lot of confidence to complete the work.

This work was supported, in part by a grant from the Director's Program Development Fund, Lawrence Berkeley Laboratory, and by the Director, Office of Fusion Energy, Applied Plasma Physics Division of the U.S. Department of Energy under Contract No. DE-AC03-76SF00098.

Figure Captions

1. RF Linac for heavy ion fusion driver. From Ref. 7
2. Synchrotron for heavy ion fusion driver. From Ref. 7
3. Induction linac for heavy ion fusion driver. From Ref. 7
4. Intra-beam charge exchange and ionization losses leading to beam attenuation in a storage ring.
5. Correlation diagram for $Cs^+ + Cs^+$ interaction from Olson and Liu.[16] Note crossing of $5p\sigma_u$ orbital with $6s\sigma_g$ orbital at appoximately 2.1 a_o.
6. Potential energy diagram of $Cs^+ + Cs^+$ system with interaction energy of the excited molecular state $1X\,{}^1\Sigma_g^{+**}$ $Cs^{+*} + Cs^{+*}$ system. Note curve crossing at 2.55 a_o.
7. Q Machine plasma-target apparatus.
8. Ionization probability for cesium on tungsten.
9. Critical density for cesium plasma on tungsten.
10. Idealized axial potential profile for negative sheath potential.
11. Theoretical radial plasma density profile using equation 4.17 with a square source function. The peak density is normalized to one.
12. Vapor pressure of cesium as a function of temperature. The density of cesium vapor at the wall temperature was about 10^7 cm^{-3}.
13. Coherent waves observed in Q machine plasma. $\delta n/n \sim 10$ percent.
14. 250 kV accelerator system and experimental area.
15. Plasma-target chamber. End view.

CHAPTER 1

INTRODUCTION

The desirability of deriving useful energy from fusion reactions has been known for many years. Considerable progress has been made in the last thirty years towards achieving the goals of a commercial power generating facility based on fusion technology. However since the goal has yet to be attained, even on a prototype basis, the technology of fusion reactors has branched into many prospective classes of reactor types. Some of these may ultimately lead to a practical power plant. The evolution of fusion technology has been diverse and will probably continue to be so until a clear-cut winner on the basis of reliability, efficiency, cost, etc. is found. This thesis concerns itself with the study of one parameter needed to evalute the merits of one of the more recent proposed power technologies.

All first generation fusion reactors will probably be based upon the following exothermic fusion reaction:

$$D + T = {}^{4}He + n \ (+17.6 \text{ MeV})$$

The various fusion reactor experiments throughout the world have had as an ultimate goal the containment of a dense, hot plasma consisting of deuterium and tritium ions which would undergo such reactions under the proper conditions. To date, there have evolved

two main branches of proposed fusion reactors. Within these two groups there are many proposed schemes that are under study.

The first class of fusion reactors are based upon magnetic confinement where the plasma is confined in a magnetic field for increased radial confinement.[1] These technologies are the most advanced and will require relatively low densities (10^{14} cm^{-3}), long confinement times (several seconds), and large plasma temperatures (few keV) to be feasible. Examples of the current (or planned) experiments include tokamaks (PLT, TFTR) and open ended mirror devices[2] (TMX, MFMF-B). There are many alternate concepts that are being studied but tokamaks and mirror machines have made the most progress of all.

The second class of proposed fusion reactors are based upon inertial confinement whereby a relatively dense (~ 10^{24} cm^{-3}), hot plasma is compressed for short times (~ 1 nanosecond) in order to achieve a significant number of fusion reactions before the plasma expands and cools to the point where fusion reactions cease. Most of these schemes involve compressing tiny microspheres (< 1 mm diameter) containing deuterium and tritium to many times normal density and temperatures, thereby "igniting" the central core and using the inertia of the plasma to hold the reactants together long enough to allow enough fusion reactions to take place. The inertial confinement scheme for fusion reactors has made considerable progress but is probably less advanced than magnetic confinement schemes towards the ultimate goal of providing the technology for a useful power plant.

Within the inertial confinement approach to fusion technology there also have evolved two main classes which are being studied. The first and most advanced is laser fusion[3] where intense laser beams are focused onto the microspheres. The high intensity light creates a plasma and interacts with this plasma to drive a shock wave into the center of the pellet, causing the temperature and density of the core to reach the levels needed for a fusion burning to take place. The burning plasma then expands and ignites the surrounding plasma. Considerable progress has been made in laser fusion technology, but the program has been plauged by low laser efficiencies, unavailability of intense lasers of the proper wavelengths and plasma instabilities due to interaction of high intensity light with the plasma. Examples of laser fusion experiments are ARGUS and SHIVA at LLNL.

The other inertial confinement schemes use particle beams in place of laser beams to compress and ignite pellets. Several experiments have been built using either proton beams or electron beams.[4] The progress of these approaches have been less successful, primarily due to problems of transport of very high current beams of sufficient quality and energy to compress pellets. An example of a particle beam device is PBFA at LASL.

Primarily due to the lowered expectations of getting useful energy by laser driven inertial fusion, there has been in recent years a more thorough investigation into the particle beam driven approach to inertial fusion. In 1976 and subsequent years there were summer studies on the use of heavy ions for inertial

fusion.[5,6,7,8] The goal of the first study was to propose several accelerator schemes that, with minimal extrapolation of current technology, would lead to an economically viable fusion reactor system.

One of the main advantages of using heavy ion beams for inertial fusion is the very favorable energy deposition profile of heavy ions as they stop on matter. The so-called Bragg curves show that most of the energy of a heavy ion stopping in a solid is deposited in a very small interval near the end if its range. Using heavy ions instead of lasers would thus hopefully eliminate one severe problem associated with laser fusion: That is, preheating of the pellet central core due to heating electrons by the laser.

The energy and power needed to compress the pellets is essentially the same for lasers and particle beams. There must be approximately three megajoules of energy with a peak power of 100 terawatts (10^{14} watts) delivered on target. Target design determines the desired range of the projectile and hence the desired energy is determined for a given Z of the projectile. Possible candidates for projectile ions include U^{+1} and Cs^{+1}. For typical pellet designs, the energy requirement for a Cs^{+} beam should translate into a 10 GeV beam with 15 kiloamps delivered in 20 nanoseconds. These are severe requirements indeed.

The first summer study in 1976 identified several types of accelerator systems that could conceivably deliver the power and energy required for a useful reactor. These were 1) synchrotron; 2) rf linac and 3) induction linacs. Both synchrotrons and rf

linacs would require accumulator and/or storage rings in order to build up the current to the desired levels. Induction linacs are single pass devices and would not require such storage rings. These three accelerators are shown schematically in Figs. 1-3.

The linear induction accelerator has been used in the past to accelerate electrons[9] (e.g., ERA). The usefulness of induction linacs has not yet been demonstrated for light ions or for heavy ions, but some work is being done to test the concept.[10]

Synchrotrons and r.f. linacs have a long history and their technology is fairly advanced. Due to the fact that they can only accelerate relatively small currents, the use of storage rings with multiturn injection would be required for any useful ICF driver based on these technologies. It will be shown that the storage times are fairly long (~seconds) and this poses a possible problem for the storage ring concept. It was identified in the first heavy ion fusion summer study that binary collisions between beam particles might lead to a significant number of intrabeam charge changing collisions which would either cause decreased beam intensities or severe degradation of the beam due to interaction with sputtered material by the lost beam striking the walls of the accelerator. This process is shown schematically in Fig. 4.

The maximum tolerable cross section for beam loss can be estimated by considering a beam in a storage ring and treating it as a reacting gas with a spread in energies which lead to intrabeam collisions. The reaction rate for the beam ions can be expressed as

FUNCTIONAL SKETCHES OF REFERENCE SYSTEMS
(Numbers in parentheses are numbers of parallel units)

BNL: 10 MJ, 200 TW, RF linac base

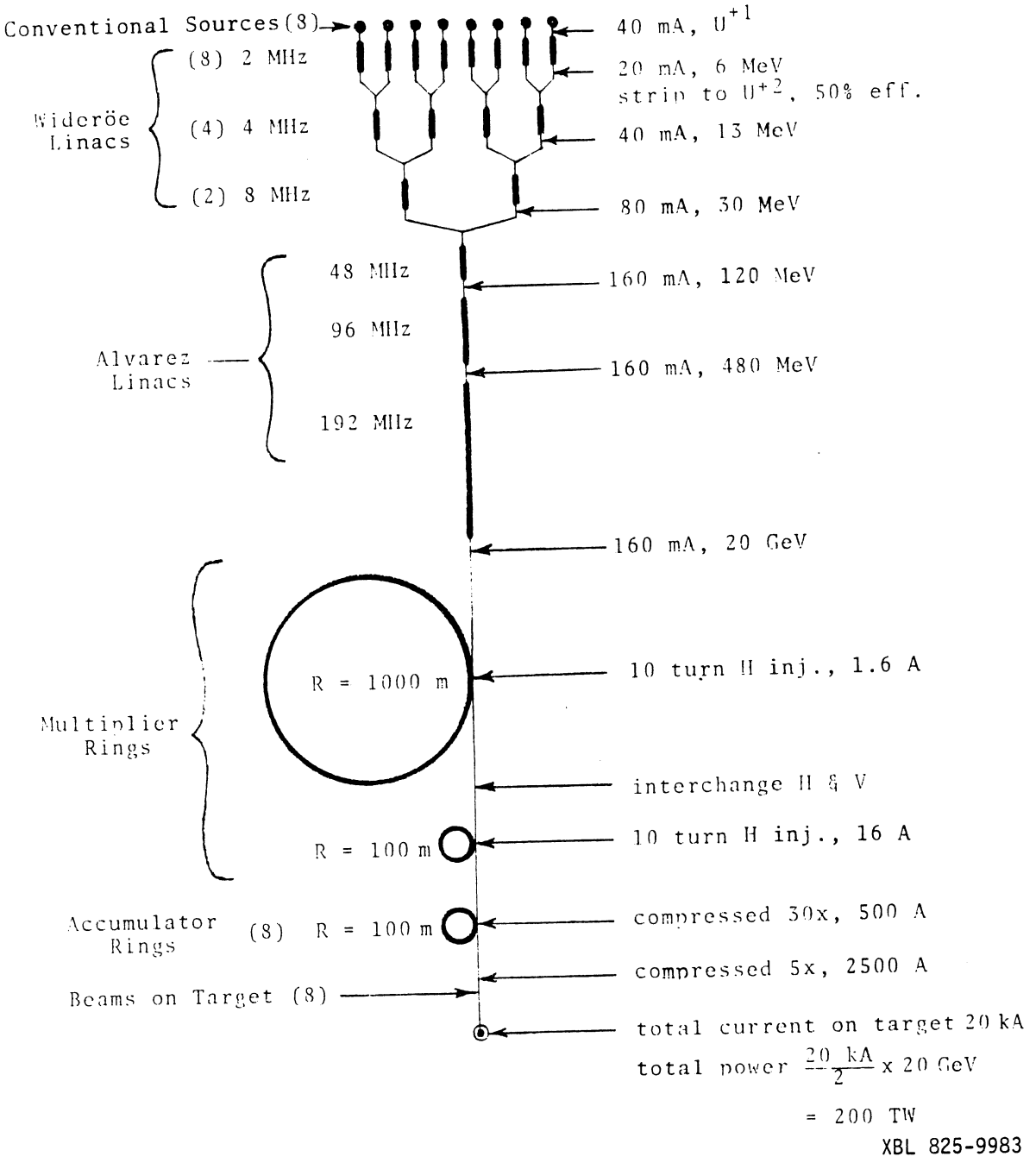

Figure 1. RF Linac for heavy ion fusion driver. From Ref.7

HF3-ANL: 1 MJ, 100 TW, synchrotron base

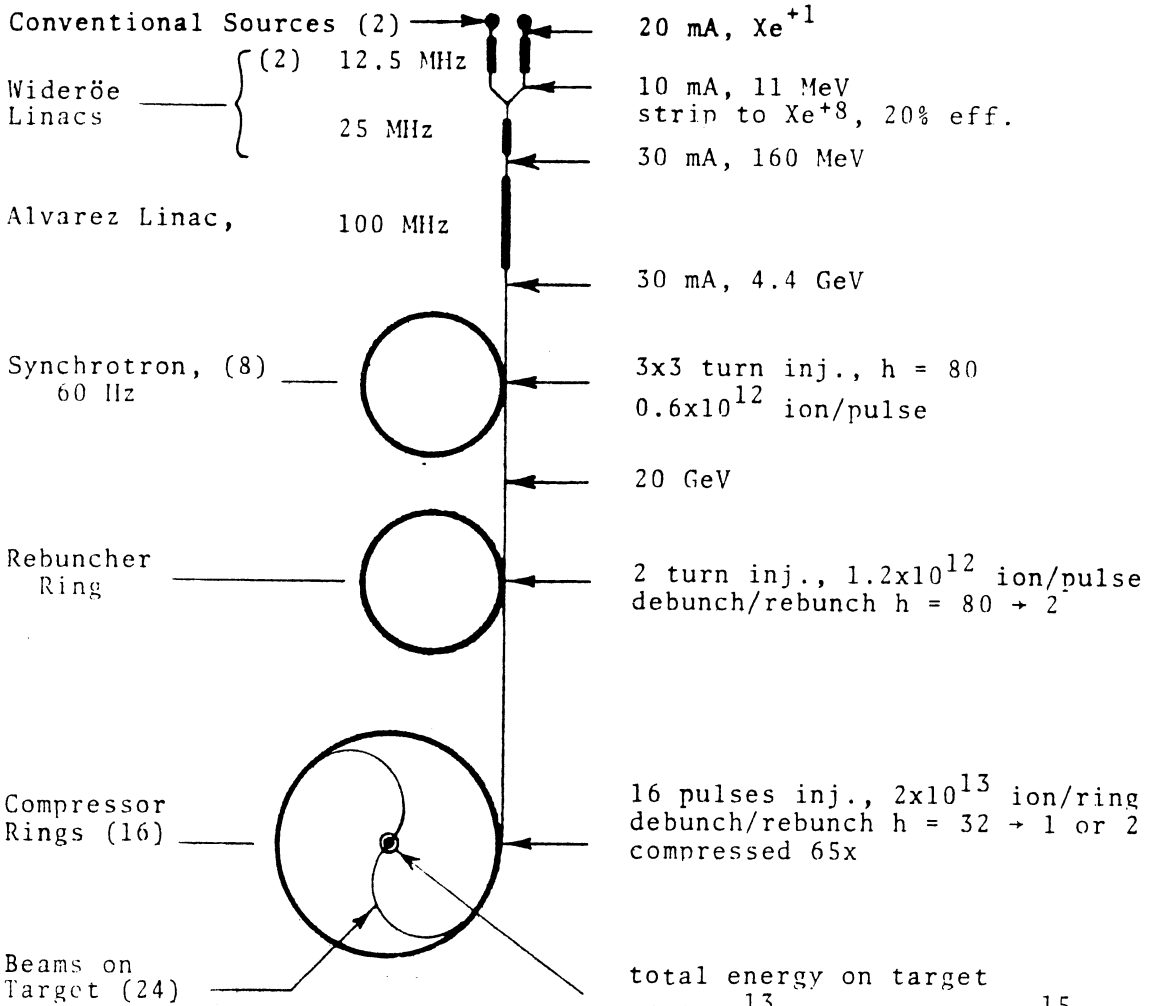

Figure 2. Synchrotron for heavy ion fusion driver. From Ref. 7

LBL: 1 MJ, 160 TW, induction linac base

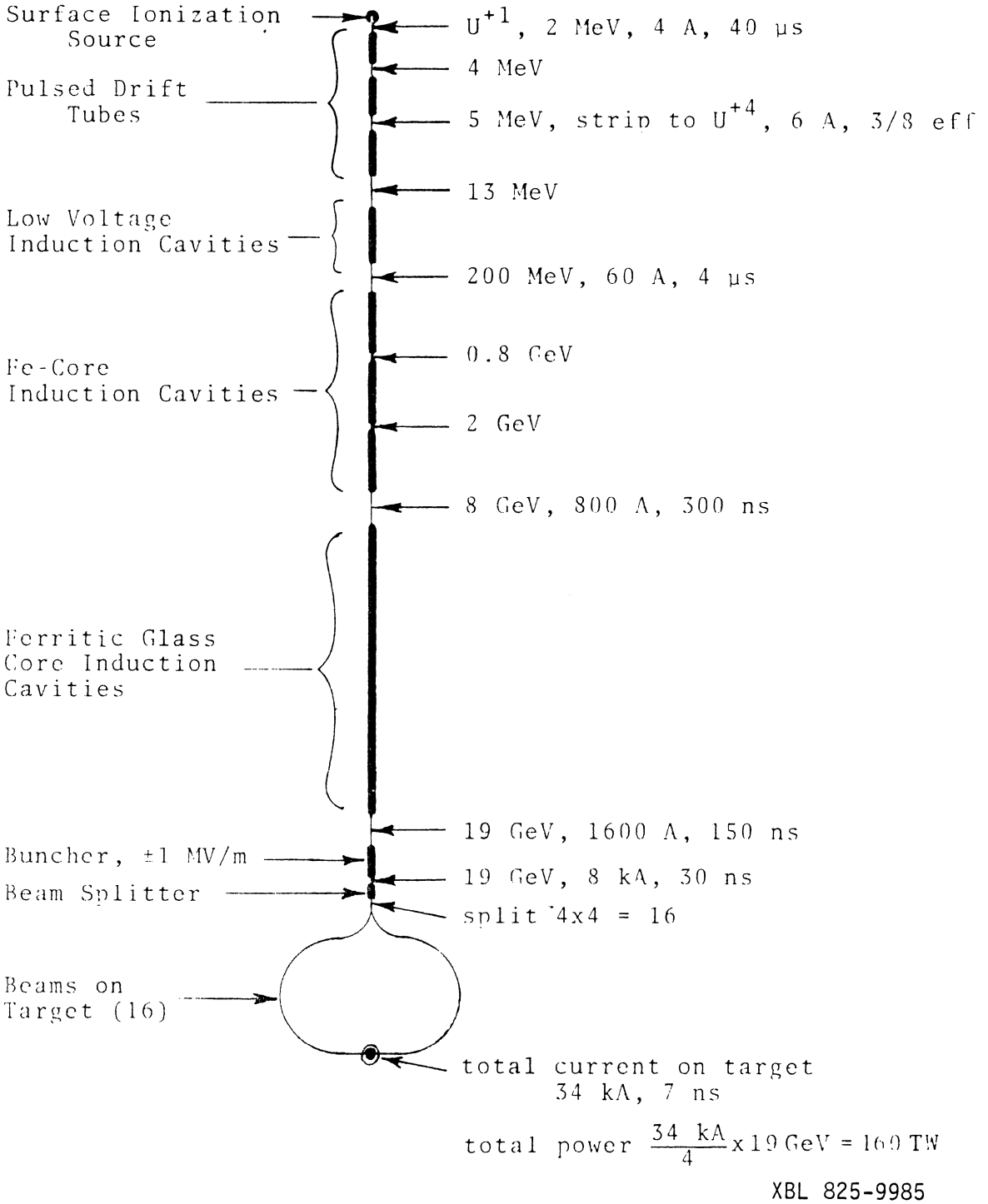

Figure 3. Induction linac for heavy ion fusion driver. From Ref. 7

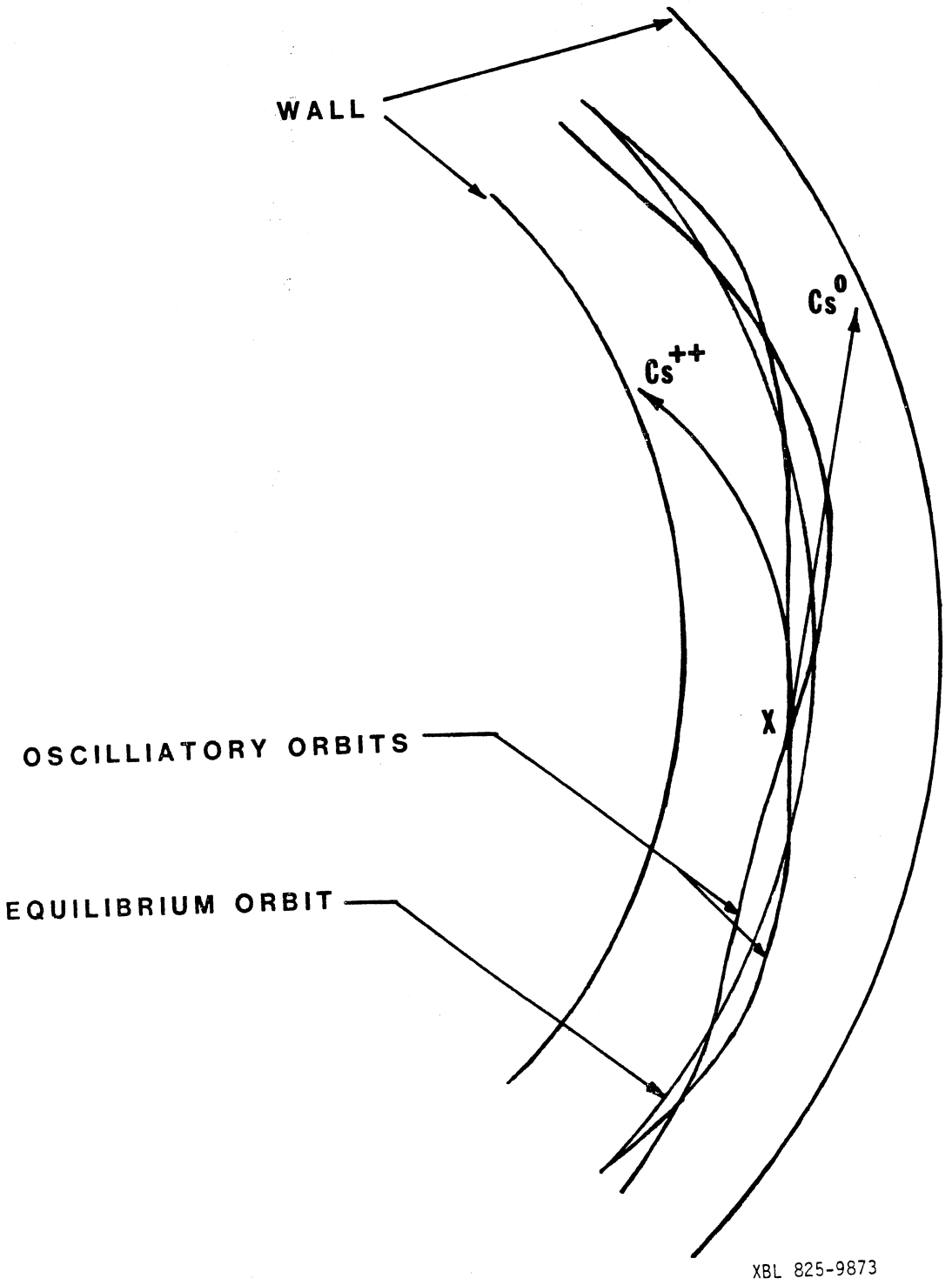

Figure 4. Intra-beam charge exchange and ionization losses leading to beam attenuation in a storage ring.

$$\frac{dn}{dt} = \frac{-n^2}{2} < \sigma(v_{rel})\, v_{rel} > \qquad (1.1)$$

where n(t) is the beam density and $\sigma\ (v_{rel})$ is the loss cross section for ions colliding with relative velocity v_{rel}. The bracket indicates the average is to be taken over the velocity distribution of the beam. The factor of 1/2 comes from the fact that identical particles are colliding.[11] This equation can be integrated to yield

$$n(t) = \frac{n_o}{1 + \frac{t}{\tau}} \qquad \text{where } \tau = \frac{1}{n_o <\sigma v>} \qquad (1.2)$$

Thus the beam would decay to 1/2 in a time τ. This formula would be valid for a coasting beam (i.e., a beam which fills the entire storage ring and is not being filled). In actuality the situation is more complex due to the fact that the beam is continuously being fed into the storage ring but this analysis yields insight into the essential physics of the problem. In order to determine the decay constant for the storage ring it is necessary to know the loss cross section and the velocity distribution of the particles within the beam. Given a storage ring of major radius R and a beam with transverse emmitance ϵ, where $\epsilon = \pi x_{max}\, x'_{max}$, it is possible to estimate the decay constant.

A 3 megajoule storage ring contains approximately 10^{15} ions at 20 GeV. If the betatron wavelength, β, is given, then the size of the beam is given by

$$x_{max} = \sqrt{\frac{\beta\epsilon}{\pi}} \qquad (1.3)$$

The density of the coasting beam then is given as

$$n = \frac{N}{2\pi R\beta\epsilon} \tag{1.4}$$

Typical values for β and ϵ are 20 meters and 3×10^{-5} m-rad, respectively. If R = 1000 m, then $n \sim 3 \times 10^{8}$ cm^{-3}.

The simplest distribution function for the particles in the beam is a δ-function velocity distribution function. Then, approximately

$$\langle \sigma(v_{rel})\, v_{rel} \rangle = \sigma(v_{rel}) \cdot v_{rel} \tag{1.5}$$

Thus the beam time constant (for typical conditions, it is expected that $\sigma(v_{rel}) = 10^{-16}$ cm^2 and $v_{rel} = 3 \times 10^{7}$ cm/sec) is 1.0 sec.

In practice the fill time must be much shorter than the time constant so that an appreciable amount of beam is not lost. Thus it is reasonable to require $t_{fill} < 0.01\ \tau$. This would imply a maximum fill time of 10 ms. This is a very short time to accumulate the required current. It is therefore necessary to know the loss cross section accurately in the range of energies where the intrabeam collisions are likely to take place. This is the prime motivation for performing the series of measurements reported in this thesis. If the loss cross section turned out to be too large ($\sim 10^{-15}$ cm^2), then all heavy ion fusion drivers based on storage ring technology would not be useful.

Theoretical estimates for the ion-ion cross sections first were discussed at the initial summer study and each subsequent study has included sessions on this problem. In 1976 Kim[5] summarized the

state of knowledge regarding these heavy ion systems and called for the need to study both theoretically and experimentally the physics of ion-ion collisions as well as the simpler ion-backround gas collision physics. He estimated that the charge transfer cross sections would dominate over ionization. That is, for any ion A, he predicted the cross section for the process

$$A^+ + A^+ \rightarrow A^{++} + A^0 \tag{1.6}$$

would dominate over ionization processes:

$$A^+ + A^+ \rightarrow A^{++} + A^+ + e \tag{1.7}$$

The state of knowledge regarding ion-ion collisions at that time was so uncertain that the actual species involved was not very important. However it was thought that ions with closed shell configurations would have the smallest cross sections. Kim estimated that the charge exchange cross section for ions such as Cs^+, I^+, U^+ and Au^+ would be 5 - 10 x 10^{-16} cm^2 in the energy range of 50-100 keV. The uncertainty in these estimates was large and prompted the investigations in this thesis. Subsequent to the initial estimates, Hiskes[12] also estimated that the charge exchange cross ection for cesium ions probably had an upper limit of 10^{-15} cm^2.

After the initial theoretcial investigations major refinements and revisions were proposed. Macek[7] proposed that the ionization cross section, Reaction (1.7), might not be negligible in comparison to charge transfer. In the process of Pauli excitation, as two heavy ions approach, the exclusion principle causes electronic orbitals of the individual ions to higher levels. Then, as the ions recede, inner shell vacancies will form and autoionization processes will result in reactions of the form Eq. (1.7). The estimated ion-ion collision cross section was re-evaluated by Cheng, et.al.[6], to be 0.62-7.8 x 10^{-16} cm^2 for Cs^+. The energy was assumed to be ~ 50 keV and no energy dependence was indicated.

No experimental work on these systems had been done at the time and it was decided to try to measure the cross sections. The measurements of these cross sections can be done by two methods which are described more fully in Chapter 3. Briefly, either a crossed ion-beam technique could be used or a plasma target technique could be developed. We chose to try to develop the plasma target technique as being simpler and faster than developing a crossed beam apparatus which was not available in our laboratory.

After the initiation of the plasma target experiment at LBL, two other groups measured the ion-ion collision cross sections by the crossed beam technique. Dunn, et.al.,[13] at Queen's University of Belfast, N. Ireland and Peart, et.al.[14,15] at the University of Newcastle upon Tyne, England, have published their results for the ion-ion cross sections relevant to Cs^+. Dunn, et.al.[13] found

that the sum of ionization and charge transfer was approximately 2 x 10^{-16} cm^2 over the range of energy from 40-280 keV with very slight structure around 80 keV. On the other hand, Peart, et.al.[14] found the cross section to vary approximately linearly from 2 x 10^{-17} cm^2 at 20 keV to 1.3 x 10^{-16} cm^2 at 80 keV. Since their results differed by as much as a factor of three, the plasma target technique was a good check on the merits of both methods as well as providing new data on the collision physics of this heavy ion system.

Since the publication of initial experimental results, the theoretical estimates have tended to converge to the experimental results. Peart and Dolder[15] experimentally have shown that charge transfer is negligible in comparison to ionization in $Cs^+ + Cs^+$ collisions. Recently, Olson, et. al.[16] has justified this theoretically. His estimate for the ionization cross section is 3 x 10^{-16} cm^2 at 50 keV, rising slowly with increasing energy.

The results from the present experiment tend to agree better with the results of Peart et.al. as opposed to those of Dunn, et.al. The results are summarized in Chapter 7, Table 2. The cross section is 0.47 ± .11 x 10^{-16} cm^2 at 50 keV and rises approximately linearly to 1.87 ± .18 x 10^{-16} cm^2 at 110 keV.

This thesis describes the plasma target technique developed to measure ion-ion cross sections. Chapter 2 discusses the theoretical estimates of the cross section. Chapter 3 describes the merits and procedures of the crossed beam technique and the plasma target technique. Chapters 4, 5 and 6 describe the plasma target method.

The results of this experiment are presented in Chapter 7. Appendices A–E discuss the experimental components and techniques as well as some of the calculations relevant to the plasma target method. Finally, Appendix F discusses the relevance of this technique to other ion–ion systems, such as D^- collisional detachment processes in plasmas.

CHAPTER 2

ATOMIC PHYSICS THEORY

Early theoretical estimates of the $Cs^+ + Cs^+$ cross sections were given at the summer studies for heavy ion fusion.[5,6,7,8] In fact, the idea for using Cs^+ in a heavy ion fusion driver was motivated by theoretical estimates that the charge transfer cross section, σ_{CX}, would be small for Cs^+ due to its closed shell configuration. These closed shell configurations were considered important to minimize the likelihood of electron transfer from one ion to the other. The theoretical discussion which follows is a condensation of the simple theories presented at the summer studies, plus the later work of Hiskes[12] and the more comprehensive work of Olson.[16]

First, consider a cesium atom in its ground state. The electron configuration is $Cs(6s)\ ^2S_{1/2}$. This atom lies in the first column of the periodic table. It is an alkali metal. It has a low ionization potential due to the weakly bound outer 6s electron. The ionization potential is approximately 3.87 eV. If this outer electron is removed, a Cs^+ ion is left with a closed shell configuration of Cs^+ $(6p^6)\ ^1S_0$. This is the same configuration of Xenon, a nobel gas. Thus, in removing the outer electron from cesium, we are left with an ion which has a noble gas electronic configuration. Since the noble gases are known to have small reaction rates among themselves at thermal velocities, it would be expected that Cs^+ would behave approximately the same.[5]

Before proceeding, it is necessary to consider the energy range of the collisions. The accelerator theorists have said that the collision energies of interest are between 50 to 100 keV. Thus, the relative interaction velocities are approximately 3×10^7 cm/sec. This is similar to the classical electron velocity in cesium which is given in a hydrogenic picture as

$$V = \frac{e^2}{nh} \sim 4 \times 10^7 \text{ cm/sec} \quad . \qquad (2.1)$$

Thus, collisions between Cs^+ ions require a molecular orbital analysis rather than an impact ionization analysis such as the Born approximation which would be expected to hold up at high velocities.[16] Collisions between Cs^+ ions at the energies of interest therefore will form molecules for short times, and the dissociation of the molecules determine the branching ratio to either Cs^{++} or Cs° or to inelastic excited products such as Cs^{+*}.

The interaction potential energy curve gives important insight into the physics of the collision in the molecular orbital approach. At very large distance, since both particles are singly charged, one would expect the potential energy of interaction would be Coulombic and vary as 1/R [R = internuclear separation]. As the two ions approach each other, the wave functions begin to overlap, and the interaction becomes more complicated.

The complexity of the problem can be appreciated by the fact that each Cs^+ ion has 54 electrons. Thus, when a collision forms a pseudo molecule, there are 108 electrons interacting along with

the nuclear repulsion of the nuclei. Many models have been developed over the years to handle these types of problems. The model which has been most successful in handling symmetric neutral rare-gas systems is the so-called Fano-Lichten promotion model.[17,18] Since Cs^+ has a rare-gas electronic configuration of Xe, it is appropriate to use this model to explain $Cs^+ + Cs^+$ interactions. The Fano-Lichten model has been used by Olsen and Liu[16] to calculate the cross section for Cs^{++} formation.

The Fano-Lichten model is constructed by calculating the molecular orbital energies of the Cs_2^{2+} pseudo-molecule as a function of internuclear separation. The wave functions were computed by Olsen and Liu by a self-consistent field (SCF) method and the results are shown in Fig. 5. One can see that the $5p\sigma_u$ orbital crosses the $6s\sigma_g$ orbital at approximately 2.1 a_o. Thus, during a collision, an excited molecule $Cs_2^{2+}(5p\sigma_g^2\ 6s\sigma_g^2)$ is formed. This molecular ion dissociates into two channels. The reaction can be summarized by the following equation:

$$Cs^+ + Cs^+ \rightarrow Cs_2^{2+}\ (5p\sigma_g^2\ 6s\sigma_g^2) \rightarrow \begin{cases} Cs^{+**}\ (6s^2) + Cs^+ & (2.2a) \\ Cs^{++}\ (6s) + Cs^{++}(6s) & (2.2b) \end{cases}$$

Now, Cs^{+**} $(6s^2)$ is doubly excited and can therefore decay to $Cs^{++} + e^-$ by an autoionization process. This is the dominant channel for production of $Cs^{++} + Cs^+ + e^-$. The lifetime of the state presumably is short such that the decay takes place before

the ions have separated too much. The theory does not consider post collision interactions which may alter the branching ratios to the various final states. Such effects have been seen in electron-ion threshold autoionization experiments.[19] On the basis of experiments on the related Ar + Ar system, Olson claims that approximately 50 percent of the inelastic products of reactions (2.2a) and (2.2b) can lead to charge-changed products (i.e., either $Cs^{++} + e^-$ or Cs^0.

A more detailed calculation of the $6s\sigma_g^2$ doubly excited state molecular configuration is shown in Fig. 6 along with the repulsive potential energy of the $Cs^+ + Cs^+$ system. A curve crossing occurs at $R_x = 2.55a_o$ with a threshold energy of 160 eV. It is claimed that the probability is large [approximately unity] for transition to the inelastic states for impact parameters less than R_x, i.e., the cross section for formation of Cs^{++} approximately is given by

$$\sigma_{12} = 0.5\ \pi\ R_x^2 = 2.8 \times 10^{-16}\ cm^2 \qquad (2.3)$$

Olsen and Liu claim that this cross section will rise slightly with energy due to the contribution of impact ionization to the collision process. The range of validity of the theory is from approximately 50-100 keV.

In conclusion, the Fano-Lichten model has been applied by Olsen and Liu to show that a $5p\sigma_u$ molecular state of Cs_2^{2+} is promoted to the $6s\sigma_g^2$ $\left(^1\Sigma_g^{+**}\right)$ state and this state then

decays to $Cs^{++} + Cs^{+} + e$ by an auto-ionization process. The theoretical value for the cross section was estimated to be approximately 3×10^{-16} cm^2. This theory is compared in Chapter 7 to the results of this experiment and to the results of Peart, et. al.[14], and Dunn, et.al.[13]

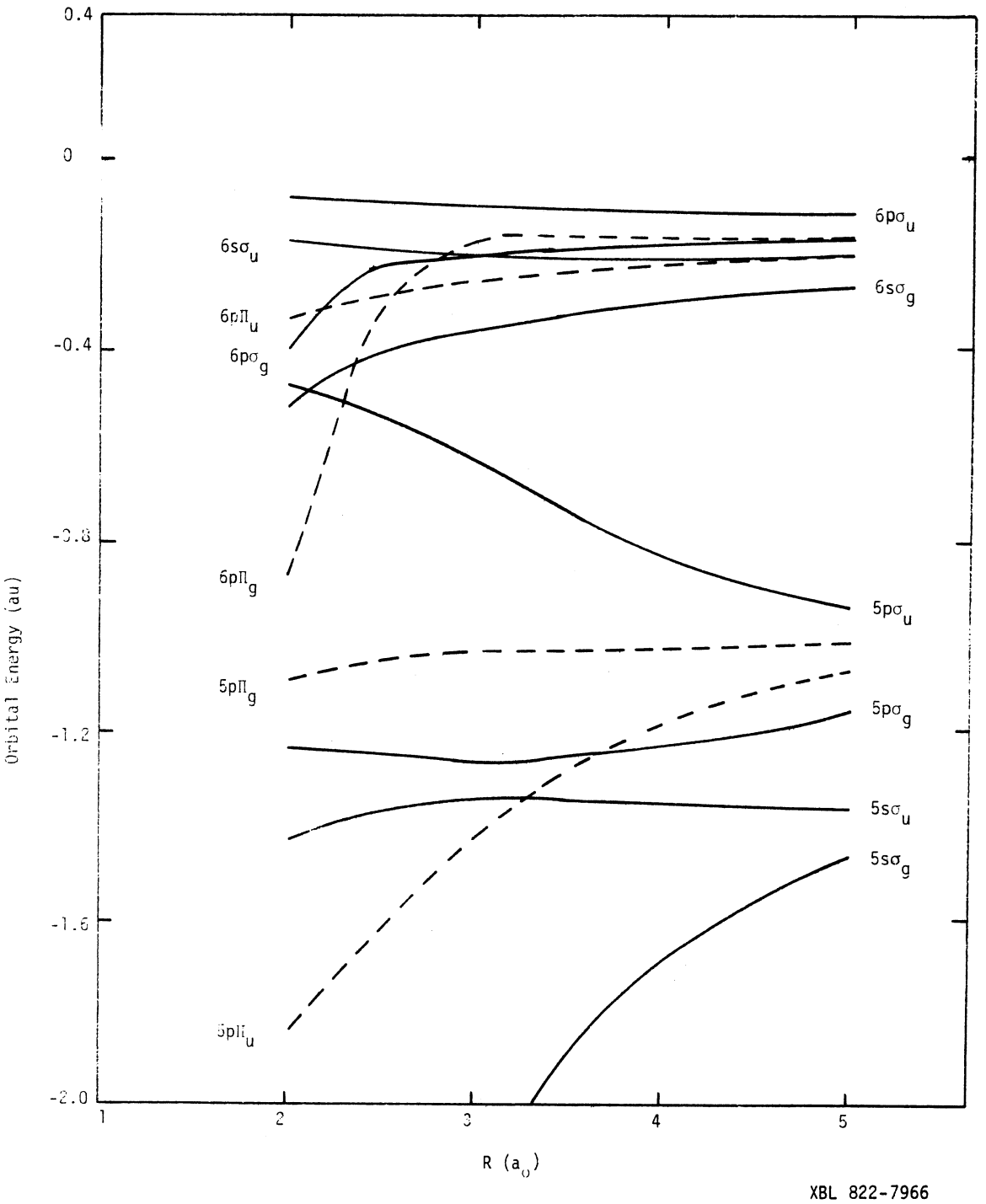

Figure 5. Correlation diagram for $Cs^+ + Cs^+$ interaction from Olson and Liu.[16] Note crossing of $5p\sigma_u$ orbital with $6s\sigma_g$ orbital at approximately 2.1 a_o.

Figure 6. Potential energy diagram of Cs^{+} + Cs^{+} system with interaction energy of the excited molecular state $1X\ \Sigma_g^{+**}$ Cs^{+*} + Cs^{+*} system. Note curve crossing at 2.55 a_o.

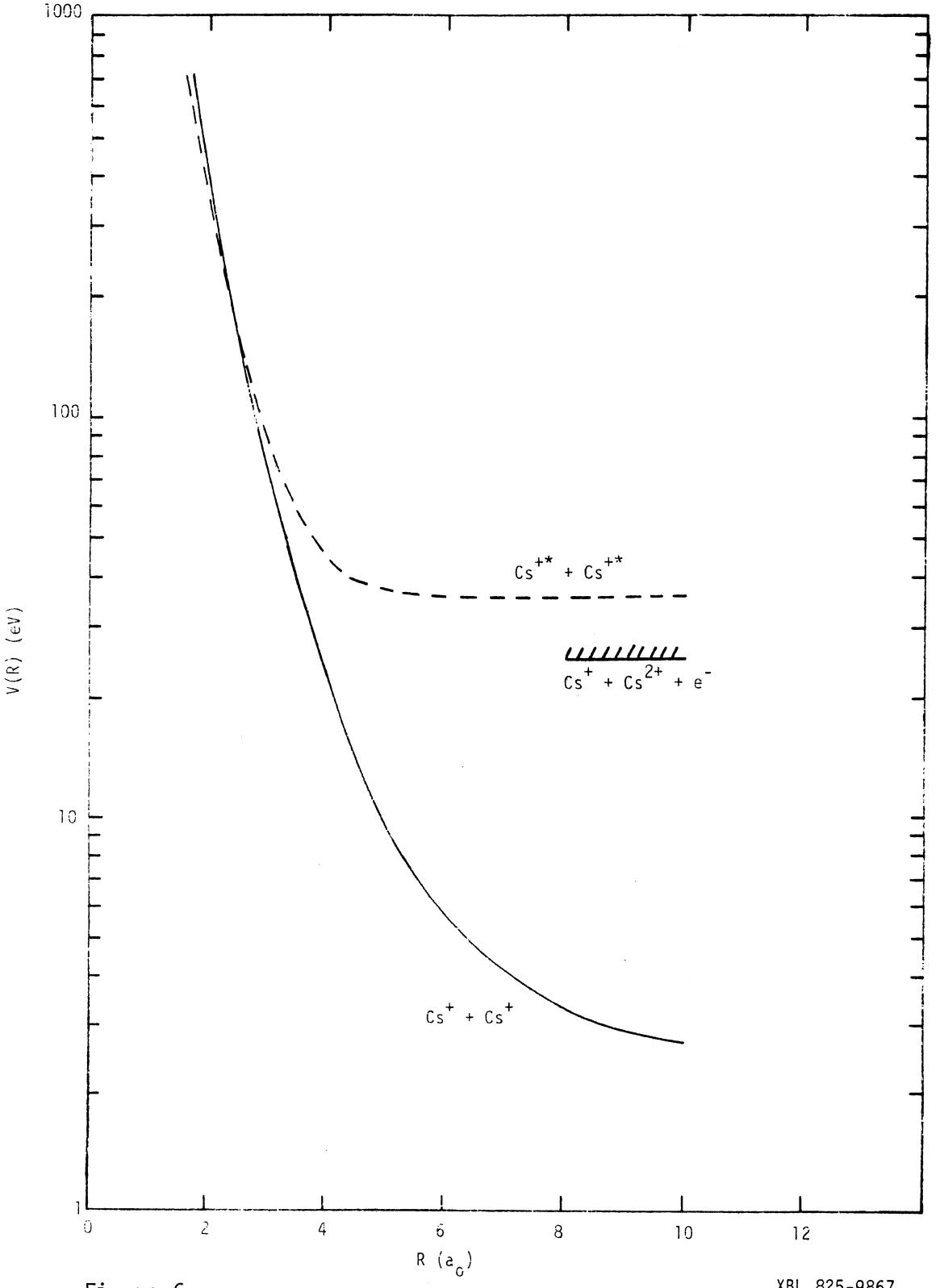

Figure 6

XBL 825-9867

CHAPTER 3

COMPARISON OF PLASMA TARGET TECHNIQUE TO CROSSED BEAM TECHNIQUES

The plasma target technique described in this thesis is new and it is useful for measuring certain ion-ion collision cross sections. There is one alternative method that has been developed using crossed-ion beams, and it is useful to consider the advantages and disadvantages of each method. In fact, the experimental results from this experiment will be compared to similar results derived by that technique.

The crossed ion beam technique has evolved since the 1960's as the most productive and accurate way of measuring ion-ion and electron-ion collision cross sections.[20,21] The method basically consists of using two accelerators to provide two beams that are intersected such as to create reactions between the constituents of the different beams. The intersections may be either perpendicular ($\theta = 90^\circ$), oblique ($\theta \sim 10^\circ$ or $\theta \sim 170^\circ$) or merged ($\theta \sim 0^\circ$)). The intersection angle is determined by the needs of a particular experiment. When two constant diameter beams of energy E_1, E_2 charge e_1, e_2, mass m_1, m_2 and currents I_1, I_2 intersect, a certain fraction will suffer collisions and give rise to product ions. The reaction rate R can be related to the cross section by the well known result

$$\sigma(E) = \frac{RF}{I_1 I_2} K \quad , \tag{3.1}$$

where F is a form factor describing the geometry and current densities of the intersecting beams,

$$F = \frac{\int I_1(x)dx \int I_2(x)dx}{\int I_1(x) I_2(x)dx} \tag{3.2}$$

where $I_1(x)$ and $I_2(x)$ are the currents flowing in elements of the beam of height dx, and K is a rate constant describing the relative velocities of the two beams:

$$K = \frac{e_1 e_2 v_1 v_2 \sin\theta}{(v_1^2 + v_2^2 - 2 v_1 v_2 \cos\theta)^{1/2}} \tag{3.3}$$

K is determined accurately if the beam energy and intersection angle are measured accurately. The form factor F usually is more difficult to determine and usually is done by moving a small slit (slit width << size of beams) past each beam and accurately measuring the current density of each beam. Then, approximately

$$F \sim \frac{\Sigma I_1(x)\ \Delta x \quad \Sigma I_2(x)\ \Delta x}{\Sigma I_1(x)\ I_2(x)\ \Delta x} = \frac{\Sigma I_1(x) \quad \Sigma I_2(x)}{\Sigma I_1(x)\ I_2(x)} \quad \Delta x \tag{3.4}$$

is computed. Δx is not the slit width, but the distance between successive positions of the slit.

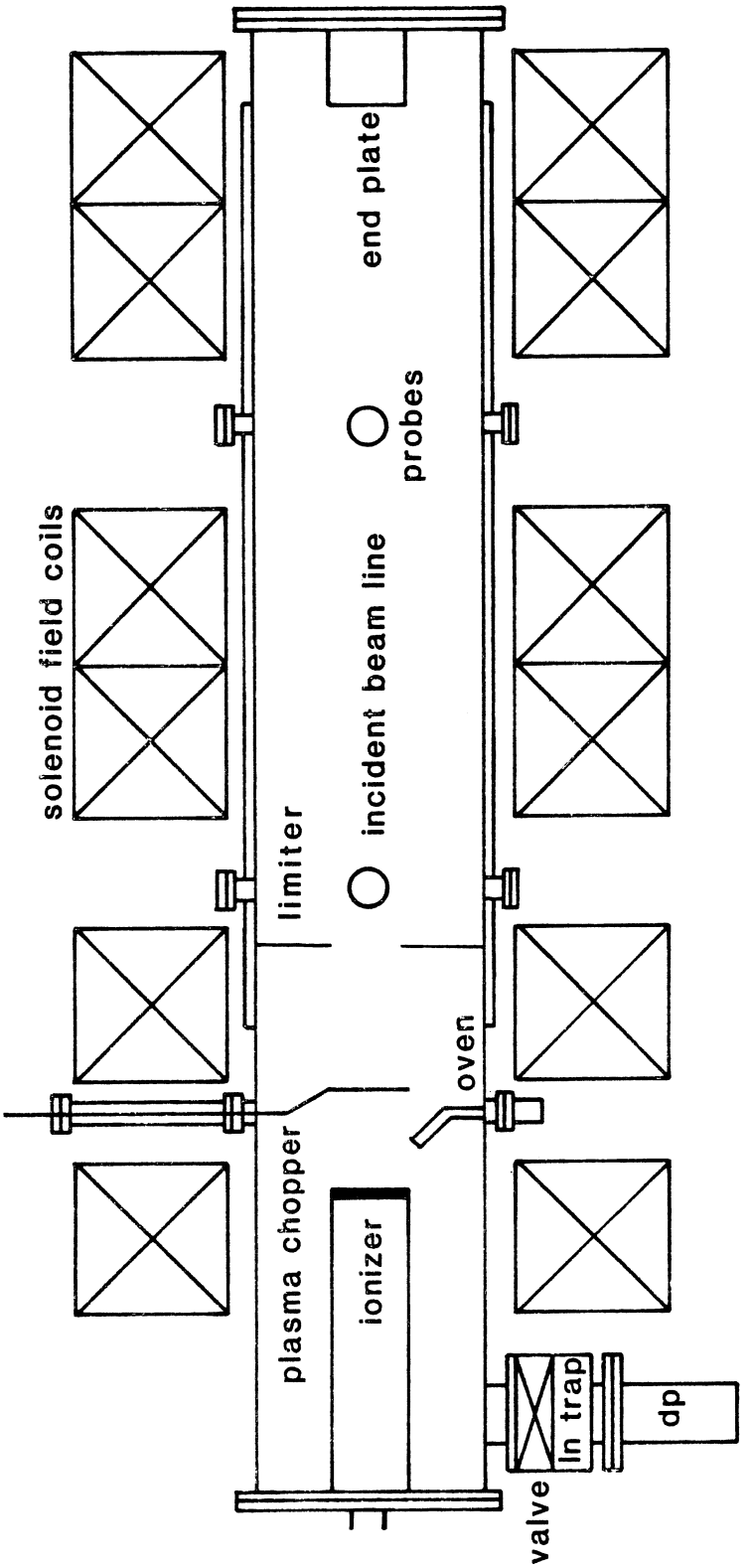

BASIC Q MACHINE GEOMETRY

XBL 825-9987

Figure 7

The quantity $\sigma(E)$ then can be computed from a determination of the reaction rate R which is simply the rate at which a detector measures the product ions. Here E is the center of mass energy given by

$$E = \frac{m_1 m_2}{m_1+m_2}\left[\frac{E_1}{m_1} + \frac{E_2}{m_2} - 2\left(\frac{E_1E_2}{m_1m_2}\right)^{1/2} \cos\theta\right] \qquad (3.5)$$

The crossed beam technique conceptually is simple, but in practice difficult due to many experimental problems. A few are listed here:

- o Low current beams (~ 10^{-6} A/cm^2) yielding beam densities of approximately 10^6 cm^{-3}. Thus, the reaction rates are small. Some experiments require counting for 200 hours to obtain sufficient counting statistics.
- o Small signals mean that the signal/background ratio is small and hence the need for ultra high vacuum [~ 10^{-10} torr] to reduce backgrounds. Beam chopping is usually used to separate signals from background. Typical signal/background ratios range from 0.1 to 10^{-3} for crossed-beam experiments.
- o Space charge effects: Slow moving beams spread more than the amount due to collimation because of a space charge repulsion of the beam. This can affect the geometry of the collision region and hence the form factor F.
- o Backround modulation: This is the most subtle and difficult problem associated with the crossed beam technique. An example can show what causes this problem: Suppose we look at the reaction

$$He^+ + H_2^+ \rightarrow He^+ + H^+ + H^+ + e \qquad (3.6)$$

The background gas can also give rise to H^+, e.g.

$$H_2^+ + H_2 \rightarrow H^+ + H^+ + e + H_2 \qquad (3.7)$$

By modulating the He^+ beam, the background H_2 may also be modulated and this can cause protons from reaction (3.7) to be modulated. The modulation of this background has nothing to do with the primary reaction (3.6) and can cause problems if the signal to background ratio is small (say 10^{-3}) and the background is modulated by say 1 percent. One has to be careful to vary the beam current to make sure the background is not being modulated enough to cause problems.

These are the main problems associated with the crossed beam technique. It should be noted that although these problems are severe, useful results have been deduced from the method and it is probably the most versatile inasmuch as a large variety of systems can be studied with relatively little change in the basic apparatus. A summary of the most recent ion-ion collisions studies has been completed by Gilbody.[22]

The plasma target technique developed as part of this thesis complements the crossed beam technique in that the same cross section can be measured by both methods.

A description of the plasma target technique should begin by noting that the technique, while useful for this case, is not

universally applicable. We have developed the technique for Cs^+ targets only. Although Q machines have run on all alkali metals and some of the alkaline earths (e.g. barium) we have not used these as targets. Thus, the plasma technique using a Q machine is limited to exploring a small class of ion-ion collisions.

With this limitation in mind, we will describe the method in detail. A plasma target technique is conceptually similar to a crossed-beam technique except that one of the beams is replaced by an essentially at rest collection of charged particles (electrons and ions) called a plasma. The Q machine was decided upon because of 1) The need for a Cs^+ target to study $Cs^+ + Cs^+$ interactions, 2) The Q machine could in principle be used with axial injection to get thick targets for other studies (D^- detachment), 3) the plasmas usually have a high degree of ionization which would lead to a large signal/background ratio.

After much studying of the conceived geometry, the final apparatus is shown in Fig. 7. It was determined that perpendicular injection (beam $\perp$ magnetic field) was preferable on several grounds.

- Although the target thickness, $\int n(r)dr$ is smaller for perpendicular injection the beam injection was much cleaner because it was not necessary to inject the beam through the hot cathode or obliquely which would give rise to a "spiral" of beams which would be difficult to separate and detect.
- The axial plasma confinement magnetic field could simultaneously separate the charge-changed-components of the beam.

- o The smaller target thickness allowed for greater angular acceptance of the detection system since the detector array could be placed closer to the target.
- o Radial line densities were easily determined by moving a probe radially across the plasma and sampling at a fast rate.

The technique involves creating a highly ionized plasma which is used as a target for a Cs^+ ion beam. The plasma consists of cesium ions (Cs^+) and electrons (e^-). Thus, one might think that electrons might "contaminate" the target by causing other reactions to take place. This indeed could happen in some energy ranges or other types of experiments (excitation studies, for example) but the presence of electrons are not a factor here. Let us consider all of the plausible reactions which might lead to a charge-changed cesium ion beam particle.

$$Cs^+ + Cs^+ \rightarrow Cs^{++} + Cs^\circ \qquad \text{charge transfer} \qquad (3.8a)$$

$$Cs^+ + Cs^+ \rightarrow Cs^{++} + e^- + Cs^+ \qquad \text{ionization} \qquad (3.8b)$$

$$Cs^+ + e^- \rightarrow Cs^{++} + 2e^- \qquad \text{electron ionization} \qquad (3.8c)$$

These three reactions are the only ones possible under single collision condition ($n\sigma l \ll 1$). Reaction (3.8c) is eliminated for the following reason:

Reaction (3.8c) is energetically impossible because at the highest beam energies (E_{Cs} = 240 keV Cs^+), the equivalent electron energy is $E_e = \frac{m_e}{m_{Cs}} E_{Cs+}$ or, E_e = 1.06 eV. Since the ionization potential of Cs^+ is 25.1 eV[23] this reaction is below threshold and the cross section for electron ionization is zero.

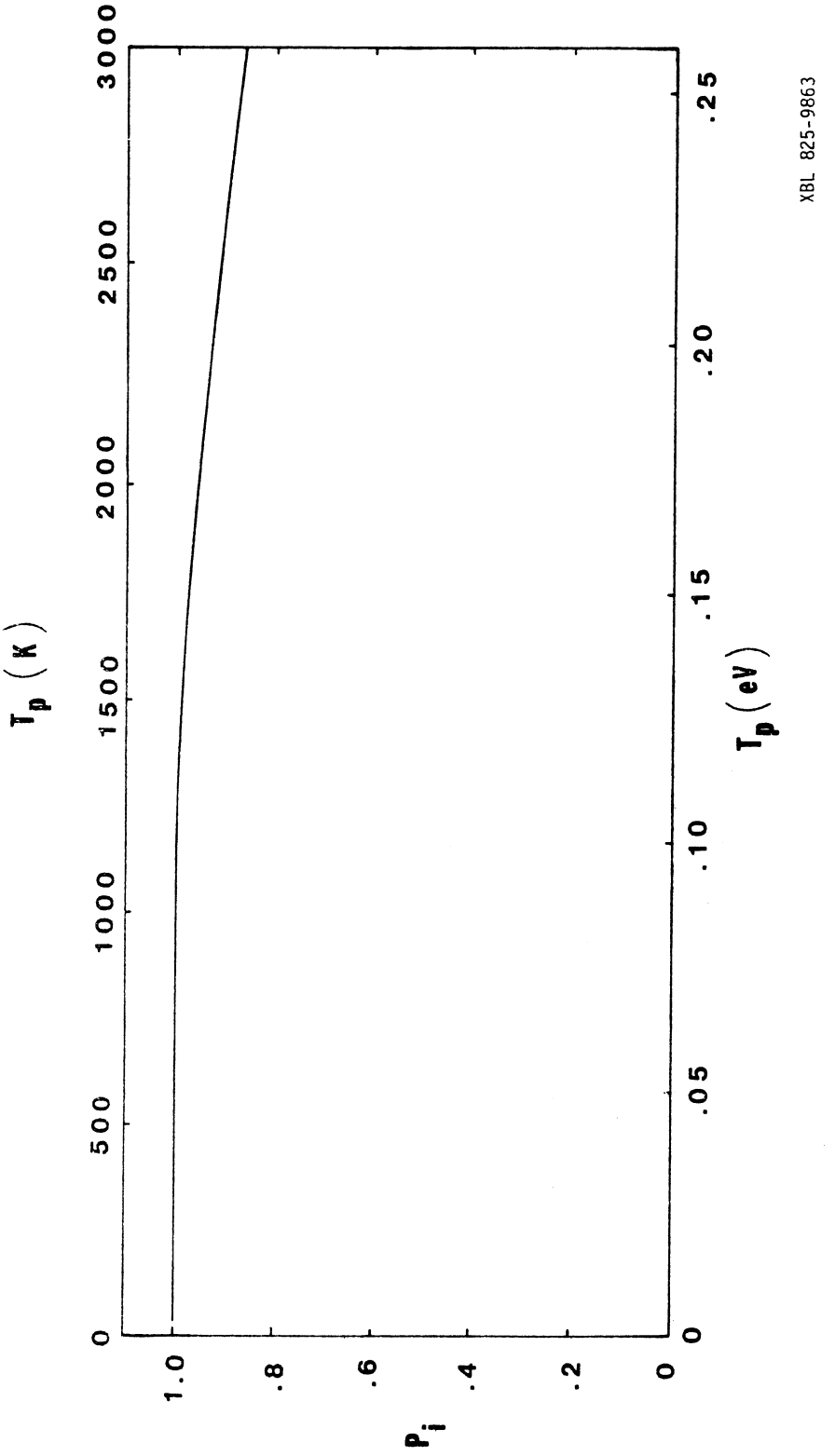

Figure 8. Ionization probability for cesium on tungsten.

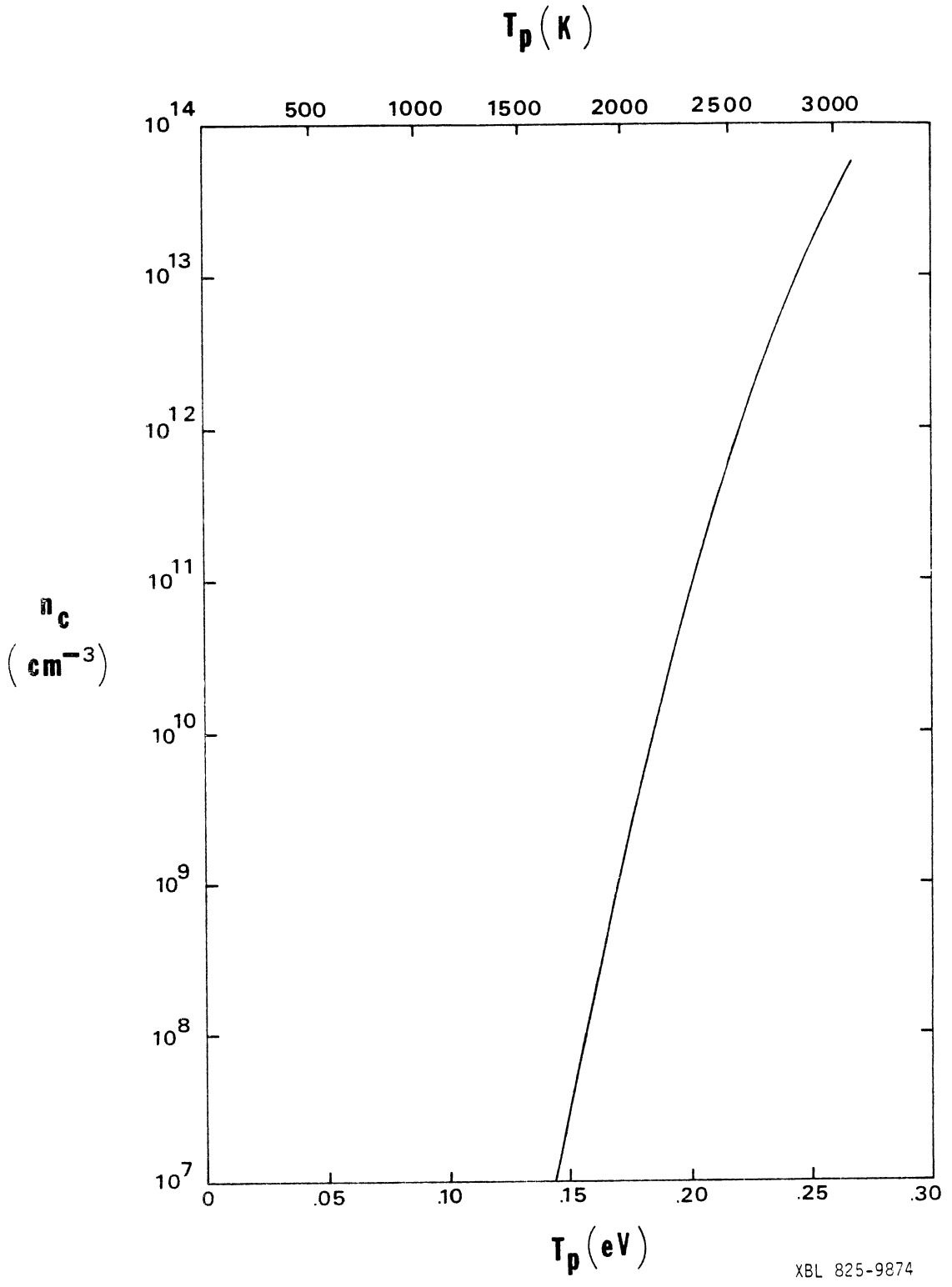

Figure 9. Critical density for cesium plasma on tungsten.

Thus, the only significant reactions that can take place are reactions (3.8a) and (3.8b). These are precisely the reactions measured in the crossed-beam experiments and it is these cross sections which are measured in this thesis. Both methods have the capability of measuring either the sum of reactions (3.8a) and (3.8b) by detecting the Cs^{++} component of the beam or reaction (3.8a) alone which is measured by detecting at the Cs° component of the beam.

The plasma target technique was the ideal method for measuring σ_{12}. The cross section theoretically was estimated to be approximately 10^{-16} cm^2 and then, for a plasma of 10^{11} cm^{-3} and 5 cm diameter, $n\sigma l = 5 \times 10^{-5}$. Although this fraction is small, it was measurable by using single particle counting techniques, and by chopping the plasma to separate the signal from the background effects of gas in the reaction chamber.

Another advantage of this plasma target was the fact that the signal to background ratio was substantially larger than in the case of the crossed-beam experiments. It was determined (Chapter 6) that the signal/background ratio was ~ 2, an improvement of at least a factor of twenty over usual crossed-beam experiments.

The primary disadvantage of measuring cross sections by the plasma target technique is the measurement of plasma density. A cross section is no better known than the density of the target which is used to measure it. Thus, for the crossed beam technique, the beam densities can be fairly well measured due to the fact that beam currents can be measured accurately. The main problem with the

beam plasma method is the systematic error of determining the absolute plasma density. The plasma density in this experiment was measured by Langmuir probe, and considerable work was done to compare the experimental probe results to theoretical probe analysis and also to other experimental results.

It has been shown that both the plasma target method and the crossed-beam technique are useful tools for measuring ion-ion collision. Although each has its advantages and disadvantages, comparing experimental results from each is useful to confirm the usefulness of either method.

CHAPTER 4

Q MACHINE PLASMA PHYSICS

The Q machine plasma target was chosen for several reasons. First, a target of Cs^+ ions was desired and Q machine plasmas are ideal sources of such ions. Second, the target was well defined by the size of the cathode and configuration of the magnetic field. Third, the plasma densities are very much larger than the densities of most ion beams from accelerators. This made detection of the secondary products easier. With these in mind, a description of the basic plasma physics follows.

Q machine plasma devices create a specific type of plasma known as a thermally ionized magneto-plasma. Many laboratory plasmas rely on driving an ionizing electron current through a gas which creates free electrons and ions. Other plasmas can be created by r.f. discharges, or laser irradiation. The Q machine was developed in the 1960's because of a need to study basic plasma physics which was free of turbulence produced by current driven plasmas.

In fact the letter Q stands for "quiescent" and it was hoped that the plasma would provide a very quiet medium in which to study basic plasma physics such as wave propagation. In fact the term Q machine is not very appropriate because the thermally ionized alkali metal plasmas are subject to other instabilities which sometimes gives rise to very turbulent behavior.

The basic Q machine consists of a hot (T ~ 2800 K), refractory metal plate (such as tungsten, rhenium, tantalum, molybdenum) which is inside a strong magnetic field (usally solenoidal). A low ionization potential atom spray (such as Cs, Rb, Na, Li, Ba) is directed onto the hot plate and as described by the Langmuir-Saha equation,[24] electrons and ions leave the hot plate and are confined by the magnetic field. Thus a plasma column is formed at the hot plate and it drifts along the magnetic field until it reaches the end of the device. The end of the device can have a cold plate where the plasma recombines, or it can have another hot plate which serves to reionize atoms on the far end. This later configuration is called double-ended whereas the cold plate configuration is referred to as single ended. Usually doubled-ended plasmas are more dense than single-ended plasmas.

The final configuration used in this experiment was single ended. It was simpler to deal with experimentally and the densities achieved were sufficient to measure cross sections after a single particle detection system was implemented. Several theories have been presented in the last twenty years to explain Q machine operation. A good reference for Q machine technology has been written by Motley.[25]

Several theories reqarding Q machine operation have been published in the last twenty years. These theories usually yield the radial plasma density profile and parameters such as the peak density as a function of hot plate temperature and cesium atom flux incident on the hot plates. The magnetic field strength is

important for the radial transport and it usually is assumed to be uniform spatially. The following discussion is based on the work of Rynn, et. al.[26,27] and Hashmi, et. al.[28] The important questions to ask regarding a plasma target are the peak density, radial profile, and the degree of ionization and stability of the plasma.

I. Plasma Production

Alkali metal plasmas are formed by thermal ionization of the low ionization potential alkali metal atoms on a hot, high work function surface. The atoms strike the hot surface and are ionized according to the Langmuir theory of ionization.[24] Given a condition of thermal equilibrium, atoms striking a hot plate of work function W and temperature T_p, have a probability of ionization given as

$$P_i = \frac{n_i}{n_o+n_i} = \left\{ 1 + \frac{g_o}{g_i} e^{e(I-W)/kT_p} \right\}^{-1}$$

where I is the ionization potential of the atom striking the hot plate. $\frac{g_o}{g_i}$ is the ratio of statistical weights and is equal to 2 for alkali metals. A plot of P_i is shown in Fig. 8.

Since a plasma is quasineutral, a flux of electrons must also be injected into the plasma to keep it neutralized. The source of electrons in a Q machine is the same hot plate that ionizes the alkali metal atoms. A significant ionization probability can occur at temperatures well below the operating temperatures of most Q machine hot plates. The hot plate temperature is raised to

approximately T = 3000 K to provide the required electron flux to maintain quasineutrality. The electron emission from hot surfaces also is well known and is described by the Richardson equation

$$J_e = A_R T_p^2 e^{-eW/kT_p} e^{eV/kT_p} \qquad (4.2)$$

where A_R is the Richardson constant. V is the plasma potential.

A crude estimate of the maximum plasma density can be derived by equating the flux of electrons leaving the hot plate to the flux of electrons from the plasma striking the hot plate. This yields the so-called critical density. The critical density is the maximum density of plasma that can be supported by the electron flux from the hot plate. This condition occurs when V = 0; for positive plasma potentials, ions are reflected at the sheath, lowering the density. When V < 0, electron flow to the plasma is inhibited.

The critical density is a function of temperature and is given as

$$n_c = \left(\frac{4 A_R}{e v_e} \right) T_p^2 e^{-eW/kT_p} \qquad (4.3)$$

A plot of n_c is shown in Fig. 9.

Most high density alkali metal plasmas are run with slightly negative plasma sheaths to keep the ion flux to the plasma the highest. A detailed analysis of this process has been described by Hashmi et.al.[28] That discussion concerned itself with double ended and single ended plasma operation. The configuration chosen

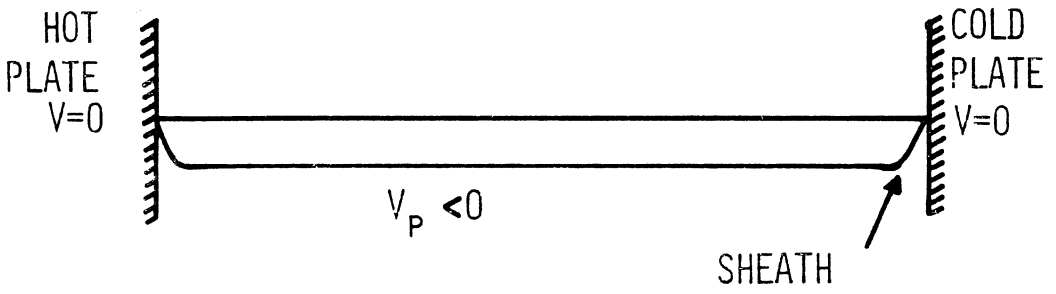

PLASMA POTENTIAL IN ELECTRON-RICH PLASMA

XBL 823-8722

Figure 10. Idealized axial potential profile for negative sheath potential.

for the present experiment was single ended. Since both the hot plate and the cold end plate were grounded, a negative plasma potential acted as an axial ion confining electrostatic well. This situation is shown in Fig. 10.

II. Radial Plasma Profile

In order to measure a cross section with a plasma target it is necessary to have an accurate knowledge of the integrated radial plasma density defined as

$$\pi = \int n_i \, dx \tag{4.4}$$

In general, this requires a knowledge of the absolute plasma density and also the radial distribution in order to compute the line density. For the experiments in this thesis, Langmuir probes were used to measure both density and the radial distribution. The procedures and analysis of this data are described in Chapter 6 and Appendix A. It is useful to have a theoretical understanding of the physics which gives rise to the radial variation of the plasma density. Rynn, et. al.[26] have constructed a useful theory for the radial profile based upon a radial diffusion term coupled with radiative recombination of the ions. The parameters which control the density variation also include the source term which describes the ionization of the atoms on the hot plate. Since the atom spray nozzle for ths experiment was not sufficiently small to create a collimated atomic beam, a wide angle spray was created which presumably covered the hot plate with a uniform flux of atoms.

Therefore it was decided that a square source function was the appropriate ionization parameter. As is shown, the radial distribution of plasma density qualitatively agrees with the actual distributions measured. In any event, the actual plasma line densities used in the experiments were numerically integrated from the experimental measurements of the plasma density at discrete intervals across the plasma column.

The density profile is theoretically derived as follows. The continuity equation is

$$\frac{\partial n}{\partial t} + \nabla \cdot (n\underline{u}) = S^{+} - S^{-} \tag{4.5}$$

where for this problem the sink term is described by a radiative recombination term:

$$S^{-} = \alpha n^{2} \tag{4.6}$$

The MHD momentum balance equation is

$$nm_i \frac{D\underline{u}}{Dt} = \frac{\underline{j} \times \underline{B}}{c} - \nabla P \tag{4.7}$$

or, with $\nabla \times B = \frac{4\pi}{c} \underline{j}$ this gives

$$nm_i \frac{\partial m}{\partial t} + nm_i (\underline{u} \cdot \underline{\nabla})\underline{u} = - (P + \frac{B^2}{8\pi}) + \frac{(\underline{B} \cdot \nabla)\underline{B}}{4\pi} \tag{4.8}$$

Assuming steady state operation and uniformity of $\underline{u}$ and $\underline{B}$ along field lines this simplifies to the well known result

$$P + \frac{B^2}{8\pi} = \text{constant} \tag{4.9}$$

Thermally ionized alkali metal plasmas are usually characterized by $T_e = 0.25$ eV, $B_o = 2000$ Gauss, and $n_e = 10^{11}$ cm^{-3}. Thus the plasma β defined as $\beta = \frac{8\pi nkT}{B^2}$ is very small ($\sim 10^{-6}$). This implies that $B = B_o$.

Since the problem we are considering has cylindrical symmetry, Eq. (4.5) becomes

$$\frac{1}{r}\frac{\partial}{\partial r}(rnu_r) + \frac{\partial}{\partial z}(nu_z) = S^+ - S^- \tag{4.10}$$

Using Ohm's law

$$\underline{E} + \frac{\underline{u} \times \underline{B}}{c} = \eta \underline{j} + \frac{\nabla p_i}{en} \tag{4.11}$$

and assuming $\underline{E} = 0$ in the plasma, we can plug this into the continuity equation to get

$$-\frac{1}{r}\frac{\partial}{\partial r}\frac{rn\eta j_\theta c}{B} + \alpha n^2 = S^+ \tag{4.12a}$$

and

$$j_\theta = 2enu_\theta \tag{4.12b}$$

That is, the plasma rotation gives rise to a diamagnetic current.

Simplifying these gives,

$$\frac{\partial^2}{\partial r^2} n^2 + \frac{1}{r}\frac{\partial}{\partial r} n^2 - \frac{\alpha n^2}{A} = -\frac{S^+}{A} \tag{4.13}$$

where

$$A = \frac{nc^2kT}{B^2} \tag{4.14}$$

Here, η is the Spitzer resistivity[29]

$$\eta \sim 6 \times 10^{-15}\, T^{-3/2}(eV)\, \ln \Lambda \quad \text{sec} \tag{4.15}$$

and $\ln \Lambda \sim 10$.

This equation for n(r) can be integrated once an appropriate source function S^+ is chosen. As explained earlier, this becomes

$$S^+ = \phi_o \qquad r<a \tag{4.16a}$$

$$S^+ = 0 \qquad r>a \tag{4.16b}$$

Equation (4.13) can be integrated to give

$$n^2(r) = C_1 K_o (kr) \qquad r>a \tag{4.17a}$$

$$n^2(r) = C_2 J_o (kr) + \phi_o \qquad r<a \tag{4.17b}$$

where $k^2 = \frac{\alpha}{A}$, and K_o and J_o are zero order Bessel functions.

Matching n and dn/dr at r = a yields the coefficients C_1 and C_2. The final result can be plotted as in Fig. 11. This plot is only the relative plasma density as the peak density is determined by

Figure 11. Theoretical radial plasma density profile using equation 4.17 with a square source function. The peak density is normalized to one.

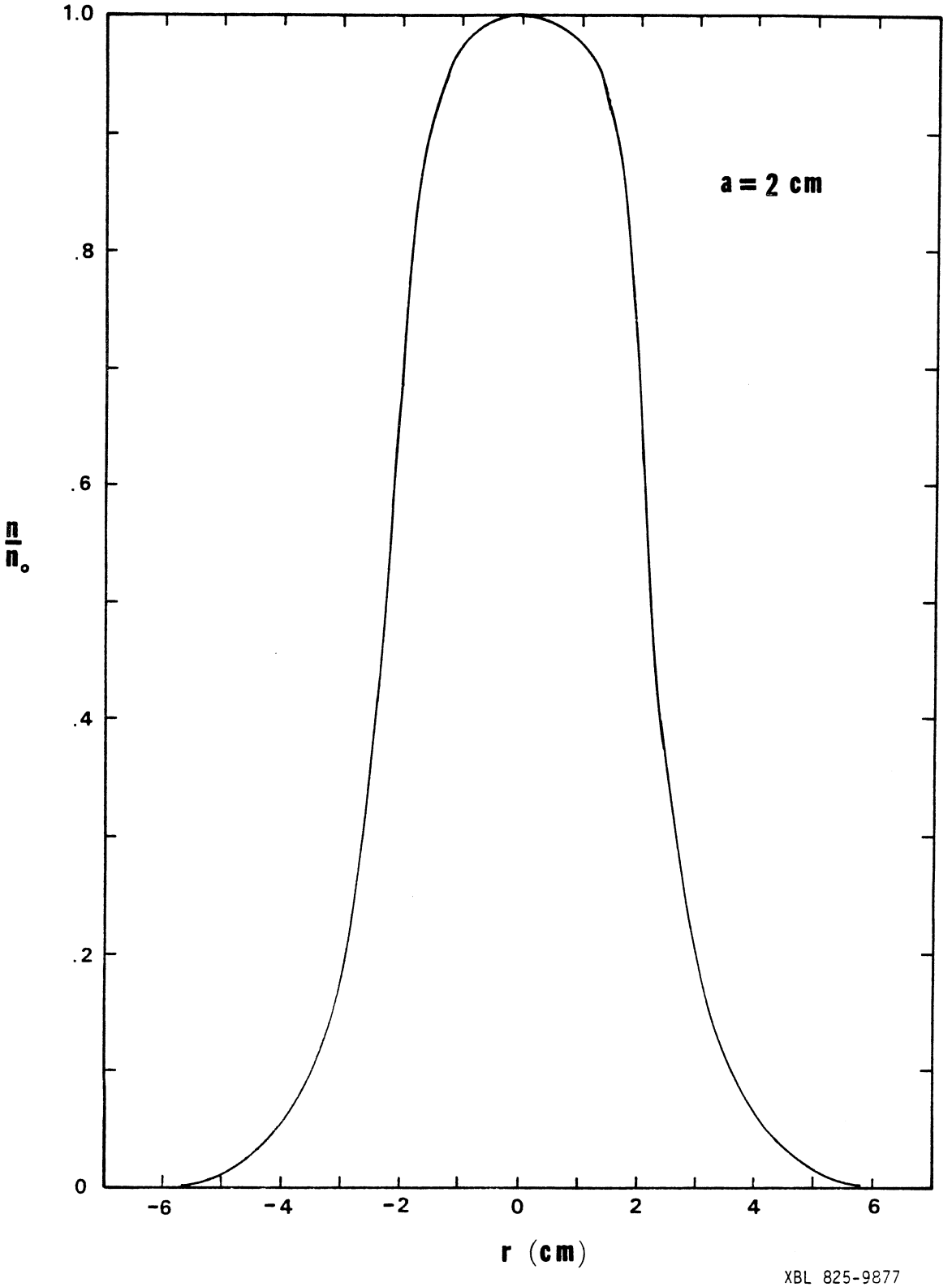

Figure 11

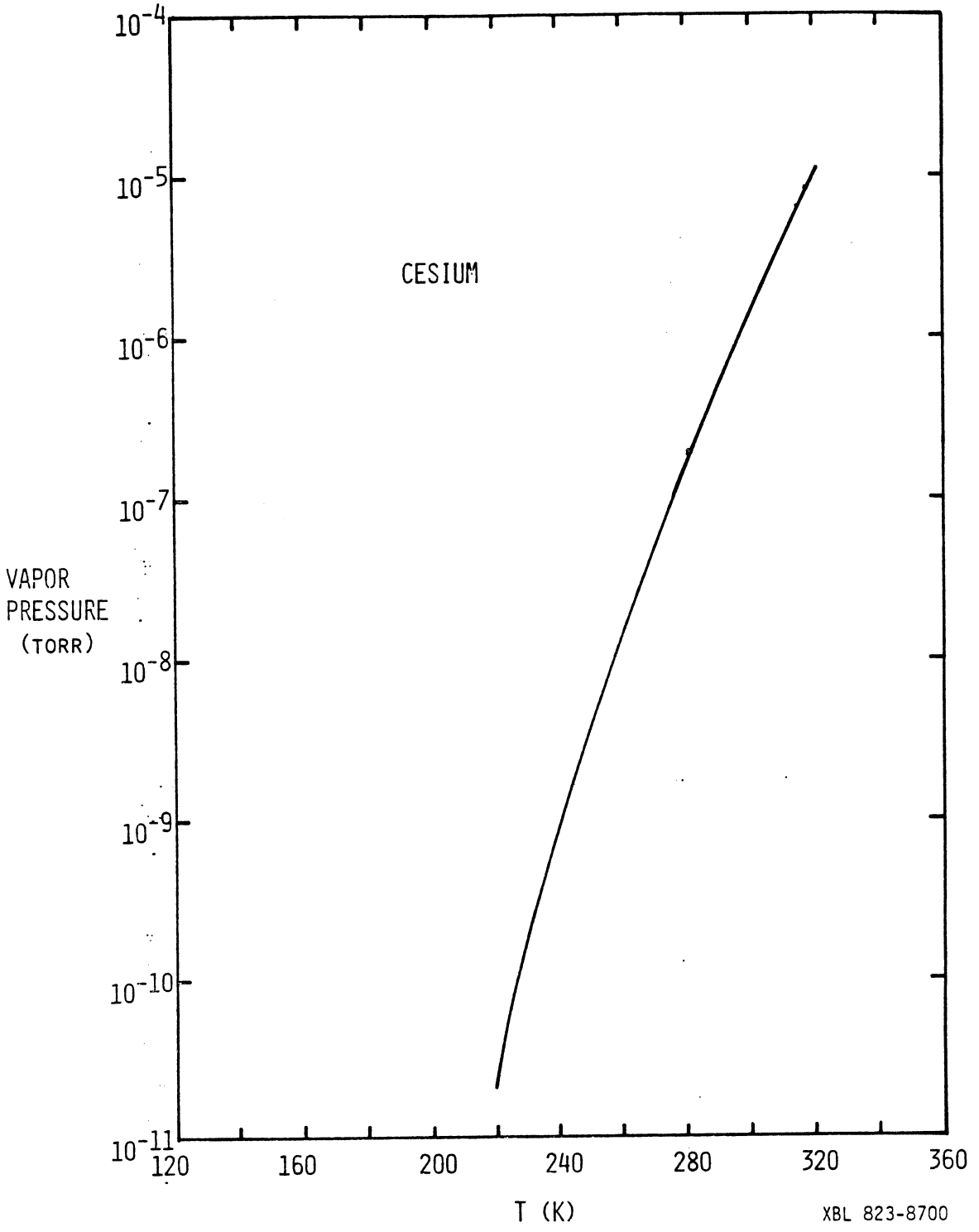

Figure 12. Vapor pressure of cesium as a function of temperature. The density of cesium vapor at the wall temperature was about 10^7 cm^{-3}.

parameters which are difficult to determine experimentally. Thus Fig. 11 can only be used to qualitatively confirm the plasma density variation. In practice, factors such as the hot plate temperature distribution and magnetic field variation and turbulence influence the density profile much more drastically.

III. Degree of Ionization

Since a plasma usually consists of ions, electrons, and neutral atoms, the usefulness of plasma targets are not readily apparent if one wants a pure target of one species. It has been shown in the previous chapter that electrons are unimportant as far as Cs^{++} formation is concerned. However the presence of cesium atoms in the target can pose serious problems in the determination of the cross section because of reactions of the following type:

$$Cs^{+} + Cs^{o} \rightarrow Cs^{++} + e + Cs^{o} \qquad (4.18)$$

Thus it is necessary to know the degree of ionization of the plasma. Also the presence of other impurities such as O_2 and N_2 and H_2 also may adversly affect the target. Such backgrounds can be handled experimentally by chopping the plasma target to look at backgrounds separately from signal plus backgrounds. This is done in the experiments by chopping the plasma on and off.

The plasma confinement chamber was far from thermal equilibrium when the plasma was operating. The walls were cooled by liquid nitrogen to approximately-120 C. The hot plate was at approximately 3000 K. The atom spray was directed towards the hot plate and away

from the plasma interaction region as can be seen in Fig. 7, Chapter 3. Thus the neutral atom density was probably high in the region behind the hot plate. Atoms which struck the hot plate and were not ionized presumably were evaporated in a very short time and most likely were directed at the interaction region. The neutral density should fall off as $1/z^2$ where z is the distance from the hot plate. Due to the fact that the interaction region is effectively a cryopump for cesium atoms due to the low vapor pressure at-120 C, it was estimated that the cesium neutral density was 10^7 cm^{-3} at the target region. The vapor pressure of cesium[30] is shown in Fig. 12. This was negligible compared to the plasma density in this region. If it is assumed that the sticking coefficient is one for a cesium atom striking a cold metal surface, then the effective pumping speed of the cryopumped region is given by

$$S = 3.64\ (T/\ M)^{12}\ \text{liters/sec cm}^2 \qquad (4.19)$$

Even if it is assumed that the neutral temperature is at room temperature, with a surface area of 3500 cm^2, the pumping speed approximately is 20,000 liters/sec. This is very large pumping speed and should keep the cesium atom density to a minimum in the target region. Typical operating pressures were in the low 10^{-7} Torr range after several hours of outgassing. It is assumed that most of the background pressure is due to non-pumpable gases such as H_2. The fact that the F++ fractions measured by chopping the plasma intersect 0 near the zero of plasma density lends support

that the background was not a severe problem for the later experiments.

IV. Plasma Stability

Q Machine plasmas were studied extensively in the past to elucidate plasma stability theories. These types of plasmas are current free, except for diamagnetic currents which are weak, and hence these plasmas usually are free of gross MHD instabilities. This is true even if the field is solenoidal with no shear present. Usually this stability has been attributed to ion-ion collisions leading to viscous damping of the unstable MHD modes.

Experimentally, unstable modes were found to exist for the plasma of this experiment. Presumably the instability is due to the radial inhomogeneity of the plasma. These instabilities usually are referred to as drift waves.[31]

These unstable modes were not studied extensively because this was not the primary purpose of this experiment. The following observations were noted. At low densities, the plasma usually was quiescent. As the density was raised, sometimes the signal to the probe became noisy, and at times, a coherent wave structure could be seen on the ion saturation current of the probe. A typical example of this coherent oscillation is shown in Fig. 13. The oscilation frequency was measured to be 4.5 khZ for this case. The frequency of the oscillation was not constant for all operating conditions of the plasma. The plate temperature as well as the magnetic field strength seemed to play important roles. It is hypothesized that

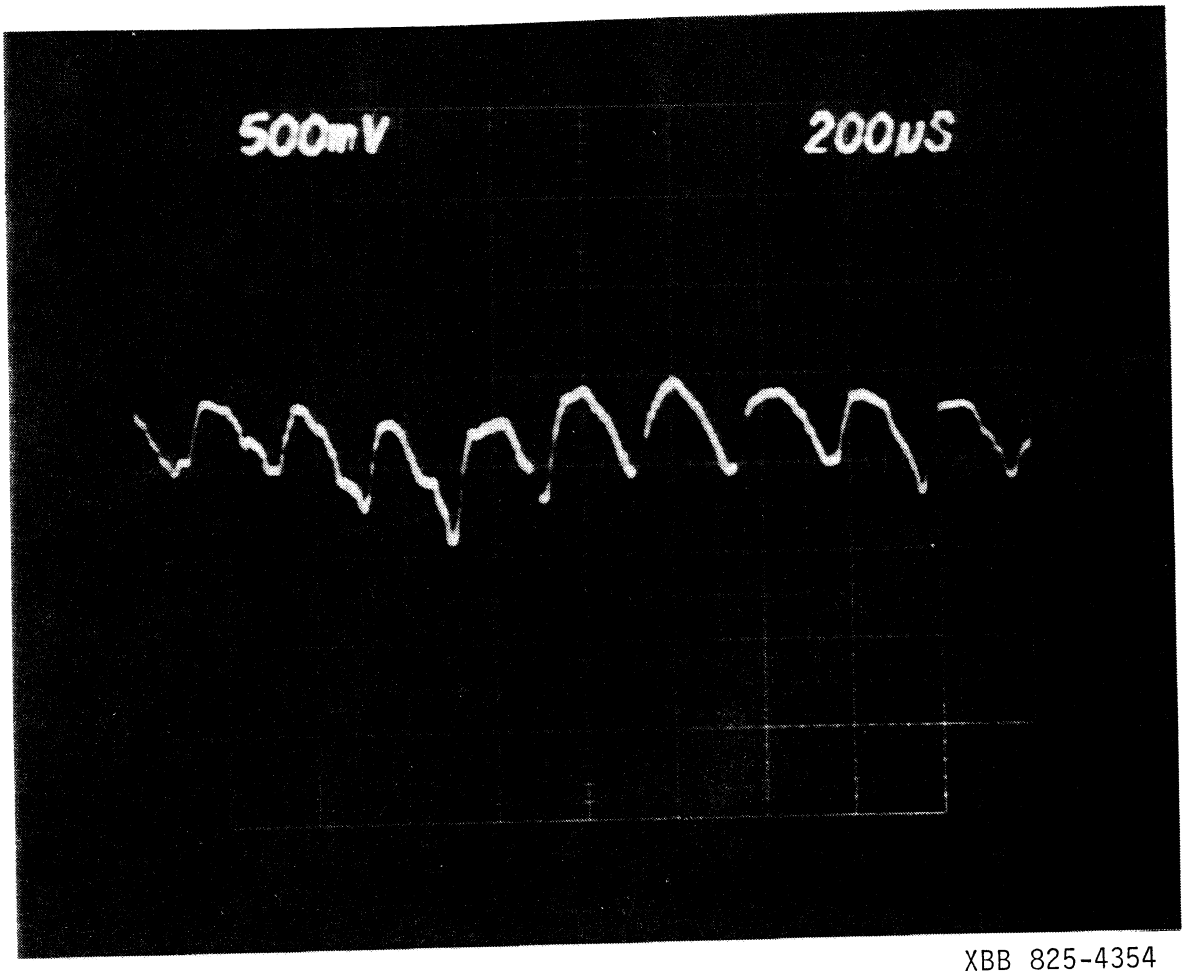

XBB 825-4354

Figure 13. Coherent waves observed in Q machine plasma. $\delta n/n \sim 10$ percent.

these were indeed low frequency drift waves. Drift waves are known to have frequencies which are determined by the gradient of the plasma density. The drift frequency is given as

$$w^* = \frac{c\, k_\theta\, T_e}{e\, B\, L_n} \tag{4.20}$$

where L_n is the density scale length.

For the conditions relevant to this plasma, if $k_\theta = 4\ cm^{-1}$, $L_n = 1$ cm the above frequency approximately is 7.9 kHz. This approximately is what was observed for the unstable plasmas. We did not try to measure k_θ.

The impact of these instabilities on the performance of the experiment was slight. The oscillation frequencies were high enough to be completely averaged out over a data acquisition cycle.

The major effect on the plasma was probably the heating of ions and electrons due to the fluctuating field associated with the instabilities. In thermal equilibrium one would expect the ion and electron temperatures to be equal to the hot plate temperature. In practice, this would lead to temperatures of approximately 0.25 eV. The unstable plasmas usually had electron temperatures well in excess of this; anywhere from 0.3 eV to 0.45 eV. These temperatures were taken into account in the analysis of the probe data.

CHAPTER 5

APPARATUS

A. Ion source and Accelerator

The beams were accelerated in a 250 kV electrostatic accelerator shown schematically in Fig. 14. The Cs^+ ion source consisted of a commerical porous tungsten plug which was impregnated with β-eucryptite. Upon heating this plug[32] to ~ 1100°C with the imbedded filament, Cs^+ ions were emitted from surface. These ions were extracted by electrodes in a Pierce geometry. The typical extraction voltage was approximately 3 kV. Ion trajectories in the source were computed with the aid of the code EBQ[2] and produced a fairly parallel beam. The beam then entered an acceleration tube with 22 grading electrodes; each electrode was set at a voltage determined by a resistive voltage divider. The Cs^+ ion source was at terminal potential and therefore the beam energy was equal to the terminal voltage. The terminal voltage was calibrated with a known standard meter and was found to be accurate to within 1 percent.

The ion source had a lifetime of several hundred hours under usual conditions. It was possible to reactivate the sources by making a β-eucryptite compound and covering the pourous plug with this compound.[33]

The pressure in the source was usually about 5×10^{-7} torr. After acceleration, the beam was focused by two electrostatic quadrupole lenses oriented at 90° to each other. The focused beam

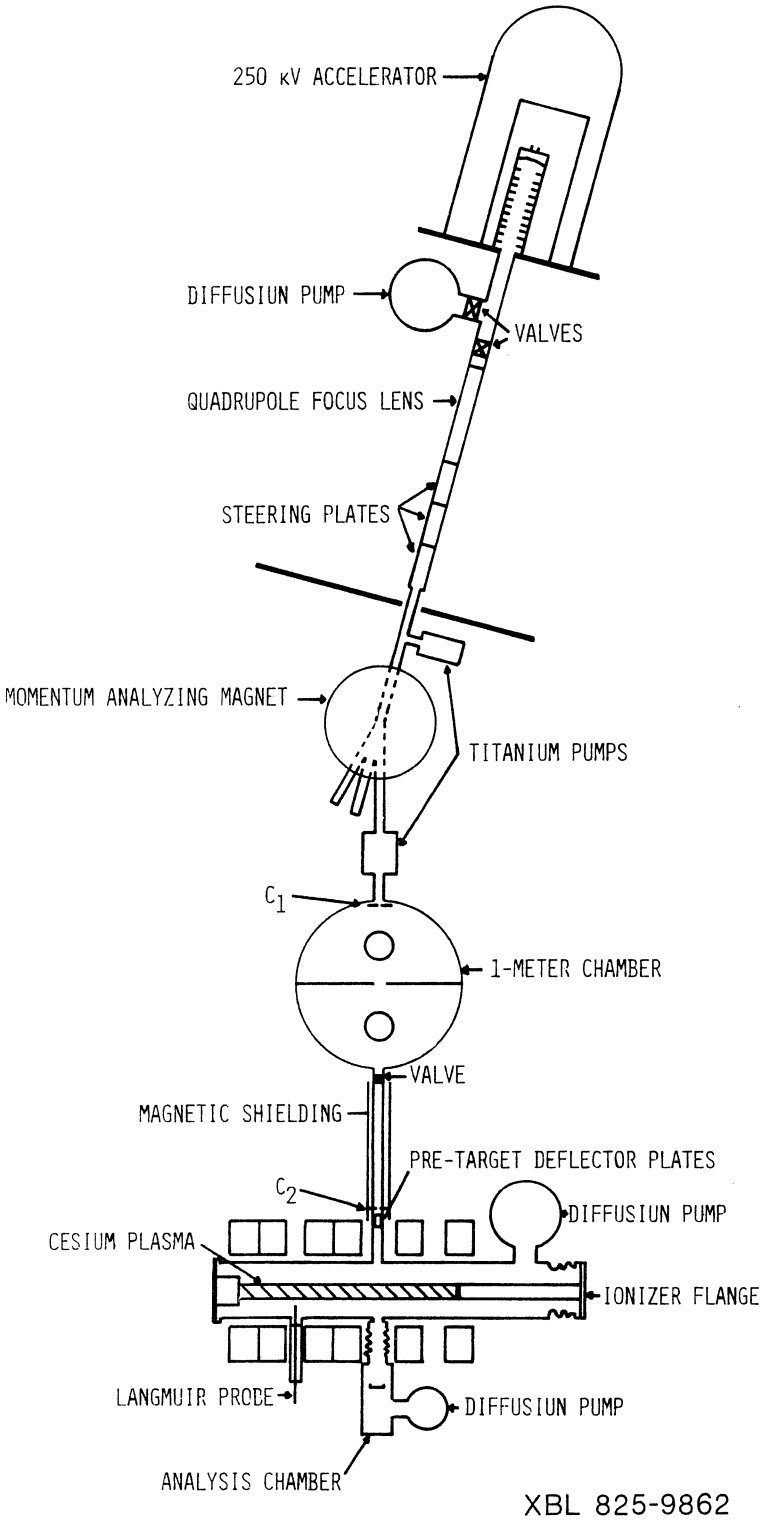

Figure 14. 250 kV accelerator system and experimental area.

entered a steering plate section with two vertical sets of steering plates and one horizontal set of steering plates. Then the beam entered a bending magnet which momentum analyzed the beam. The bending angle was approximately 15°. The purity of the beam was insured by using this magnet to select only the correct mass ions to be sent to the plasma target.

The plasma target was located approximately 5 m from the bending magnet. A large vacuum chamber approximately 1 m in diameter which was used for other experiments, served as a beam line. The first collimater, C_1, was located in the entrance to this chamber. Just before C_1 was a titanium pump which pumped the beamline section before the vacuum chamber. The vacuum chamber was pumped by two diffusion pumps and was usually at approximately 2×10^{-7} torr.

The beam then entered a final beamline where the second collimator, C_2, was located. After the second collimater, a set of vertical steering plates allowed the beam to be moved vertically to correct for the upward movement of the beam in the solenoidal plasma confinement field.

B. Plasma Target Chamber

The plasma target chamber is shown in Fig. 15-17. The chamber consisted of a special coaxial pipe with a jacket that was used for cooling the chamber walls. The chamber was oriented such that the axis of the tube was at 90° to the beam line. It was originally intended to have the beam traverse the tube axially, to provide a longer target, but this proved to be unfeasable due to outgassing of

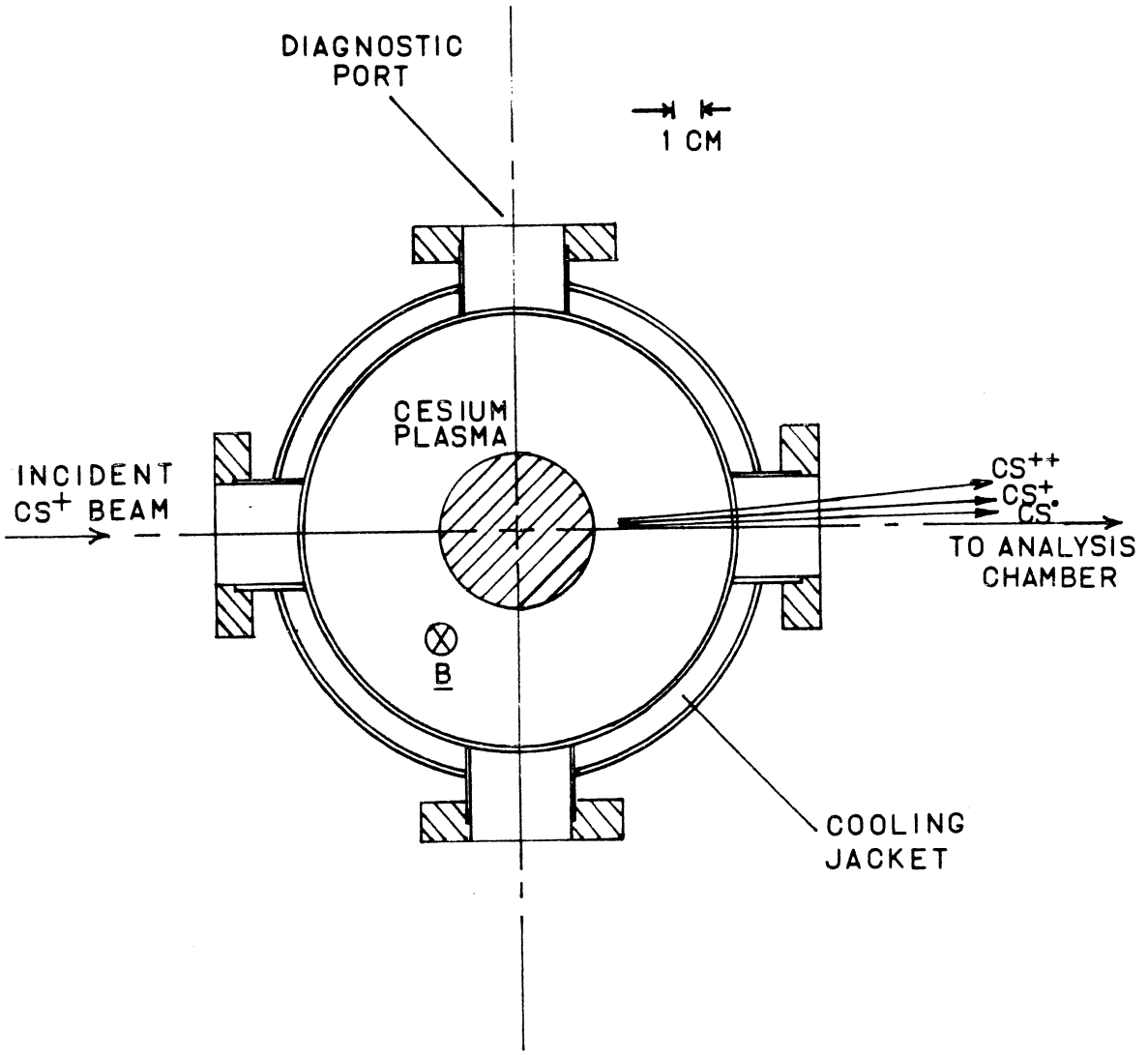

Q MACHINE PLASMA TARGET
END VIEW

XBL 7911-12628

Figure 15

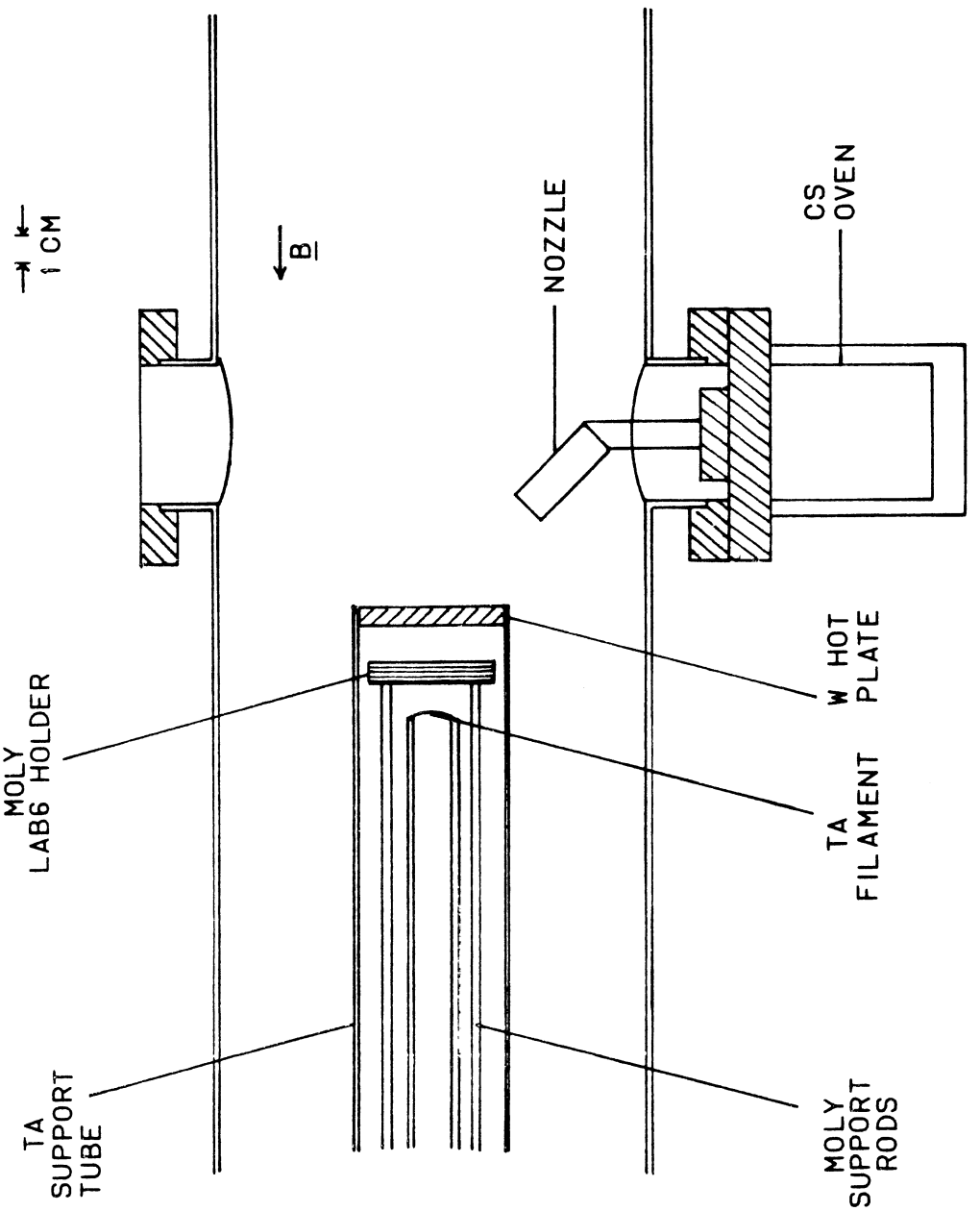

XBL 7911-12661

Figure 16

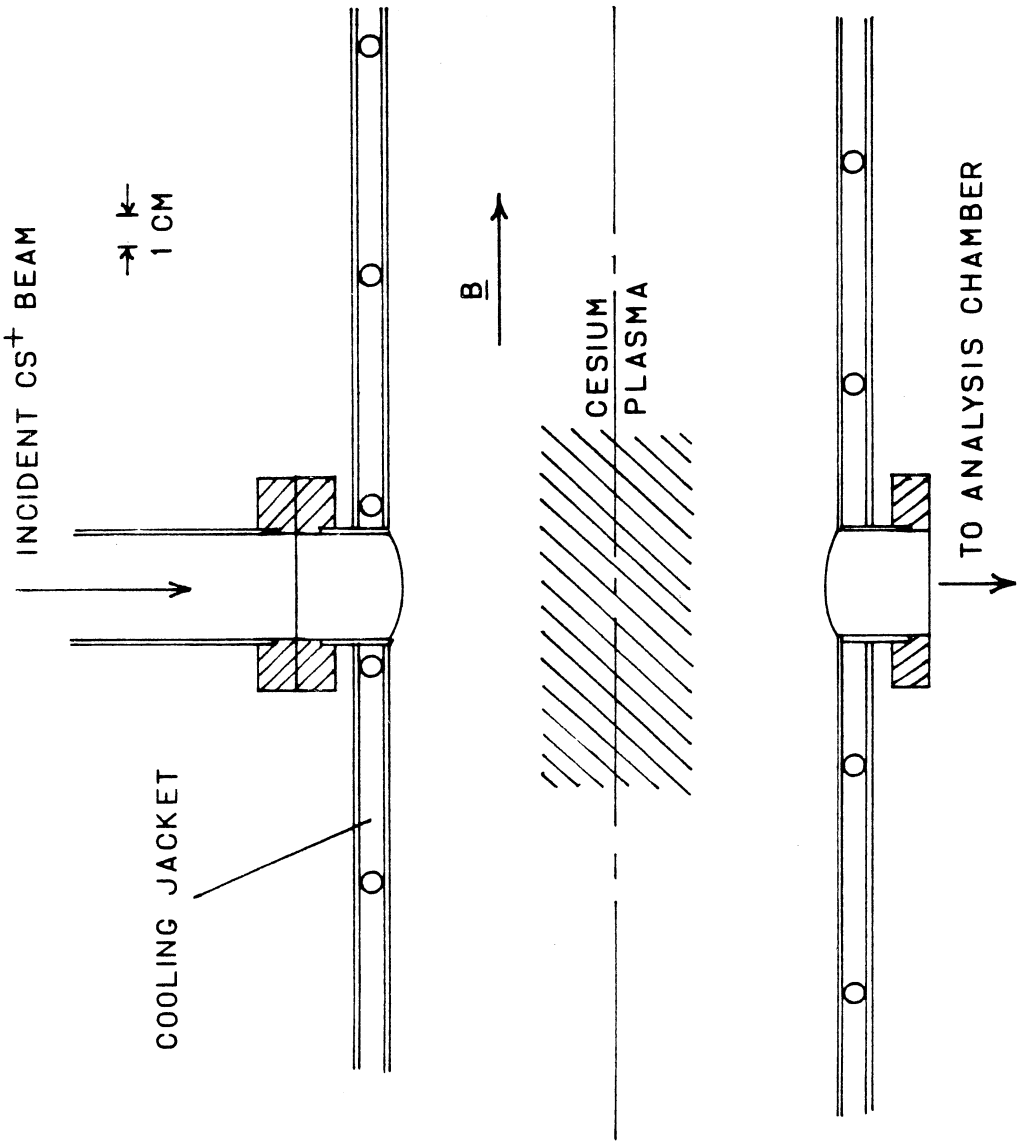

Q MACHINE PLASMA TARGET

Figure 17

XBL 7911-12629

the cathode and large scattering of the beam, limiting the acceptance angle of the detector array. Thus, all experiments were finally done with the chamber oriented for transverse (to the solenoidal $\underline{B}$ field) beam injection. This significantly lowered the plasma line density and neccesitated the design and construction of the secondary emission detector (see Appendix B).

The chamber sat inside six water cooled solenoid magnets. The solenoid magnets were driven by a 60 kW motor-generator set which was current regulated. The spacing of the coils were such to allow access through the eight 1-1/2" diameter diagnostic ports. All flanges were Varian conflat flanges made of stainless steel and OFHC copper gaskets were used for all flanges. The chamber was also 304 stainless steel. In addition to these flanges there were two 2" diameter flanges. One was used for the cesium oven and the other was used for the plasma chopper. The cesium oven is shown in Fig. 18.

The magnetic field primarily was a solenoidal field, but was somewhat non-uniform due to the spacing of the coils to allow access to the plasma. Typical axial and transverse magnetic field profiles are shown in Figs. 19 and 20. The maximum fields were on the order of 4 kG. The magnetic field was set by the requirement of separating the Cs^{+} and Cs^{++} beams of a given energy. Thus, when higher energy (240 keV Cs^{+}) beams were used, the magnetic field was stronger than when lower energy beams (100 keV Cs^{+}) were run.

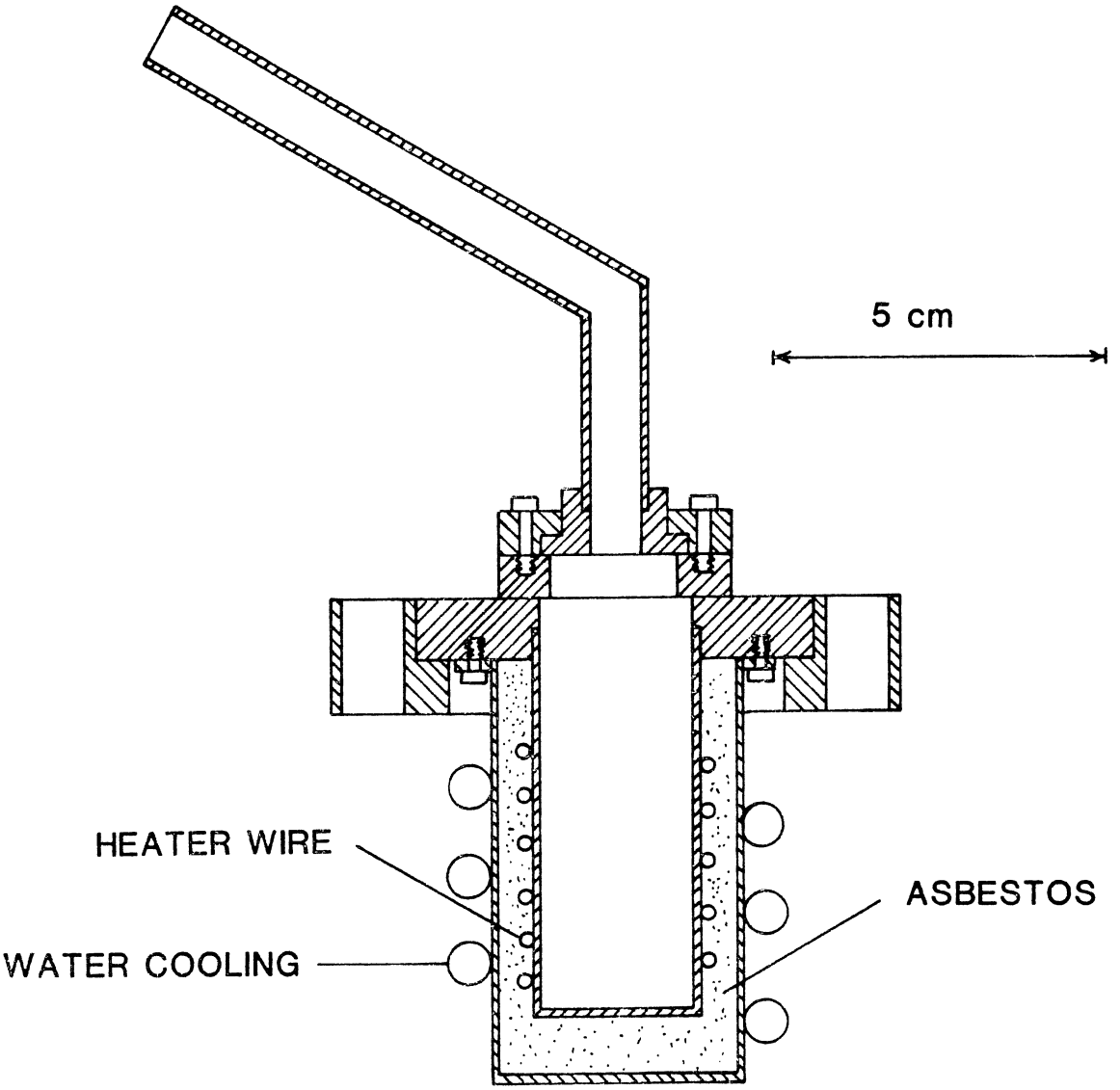

Figure 18. Cesium oven. Heating coils were used to heat the oven and external water cooling coils were used for quick oven cool down.

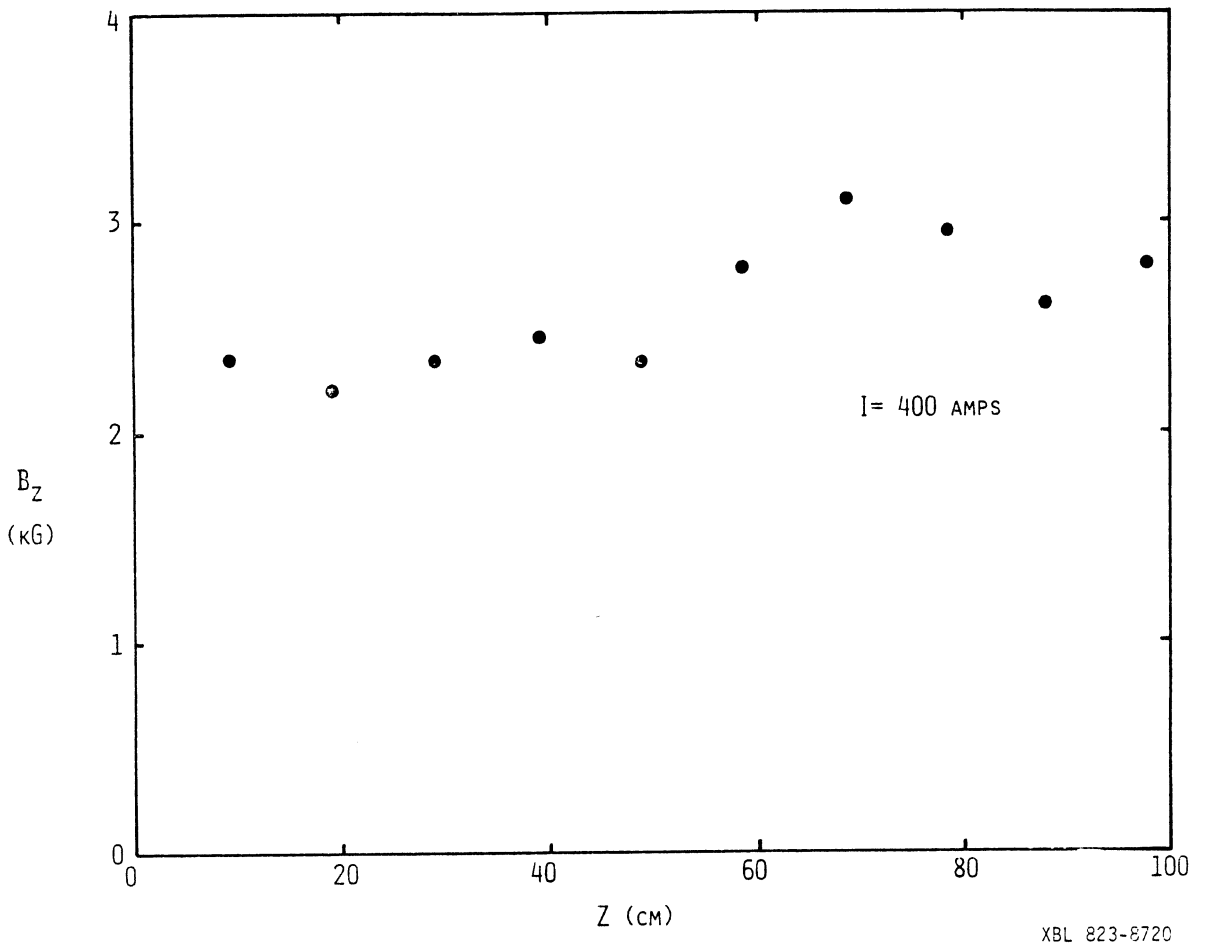

Figure 19. On-axis magnetic field strength as a function of axial distance for solenoidal plasma-confining coils.

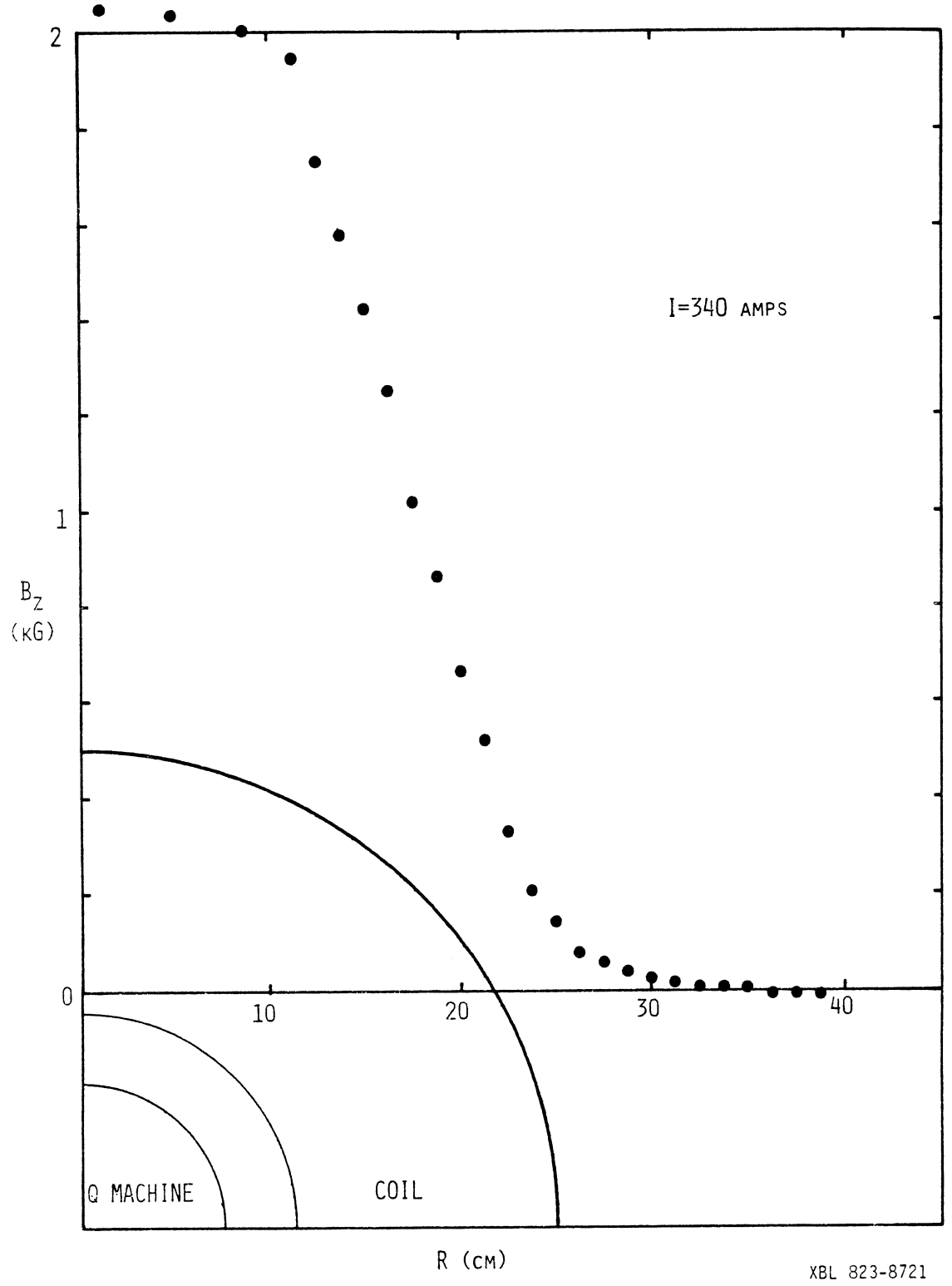

Figure 20. Radial scan of axial magnetic field strength at the beam injection port.

Figure 21. Analysis chamber in final configuration as attached to the target chamber with a bellows.

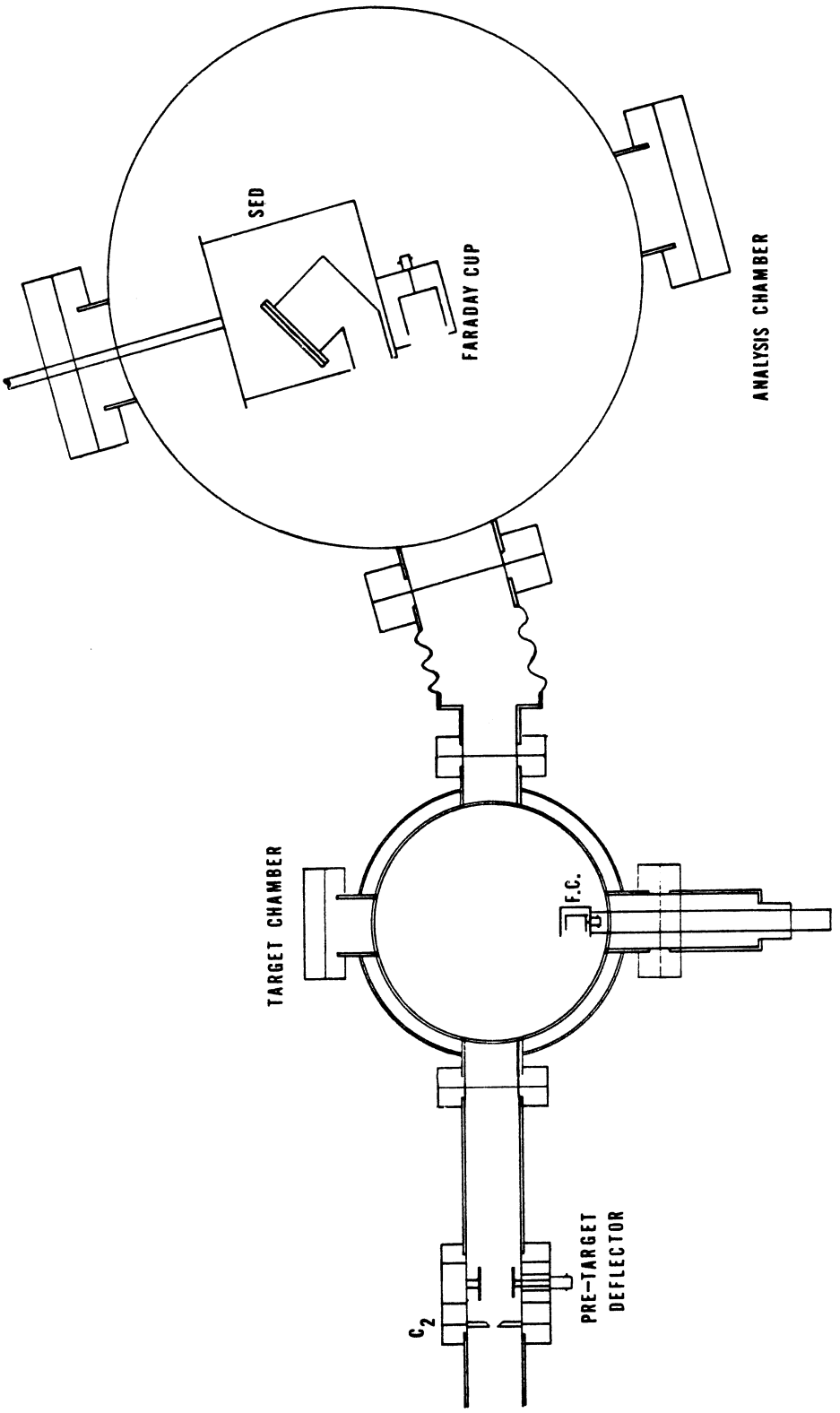

XBL 825-9989

Figure 21

C. Analysis Chamber

The stainless steel analysis chamber was connected by bellows to the plasma target chamber. The arrangement is shown in Fig. 21. Initial design of the system with axial beam injection had the analysis chamber at the cold plate end of the plasma target chamber and the analysis chamber was horizontal. A transverse electric field created by two parallel plates separated the Cs^{++} and Cs^{+} components of the beam. After it was found that scattering of the beam neccesitated transverse injection, the analysis chamber was moved to the final location at 90° to the axis of the plasma chamber. The analysis chamber also was rotated by 90° so that the base of the chamber lay in a vertical plane. This allowed more freedom of movement for the detector array which could be moved vertically through a Wilson seal to scan the fan of the beam as it exited the plasma target chamber.

The analysis chamber was a 35 cm diameter 316 stainless steel chamber with a port to allow a 4" pumping stack to be connected by a 90° elbow. The pumping stack consisted of a valve, liquid nitrogen trap and a 4" diffusion pump (Neovac Sy manufactured by Varian Associates, Inc. was used as the pump fluid in all diffusion pumps). Typical base pressures in the analysis chamber were in the low 10^{-7} range. Electrical connections were made through Varian conflat flanges with vacuum tight BNC connectors. The lid of the analysis chamber was sealed by a Viton O ring and clamped down by eight bolts. Roughing down the analysis chamber was through the bellows and the plasma target roughing valve. It typically took

approximately 24 hours to pump the system from atmospheric pressure to the ultimate system pressure.

D. Detectors and Diagnostics

The beam and plasma were diagnosed by several methods.

1. Langmuir Probes

Langmuir probes were used for measuring plasma density. The probe was located 30 cm down stream from the beam-intersection region. The probe analysis and circuitry is described fully in Appendix A.

2. Faraday Cups

The incident beam current was measured with a Faraday cup connected to an electrometer (Keithley, Model 610C). Several cups were located along the beamline. The Faraday cup in the analysis chamber was magnetically suppressed in order to stop secondary electrons from altering the actual beam current. The retractable Faraday cup located in the Q machine was not suppressed with ceramic magnets, but was suppressed by the solenoidal field. A typical suppression curve us shown in Fig. 22. The retractable Faraday cup was used to insure that the beam current incident on target was the same as the current detected at the analysis chamber.

3. Secondary Emission Detector

The secondary emission detector was used to detect the Cs^{++} component of the beam. Faraday cups were not sufficient because even with magnetic suppression, it only was possible to

suppress secondary electrons by a factor of 10^3. Since the Cs^{++} component was ~ 10^{-5} of the incident beam, stray electrons tended to swamp the desired Cs^{++} current. The secondary emission detector is described in Appendix B.

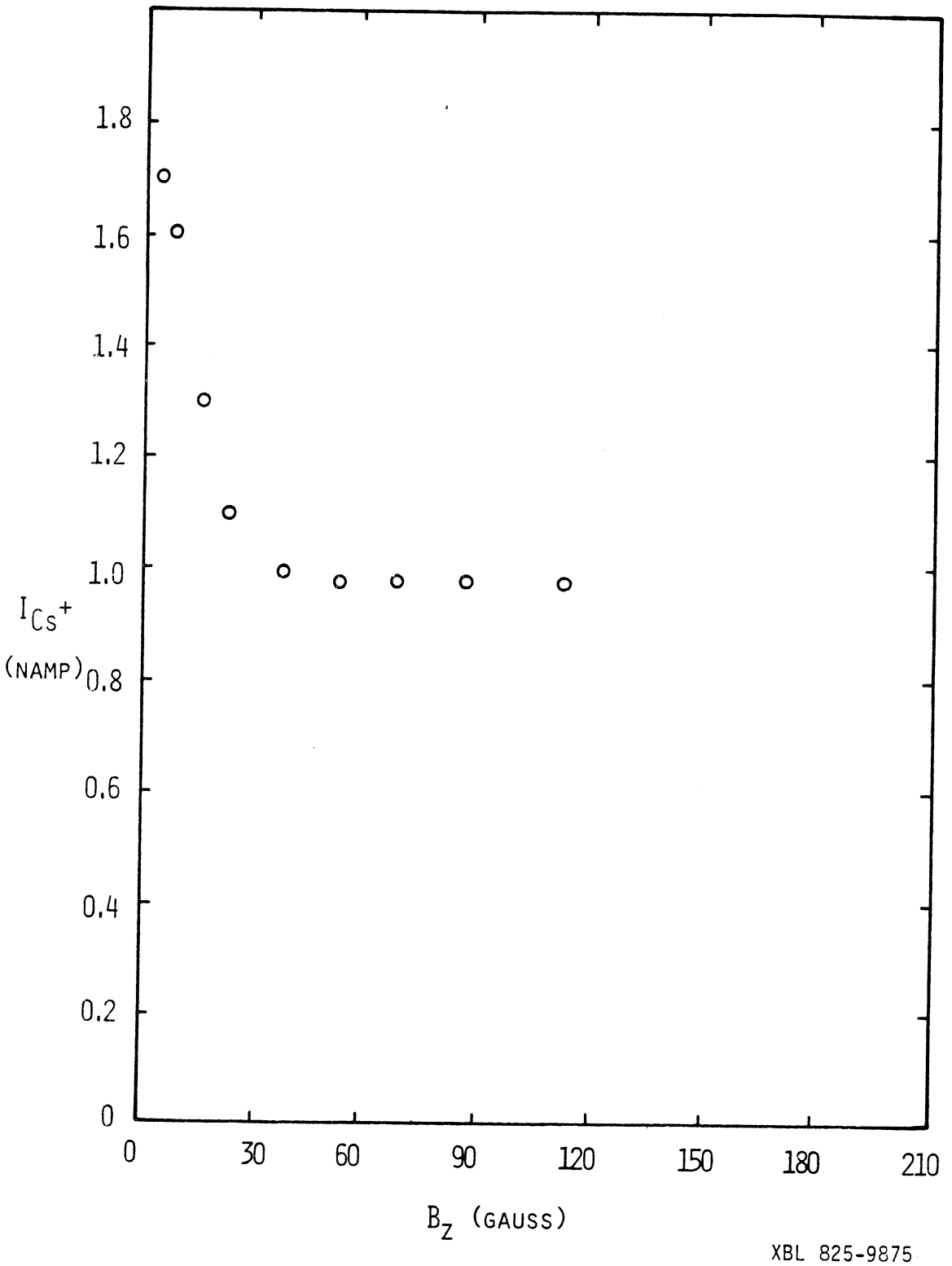

Figure 22. Faraday cup suppression curve. Secondary electrons were suppressed above 40 gauss.

CHAPTER 6

PROCEDURE AND DATA ANALYSIS

Procedure

The operation of the plasma as a target for an ion beam collision study entailed many factors not normally associated with Q machine plasmas. These procedures are described in this section.

I. Cs Oven Cleaning

A charge of 5 grams cesium was enough for typically ten hours of plasma operation. After it was determined that no plasma was found due to a lack of cesium in the oven, the cathode was turned off and the LN cooling of the jacket was stopped. The cesium oven was turned off but the water cooling was kept on to facilitate oven cooling. Water cooling on the plasma chamber ends was also continued to prevent them from freezing due to conduction by the cold central region. Approximately 12 hours after an experiment was finished, the chamber was fully equilbrated to room temperature and the water cooling was turned off. The water cooling to the cesium oven was turned off and the lines to it were disconnected. The electrical heating wires were also disconnected. The analysis chamber and plasma target chamber were simultaneously brought up to atmospheric pressure by purging with argon gas. The oven was demounted from the plasma chamber and placed on a table for observation to confirm that there was no cesium metal left in it. After the nozzle was removed and the lack of cesium metal was

visually confirmed, the oven was taken outside and placed on the ground on its side. Cleaning the oven took several steps: First, a heavy alcohol was used to flood the oven. After all reactions (with residual cesium) ceased, a second purge with ethanol and then a third purge with methanol was performed.

This usually was sufficient to clean all cesium from the oven. On several occasions the methanol caught fire due to the heat of reaction but the situation was safe due to handling outside in an open area away from all flamable objects. Metal-X was on standby at all times to extinguish any alkali metal fire (none occured). The oven then was carefully sprayed by a water jet from a bottle to flush all reacted cesium from the oven. The oven was brought inside and fully flushed with tap water. Reacted cesium compounds stuck to the oven were removed by cotton swabs and ethanol was used to clean the oven further. After a final rinse with methanol the oven was hooked up to the heating variac and warmed by low power to evaporate all remaining liquid.

II. Loading Cs Oven

The cleaned cesium oven and nozzle then were placed in an airtight glove box with all necessary tools and a new Cs ampoule. The glove box was purged for approximately 1/2 hour with argon to drive away all air. Working with argon flowing in the box allowed the breaking of the ampoule and the loading of the cesium into the oven without reacting too much cesium metal. The cesium in the ampoule was usually solid but could be melted by (m.p. 29°C) holding

the ampoule in the rubber gloves for several minutes. The melted cesium then was poured into the oven and the nozzle was bolted on with a small copper gasket to seal it. The oven was quickly removed from the glove box and mounted back on the plasma chamber. Alignment of the nozzle with the cathode was done visually thru the cold plate end flange such that the nozzle pointed directly at the tungsten hot plate. All flanges were connected and the chamber was roughed down.

III. System Pump Down

Roughing the chamber took approximately 0.5 hour to reach 50 millitorr. After closing the roughing valve the main diffusion pumps could be opened and this brought the chamber to 10^{-5} torr within about 10 minutes. Pumping overnight with mild bakeout (80°C) brought the system to an ultimate pressure of 10^{-7} torr. All experiments initially were started in the low 10^{-7} torr range. All beam line pumps were turned on the day of each experiment and the typical operating pressures were in the low 10^{-7} torr range.

The accelerator was pumped by a 6" diffusion pump stack with a liquid nitrogen trap. Typically, it ran in the mid 10^{-7} torr range.

IV. Beam Tuning and Operation

After the entire system was pumped down the accelerator was turned on and the desired beam energy was set by the accelerator H.V. power supply. The plasma confinement coils were energized by

the m.g. set and were set to the proper field strength to make the beam traverse the plasma target chamber and enter the analysis chamber. The pre-target deflecter plate voltage was also set to the proper value to bend the beam downward to correct for the upward movement of the beam in the magnetic field.

The cesium ion source and all focus and steering plates were turned on. The beam initially was tuned by letting it run straight down the accelerator and into a Faraday cup placed on the 0° axis of the accelerator just past the momentum analyzing magnet. With no collimation we could typically expect 10^{-4} amps with moderate ion source heater power. After a brief warm up time (usually about 15 minutes) all power supplies and heaters were stable. The bending magnet then was energized and set to the value needed to bend the desired energy beam into the beamline where the plasma target experiment was located. After passing thru two collimators, the beam hit the Faraday cup in the analysis chamber. The beam was tuned for maximum current, and the ion source heater was adjusted to bring the incident beam current to approximately 10^{-11}A (approximately 10^{8} particles/sec).

The secondary emission detector then was turned on and all voltages were set to the operating points determined by the efficiency measurements (see Appendix B). There was usually some beam related background which was presumed to come from residual gas in the plasma target chamber. The detector dark current when the beam was turned off (by closing a beamline valve) was extremely low (~2

counts/sec) when the pressure in the chamber was in the low 10^{-7} torr range.

V. Plasma Operation

With the beam running continuously, the plasma then was turned on. It took approximately one hour to get the plasma working optimally. The magnetic field was already on and was set by beam bending requirements (see Appendix D). The cathode was heated in several steps. First, the cathode H.V. supply was turned on to +1 kV. The cathode filament current then was slowly raised keeping the plasma chamber pressure below 10^{-5} torr. Electrons from the filament (at ground potential) struck the moly LaB_6 holder and heated it by electron bombardment. The filament usually was heated to incandescence and took ~ 45 amps at 6 volts. At this time the cathode power supply drew approximately 1 ampere, giving a total bombardment power of one kilowatt. The cathode voltage then was raised such that the total bombardment power was approximately 1.5 k watt. The enclosed moly LaB_6 holder then heated the Tantalum hot plate holder and hot plate by radiation to ~ 1000°C. It then was possible to switch polarity on the moly LaB_6 holder to approximately - 1.5 kV. Since the LaB_6 is very much more emissive, electrons from the LaB_6 struck the tungsten hot plate and heated it to ~ 2000°C. Since the hot plate heated the moly LaB_6 holder by radiation, it was possible to completely turn off the filament at this point. The cathode ran in a stable space charge limited operation. At this time the liquid nitrogen cooling

of the plasma chamber jacket was initiated and a stable inside wall temperature of approximately - 140°C was reached within about 15 - 30 minutes. The temperature was measured with a chromel-alumel thermocouple that was fixed to the inside vacuum wall by a high vacuum epoxy.

The cathode voltage then was increased slowly to approximately 1.8 - 2.0 kV and the current rose to ~ 3 amps. This resulted in a hot plate temperature of ~ 2800°K. The plate temperature was monitored in early tests by optical pyrometer and was found to be reasonably constant over the face of the cathode (Appendix E) This is due primarly to the coaxial design of the gun. Radial temperature gradients of hot plate temperature were not considered to be bad because they give rise to azimuthal plasma drifts. However azimuthal temperature gradients are deleterious to plasma confinement because they give rise to radial drifts. The coaxial hot plate design minimizes the azimuthal temperature variation.

At this point the cesium oven was turned on. A variac was used for the heater power supply. Typical variac voltages of 10-15 volts heated the oven to ~ 100°C on the outside surface. This caused the cesium metal in the oven to melt and cesium vapor streamed out of the nozzle and was directed at the hot plate. No attempt was made to collimate the atomic cesium beam.

The movable Langmuir probe was placed such that the probe would detect the plasma. As the oven heated up and the cathode power was increased, a plasma developed as detected by the probe signal. After approximately 15 minutes, all temperatures were stable and the

plasma was stable. Both stationary and moving probe traces were taken. Stationary probe traces had the probe position fixed and the probe bias was varied between -10 and +10 volts yielding a characteristic curve. This gave information on the plasma floating potential and electron temperature. Typically three characteristic curves were taken in close succession to ensure the repeatability of the measurements.

Next, moving probe data was obtained by using the driving motor and probe assembly to scan the plasma radially. The probe bias was fixed, usually at -10 volts to collect the ion saturation current. This data, in conjunction with the fixed probe data, was analyzed by the Laframboise theory and yielded a point by point determination of the plasma density (see Appendix A). The density profile was integrated numerically and yielded a radial plasma line density. (See Fig. 23).

The probe then was set to the position corresponding to the maximum in the density and the bias was still fixed at -10 volts.

The plasma chopper then was actuated and the plasma was turned on and off by the passage of the rotating plate across the face of the hot plate. This also actuated a gate signal for counting plasma ON and plasma OFF data. A counter shot was initiated and yielded a Langmuir probe count related to the total number of charged particles collected by the probe in the time that the ON gate was open. The density at this point was assumed to be proportional to the quantity Langmuir probe counts/ON time.

Figure 23. Plasma density versus radial position. Probe bias was fixed while probe was scanned radially. Data points were taken every 100 ms. Data analyzed according to Laframboise theory.

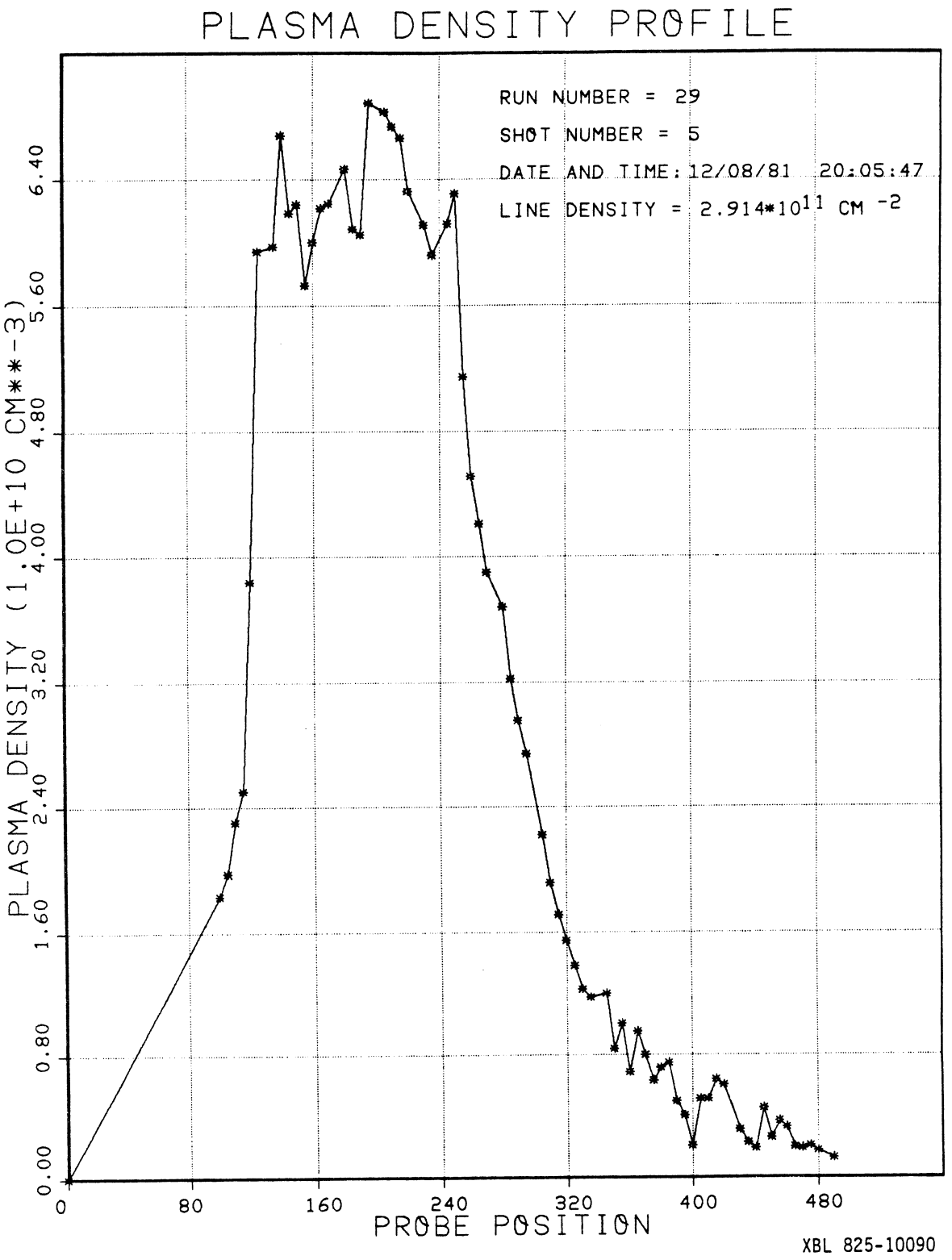
PLASMA DENSITY PROFILE
RUN NUMBER = 29
SHOT NUMBER = 5
DATE AND TIME: 12/08/81 20:05:47
LINE DENSITY = 2.914*10^11 CM -2
PLASMA DENSITY (1.0E+10 CM**-3)
0.00
0.80
1.60
2.40
3.20
4.00
4.80
5.60
6.40
0
80
160
240
320
400
480
PROBE POSITION
XBL 825-10090

Figure 23

Figure 24. Data acquisition system. Abbreviations are as follows: sed=secondary emission detector, sca=single-channel analyzer, pha=pulse height, fc=Faraday cup, scope=oscilloscope, remac=remote data acquisition module, modcomp=Modcomp IV computer.

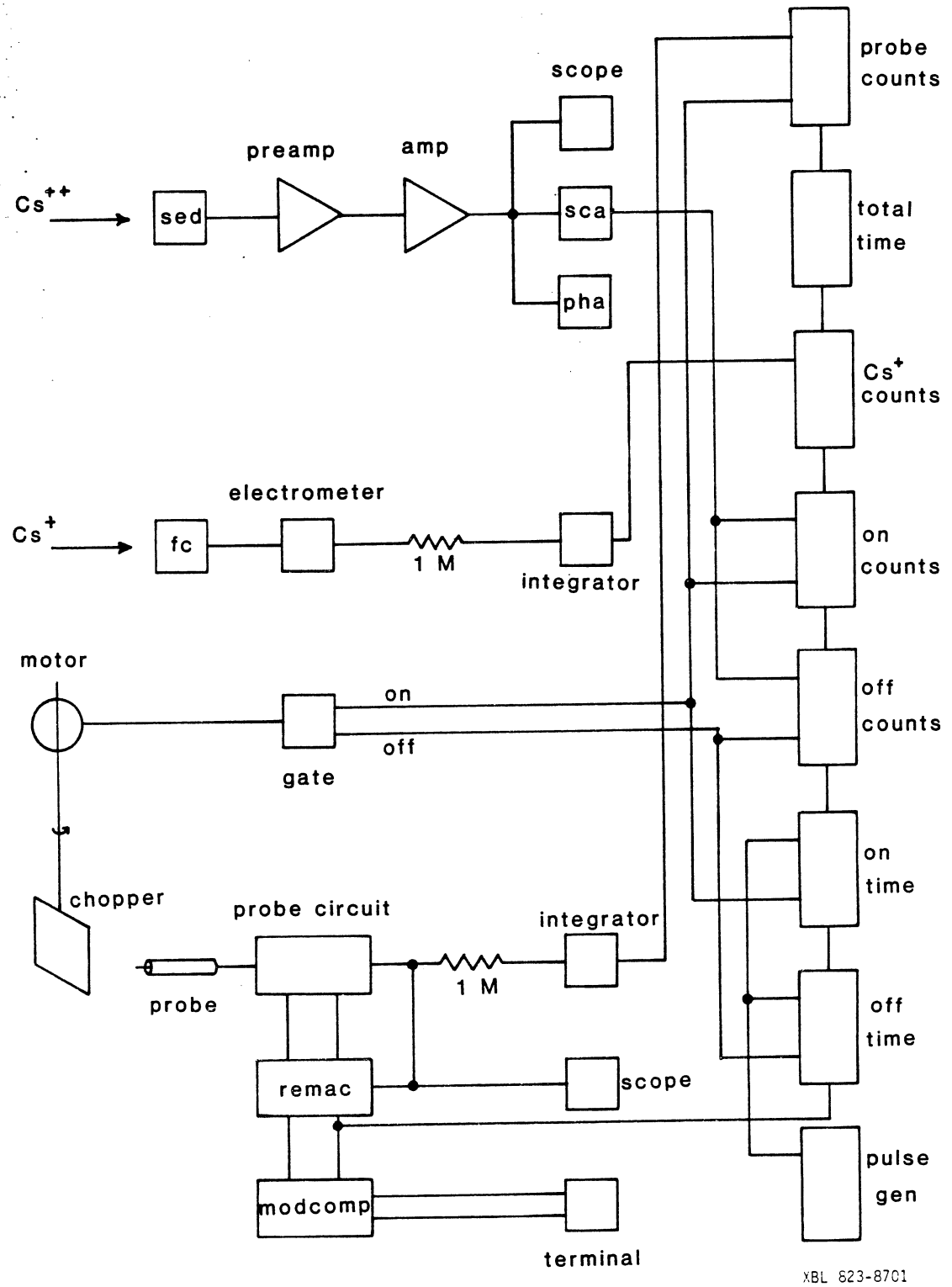
probe counts
scope
preamp
amp
Cs++
sed
sca
total time
pha
Cs+ counts
electrometer
Cs+
fc
1 M
integrator
on counts
motor
on
off counts
off
gate
on time
chopper
probe circuit
integrator
probe
1 M
off time
remac
scope
pulse gen
modcomp
terminal
XBL 823-8701

Figure 24

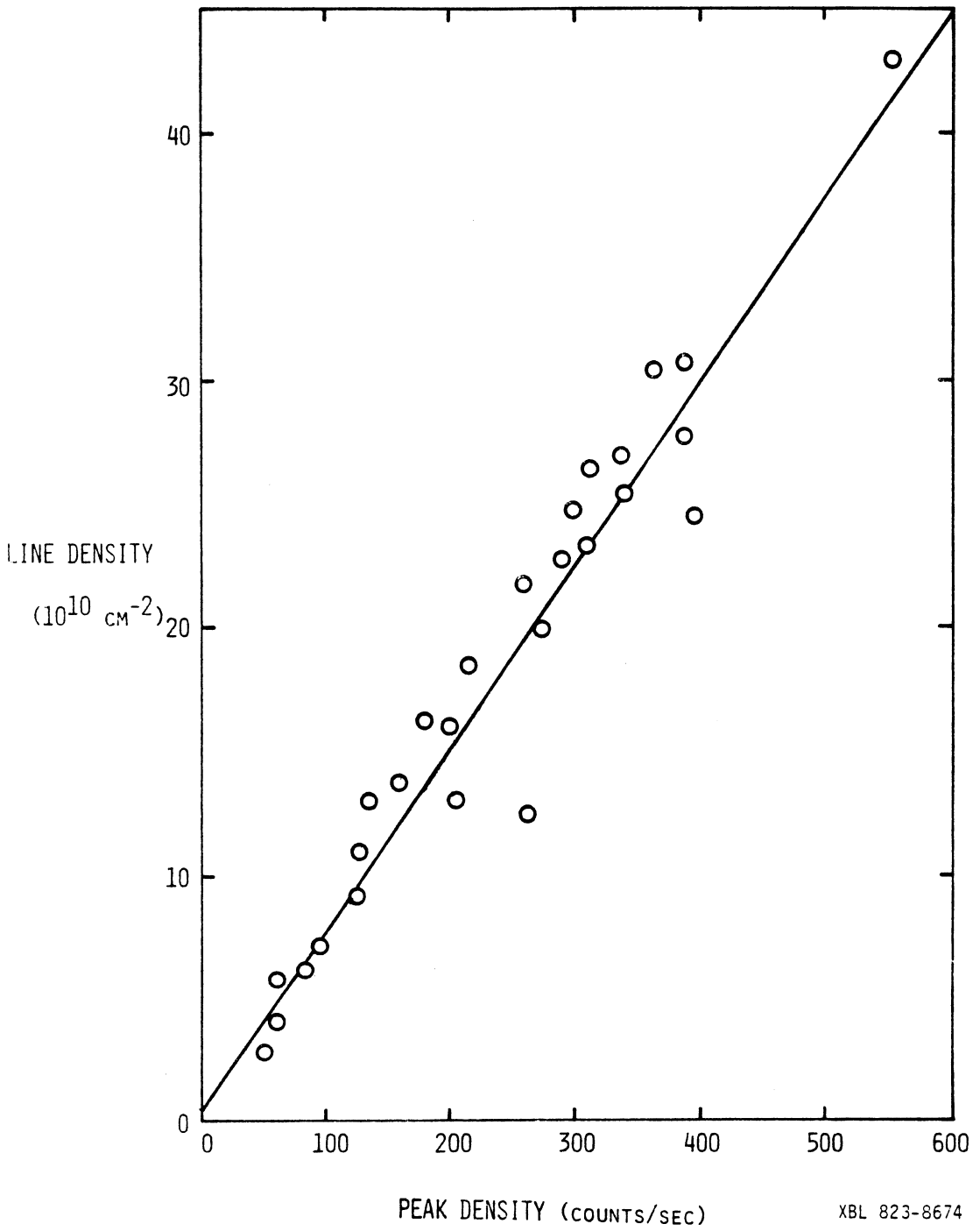

Figure 25. Integrated radial line density versus Langmuir probe counts/ON time. These data span approximately 25 runs over two months operation.

The counting electronics and data acquisition system are shown in Fig. 24.

In addition, it was assumed that the total radial line density also was proportional to the density at one point. This is equivalent to assuming the plasma profile remained unchanged as the peak density was varied. This was confirmed over many runs and the total error from this technique was around 13 percent as deduced from the least-square fit to the data in Fig. 25.

The plasma line density could be varied in several ways. Either the oven temperature could be varied, or the hot plate temperature could be varied by changing the electron bombardment power supply voltage. The plasma density is a strong function of temperature as is indicated by the critical density in Fig. 9.

The second technique was preferred since the time constant for changing density by this method was approximately 15 seconds and much shorter than the time constant for changing the oven temperature (many minutes).

The beam was swept across the plasma to confirm the correct tuning of the beam. Initial runs of the experiment were not done correctly due to the fact that the beam was not centered on both the plasma column and the detector array simultaneously. This usually resulted in cross section measurements which were too low due to either lost beam or lower target thicknesses or both. A typical beam sweep is shown in Fig. 26. The plasma density was held constant for the beam sweeps. Ideally the profile would be flat topped. However, since the plasma profile was not always flat, the

apparent cross section was a convolution of the beam path through the nonuniform target and the detector acceptance. The detector acceptance angle was geometrically determined to be ~ 4.5×10^{-3} steradians. This is smaller by a factor of three than the acceptance angle used by Peart and Dolder but the analyzed-beam energy for this experiment was at least a factor of twenty higher than theirs. This should minimize the effects of angular scattering on the cross section.

After making sure that the beam was tuned correctly, the plasma density was varied and beam data were taken simultaneously.

It thus was possible to vary the plasma line density and to take counter data at the same time. These data were taken by the computer and stored on disk for analysis during and after a particular plasma run. Typically a counter shot lasted for 30 seconds and yielded plasma density, SEC detecter counts (backround and signal), and incident Cs^+ beam current data. The data was analyzed as in the next section and yielded a Cs^{++} fraction, F^{++}, as a function of plasma line density. The slope of this line yielded the cross section, σ_{12}, which is the cross section for formation of Cs^{++} ions by these two reactions:

$$\begin{aligned} Cs^+ + Cs^+ &\rightarrow Cs^{++} + Cs^0 \qquad \sigma_{cx} \\ &\rightarrow Cs^{++} + e + Cs^+ \qquad \sigma_i \end{aligned} \tag{6.1}$$

These data are presented in the next section.

A plasma run typically lasted for two hours, but sometimes as long as eight hours. The cathode operation was extremely good for

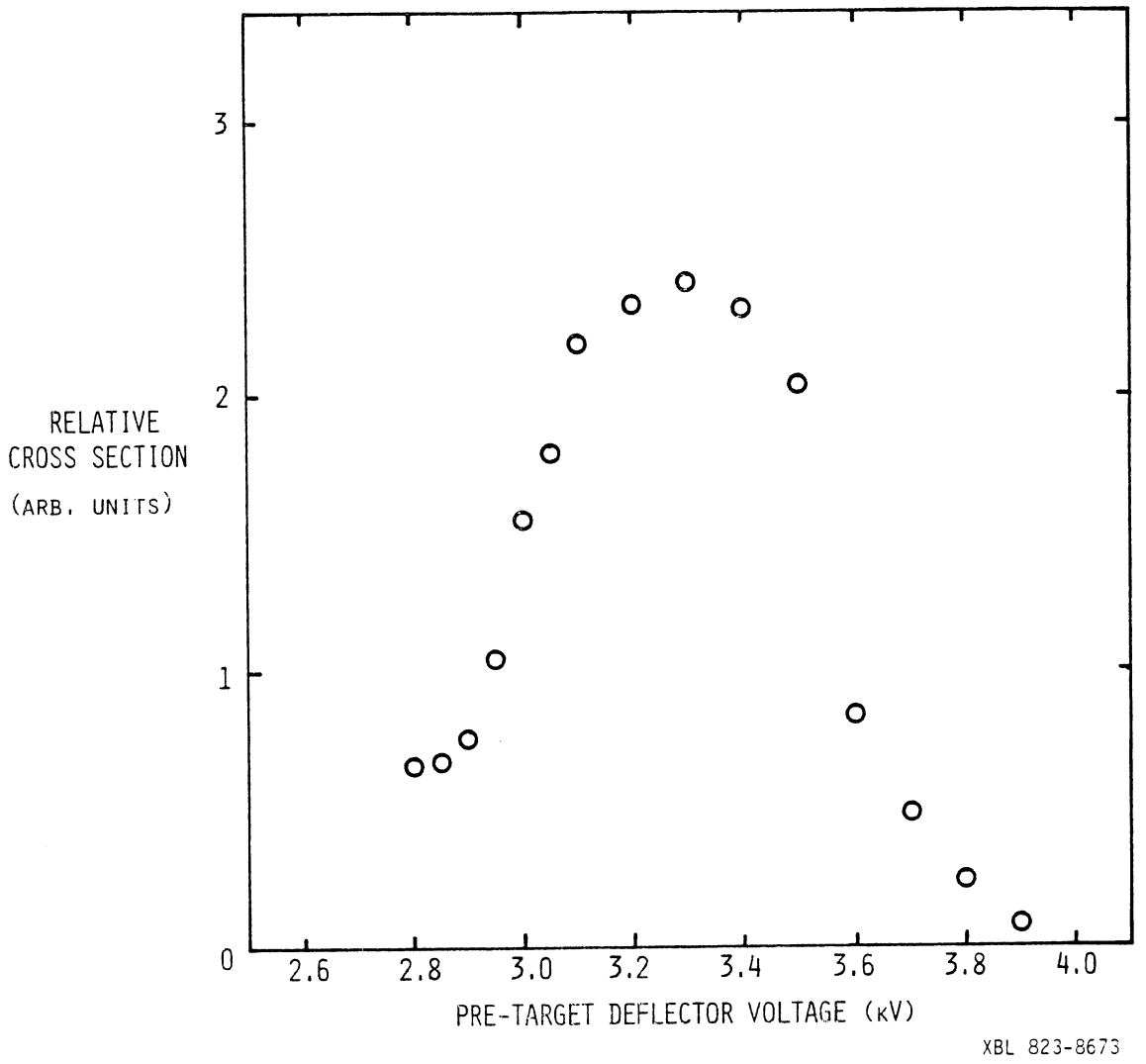

Figure 26. Apparent cross section versus pre-target deflector voltage.

long periods of time and the only limiting factors usually were depletion of cesium, or occasionally insulator failure due to operation at high temperatures for long times.

The longer runs allowed the energy of the Cs^+ beam to be varied such as to obtain cross section data for a range of energies. Typically data at four or five energies could be taken in an eight hour plasma run. Each energy had about 50 data points associated with varying the plasma density.

VI. DATA ANALYSIS

The analysis of these data is fairly straightforward. One can refer to the book by Bevington[34] for the explicit formulas for least square fits and error analysis.

For each plasma run counter data was collected for many intervals lasting for typically 30 seconds. The plasma as discussed before was chopped on and off by a mechanical stop to allow for counting signal plus background and background alone. The quantities measured were:

TOTAL TIME:	Typically 30 seconds.
ON TIME COUNTS:	Time when plasma was on.
OFF TIME COUNTS:	Time when plasma was off.
ON COUNTS:	Secondary emission detector counts when the plasma was on.
OFF COUNTS:	Secondary emission detector counts when the plasma was off.
Cs^+ COUNTS:	Proportional to incident Cs^+ current-measured for TOTAL TIME.
LANGMUIR PROBE COUNTS:	Proportional to plasma density; counted for the ON TIME.

Since the secondary emission detector should obey Poisson statistics, we can define errors in the number of counts as

$$\sigma_{ON} = ON^{1/2},$$
$$\sigma_{OFF} = OFF^{1/2} \tag{6.2}$$

The background signals were subtracted from the signal plus background to give the net F^{++} fraction:

$$F^{++} = \frac{\frac{ON}{ON\ TIME} - \frac{OFF}{OFF\ TIME}}{\frac{Cs^{+}\ COUNTS}{TOTAL\ TIME}} \tag{6.3}$$

The errors were normalized to the count times and added in quadrature and the Cs^{+} count errors were ignored as being small with respect to the statistical errors. That is,

$$\sigma_{F++} = \frac{\left[\left(\frac{\sigma_{ON}}{ON\ TIME}\right)^{2} + \left(\frac{\sigma_{OFF}}{OFF\ TIME}\right)^{2}\right]^{1/2}}{\frac{Cs^{+}\ COUNTS}{TOTAL\ TIME}} \tag{6.4}$$

Thus, for each line density, an F^{++} fraction and σ_{F++} error were computed. These results were plotted as in Fig. 27.

The abcissa shown is proportional to the plasma density. However the plasma line density is the quantity which must be known to compute the cross section. To correlate the two, moving probe (plasma profile) data was compared to the LANGMUIR PROBE COUNTER

data (when the probe was at the peak of the plasma density profile) at the nearest possible time. It thus was possible to convert a static probe counter result into a plasma line density. It was assumed that the plasma line density varied linearly with density measured at one point. As explained in the previous section, this uncertainty was estimated to be 13 percent, independent of the particular run. This uncertainty was added in quadrature with the error in the slope for a given run to give a total cross section error.

The slope of the line fit through these data is proportional to the cross section σ_{12}. We fit a straight line to the data of the form

$$y = a + bx \tag{6.5}$$

where $y = F^{++}$ is the Cs^{++} fraction of the beam and x = LANGMUIR PROBE COUNTS/ON TIME is proportional to the plasma line density.

The least-square fit took into account the uncertainty of each point by weighing each point with σ_{F++}^{-2}. The fitting procedure yielded the y-intercept (a) and the slope (b) and uncertainties for each. The y-intercept, a, was not forced to zero but usually was near zero within the error of the fit.

Also computed were a linear correlation coefficient and a probability for no correlation of the data.

The cross section, σ_{12}, then was computed by

$$\sigma_{12} = \frac{b}{C} \tag{6.6}$$

where C is the conversion factor for LANGMUIR PROBE COUNTS to plasma line density.

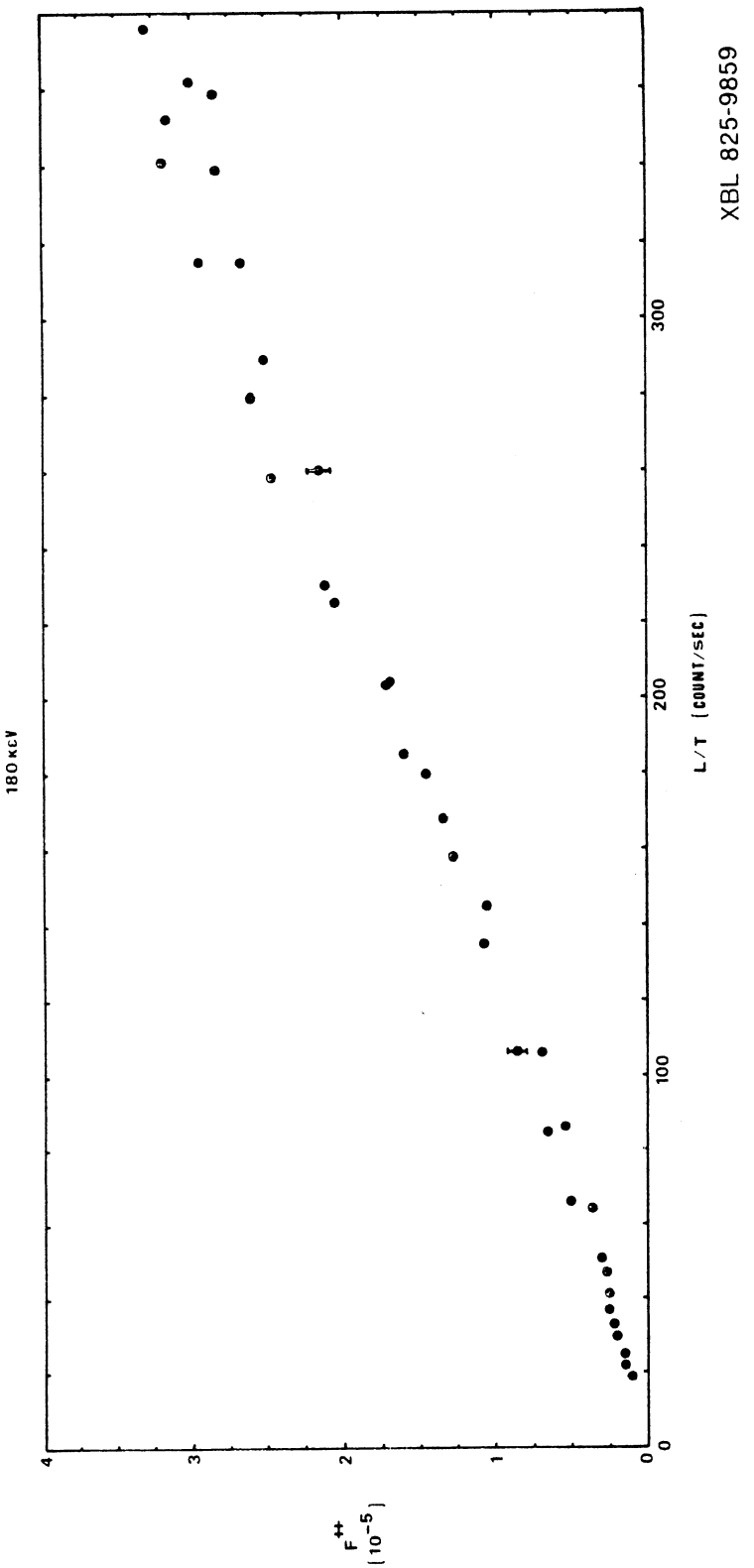

Figure 27. F^{++} fraction as a function of plasma line density for 180 keV Cs^{+} beam. Error bars shown are the typical statistical counting errors due to Poisson statistics.

CHAPTER 7

RESULTS AND DISCUSSION

A. Present Experiment

The final results for this experiment are presented in this chapter. Table 1 shows the results for the individual runs which are believed to be the most accurate. The cross section for electron loss from the incident cesium ion is defined as the sum of ionization and charge transfer cross sections. That is,

$$\sigma_{12} = \sigma_{cx} + \sigma_{ionization} \tag{7.1}$$

This cross section is derived as explained in the previous chapter. The slope of the line F^{++} vs plasma line density is proportional to the loss cross section. A typical plot of F^{++} is shown in Fig. 27. The error bars are errors arising from the counting errors associated with the secondary emission detector. The background also has been subtracted. The error in the slope is added in quadrature with the uncertainty of the plasma line density to yield a total cross section error. These quantities also are tabulated in Table 1. The data for a particular energy is averaged by weighing each point with its total uncertainty to yield the final results for the loss cross section σ_{12}. The results are tabulated in Table 2 and plotted in Fig. 28. The center of mass energy is used since this is the preferred parameter for crossed beam

TABLE I. Results of individual experiments.

(Run #)	Cs^+ Beam Energy (keV)	$\sigma_{12}(10^{-16}cm^2)$	Slope Error (%)	Line Density Error (%)	Total Error (%)
1(33)	100	0.47	20	13	24
2(32)	120	0.70	7	13	15
3(38)	120	0.48	50	13	52
4(32)	140	0.85	14	13	19
5(31)	140	1.09	2	13	13
6(24)	150	1.20	2	13	13
7(16)	150	1.90	5	13	14
8(26)	160	1.43	6	13	14
9(30)	160	1.45	2	13	13
10(33)	160	1.50	20	13	24
11(36)	160	1.26	3	13	13
12(30)	180	1.65	1	13	13
13(43)	180	1.50	1	13	13
14(37)	200	2.04	8	13	15
15(43)	200	1.73	1	13	13
16(28)	220	2.23	1	13	13
17(24)	220	1.67	.5	13	13

experiments. In this experiment, since the target ion is essentially at rest, the center of mass energy is given as

$$E_{cm} = 0.5\ E_{beam} \tag{7.2}$$

The results of the two other crossed beam experiments reported by Dunn, et. al.,[13] and Peart, et. al.[14,15] also are shown in Fig. 28. It is evident that there is a wide discrepancy between the results of these experiments at lower energies. This will be discussed later in this chapter. Unfortunately, the range of energies for the three experiments do not completely overlap. It is evident that the results of the present experiment appear to agree better with the results of Peart, et. al. than with Dunn, et. al.

B. Discussion of results and comparison with other experiments

Since there is such a wide discrepancy between the data of the results of Dunn et. al. and Peart et. al. and the present experiment at low energies, it is worthwhile discussing some of the possible sources of systematic errors which might explain the different results.

The problems with the crossed beam technique have been discussed previously in Chapter 3. These problems are believed to be exacerbated in the case of these heavy ion collisions for the following reasons. First, at the energies of interest, the slower ions have a much more severe space charge problem. This would tend to cause the beams to spread out much more than in the case of

TABLE 2. Summary of results.

c.m. Energy (keV)	σ_{12} (10^{-16} cm^2)	± uncertainty (10^{-16} cm^2)
50	.47	.11
60	.67	.09
70	.95	.09
75	1.38	.14
80	1.37	.10
90	1.57	.14
100	1.82	.17
110	1.87	.18

higher energy ion beams. Also, the interaction region would be much more susceptible to space charge problems as the slow beams intersect. Depending on the geometry of the particular experiment, this may result in a higher or lower apparent cross section since the space charge scattered beam may overlap the charge-changed beam.

Second, the apparently large elastic scattering cross section for the heavy ions may also lead to an erroneous measurement. It was found that in the case of Cs^+ + Xe experiments reported in Appendix C, large scattering resulted in a lower measured cross section in a gas cell type experiment. Since the Cs^+ + Cs^+ system is believed to scatter even more, this may be a source of problems for the crossed beam experiments.

Of course, the plasma target technique also is subject to its own problems and there are several which are in common with the crossed-beam technique. This experiment also had to contend with the large scattering at lower energies. Since a relatively high energy beam (> 100 keV) was analyzed in this experiment, as compared to the rather low energy beam (around 10 keV) analyzed in crossed-beam experiments, it is thought that the problem is less severe for the plasma target technique. This was confirmed when the gas cell was used to simulate the presence of the plasma as described in Appendix C. These experiments were performed at 150 keV and not at lower energies. Thus we are confident that the results of the present experiment are not subject to adverse scattering problems. The slight difference between the present

results and the results from Peart, et. al. below 75 keV might be attributed to these types of effects.

Space charge modulation of the beam in the present experiment is expected to be small due to the fact that the plasma already is neutralized by the electrons. No effects were ever seen on the probe signal when the beam was modulated. This was expected since the density of the ion beam is small in comparison to the plasma density ($n_{beam}/n_{plasma} = 10^{-8}$). Also, background modulation was believed to be small since the mean free path for ionization is long for cesium atoms and other neutral atoms in the plasma.[25] Thus burnout of neutrals in the plasma is negligible.

The major source of systematic errors in the present experiment was in the interpretation of the probe characteristics and in determining the plasma density from them. These problems are discussed in Appendix A. It is believed that the uncertainty in the determination of the plasma density is about 30 percent at a maximum. This is by far the major problem with the plasma target technique for this experiment.

Other problems with the technique involve steering the beam properly through the plasma and onto the detector array. A lot of work was done to insure that the beams did not scrape on exit aperatures and that the beams were centered on the plasma as well as the detectors. This was the primary reason why the initial results from the experiments were erroneous. Later runs were checked to make sure that the beams were aimed correctly.

The comparison of the present results to the results of the crossed-beam experiments should be interpreted in light of these possible systematic errors. While in the present case, all possible systematic errors in steering would tend to lower the measured cross sections, other errors in probe analysis could change the results up or down depending on the particular error made in probe analysis.

After considerable work to minimize the steering problems of the beam, the maximum systematic error associated with this experiment is believed to be less than ± 30 percent.

The absolute uncertainty is larger than for the two crossed beam experiments. Dunn et. al. claim a maximum possible systematic error if ± 8.5 percent. Peart and Dolder claim a maximum possible systematic error of 10 percent. After folding in the systematic errors, the agreement between the three experiments is good except at the lowest energies. The data of Dunn et. al. still is a factor of three higher than the results from Peart and Dolder and the present experiment. Thus there must be some systematic errors among the three experiments.

The following systematic differences between the experiments are noted. The plasma target experiment used high energy beams (> 100 keV) incident on a thermal target. The charge-changed components of the beam were magnetically analyzed and the Cs^{++} component of the beam was detected with a secondary emission detector. The typical signal to background ratio in this experiment was ~ 2.

The experiment of Dunn et.al. detected the charge-changed components of a 14 keV beam intersected at 90 degrees to a beam of variable energy from 66 to 544 keV. The detected beam was electrostatically analyzed in a two-stage electrostatic analyzer. Single particle counting was used to detect the Cs^{++} component of the beam. Typical signal to background ratios were not mentioned.

The experiment of Peart and Dolder detected the charge-changed components of 9.9 and 14 keV beams intersected at 160 degrees to a beam of variable energy from 10 to 80 keV. The Cs^{++} component of the beam was detected by a single particle detector (Johnston, type MM1-1SG) after being electrostatically analyzed. The signal to background ratio for a typical measurement was quoted to be 0.17.

Careful checks on the systematic errors by all three experiments still gave rise to inconsistent results. Possible sources of error which have not been addressed completely in the crossed-beam experiments are: 1) Detector efficiency versus count rate. 2) Space charge modulation of the slow heavy ion beams. While there undoubtly are other sources of possible errors, these seem to be the main candidates.

The final conclusions regarding this experiment and a comparison with theory is made in the next chapter.

Figure 28. Cross section for Cs^{++} formation determined by the plasma target technique as a function of center of mass energy. Open circles: present experiment. Open triangles: Peart et.al. Open squares: Dunn, et.al. Solid triangles: Peart, et.al., σ_{10}.

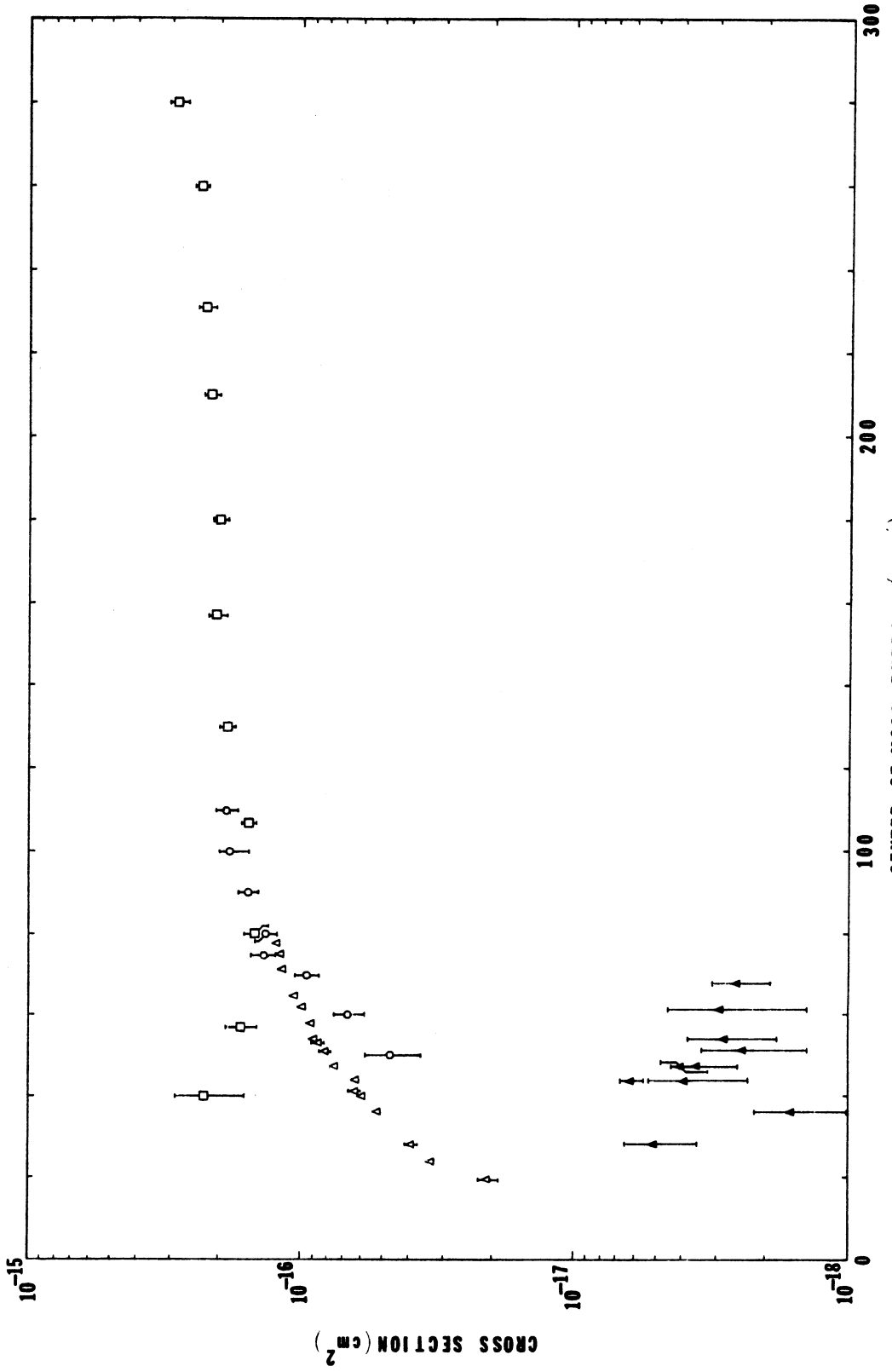

XBL 825-9861

Figure 28

CHAPTER 8

CONCLUSIONS

The experimental data has been discussed in the previous chapter. It remains to draw some final conclusions regarding the importance of the charge-changing cross section on the development of the heavy-ion fusion schemes based on storage ring technonogy. Since Peart and Dolder have shown the relative unimportance of the charge exchange cross section, the dominant loss mechanism is due to ionization. In that case, only one ion is lost in each collision. The results from the present experiment indicate that the loss cross section varies approximately linearly with energy and has the form

$$\sigma_{12}(E) = a + bE \qquad (cm^2) \tag{8.1}$$

where $a = -1 \times 10^{-16}$ cm^2 and $b = 3 \times 10^{-18}$ cm^2/keV. The range of validity of this expression is between 50-100 keV in the center of mass energy. The reaction rate can be computed if the distribution function is known. A reasonable choice for a distribution function would be a uniform distribution between 0 and 100 keV. If the loss cross section is assumed to be negligible at energies below 50 keV, then it is straightforward to show the reaction rate can be written as

$$\langle \sigma v \rangle = \frac{(\Delta v)(\bar{v})}{v_{max}} \sigma(\bar{v}) \tag{8.2}$$

where Δv is the difference in velocities of 50 and 100 keV cesium ions and $\bar{v}$ is the average velocities of these energy ions. v_{max} is the velocity of a 100 keV cesium ion. This calculation gives a reaction rate of 10^{-9} cm^3 sec. Thus, if the beam density is 3 x 10^8 cm^{-3}, the beam time constant is ~ 3.3 sec. To avoid appreciable beam loss, it would be advisable to limit the storage time to ~ 30 msec.

It has been suggested that storage times of 10^{-2} τ might still be too long to contain a heavy ion beam. Jones[35] has postulated that sputtered material from the walls might catastrophically disrupt the beam in very short times. If slow atoms from the wall travel at ~ 10^5 cm/sec, and the distance to the beam is ~ 10 cm, then the ablated material would interact with the beam in ~ 100 μ sec. This is substantially shorter than the beam constant.

Thus, a critical problem for future study related to storage rings for intense ion beams would be the sputtering effects of high energy beams on wall material. It should be noted that induction linacs would be immume to this problem because the beam envelope would travel many meters past any point along the beamline before the ablated wall material could reach the beam radius.

Other results of the experiments performed as part of this thesis concerned charge transfer and ionization in collisions of Cs^+ + Xe. The results are discussed in Appendix C. The hypothesis regarding the similarity of the Cs^+-Xe system to the Cs^+ - Cs^+ system was shown to only hold up for charge-changing cross sections for the Cs^+ projectile. The ionization cross

section of Xe was substantially higher than the ionization cross section of the projectile. This seems physically reasonable on the basis of the difference in ionization potentials of Cs^+ (25.1 eV) versus Xe (12.127 eV). The cross section for ionization of Xe was about 2×10^{-15} cm^2 at beam energies around 100 keV. This is substantially higher than the charge transfer cross section and the projectile ionization cross section which were both about 1×10^{-16} cm^2 at 100 keV Cs^+ energy.

The use of the Q machine plasma target to study D^- detachment was not useful in the present geometry. The attainable plasma line densities for perpendicular injection were not sufficient to study the optimum yield of neutral deuterium. Also, the study of cross sections which could be used to infer the optimum neutral yield was not performed due to the difficulty in detecting the widely divergent beam in the plasma confinement magnetic field.

Overall, the Q machine plasma target was a useful method for determining ion-ion collision cross sections for cesium ions. It remains to be seen if the target can be improved to study other ion-ion systems relevant to both heavy-ion fusion and magnetic confinement fusion.

REFERENCES

1. Fusion, Vol. 1. ed. by E. Teller, Academic Press, 1981.
2. Simonen, T. C., Proc. of the IEEE, 69, 935 (1981).
3. Keefe, D., Inertial Confinement Fusion. To be published as an article in Annual Review of Nuclear Particle Science, 32, Annual Review Inc. (1982). Also LBL Report No. 14194.
4. Yonas, G., Scientific American, 239, 50 (1978).
5. ERDA Summer Study of Heavy Ions for Inertial Fusion, LBL-5543, Claremont Hotel, Oakland/Berkeley, July 19-30, 1976.
6. Proceedings of the Heavy Ion Fusion Workshop, BNL 50769, Brookhaven National Laboratory, Upton, NY, October 17-21, 1977.
7. Proceedings of the Heavy Ion Fusion Workshop, ANL-79-41, Argonne National Laboratory, September 19-26, 1978.
8. Proceeding of the Heavy Ion Fusion Workshop, Berkeley, (1979). LBL-10301.
9. Avery, R., Behrsing, G., Chupp, W. W., Faltens, A., Hartwig, E. C., Hernandez, H. P., MacDonald, C., Meneghetti, J. R., Nemetz, R. G., Popenuck, W., Salsig, W. and Vanecek, D., IEEE Trans. Nuc. Sci., NS-18, 479 (1971).
10. Heavy Ion Fusion Staff, U.C. LBL Pub 5039 (1980).
11. Introduction to Physical Gas Dynamics, by Vincenti, W. G., and Kruger, C. H., Wiley (1965) p. 52.
12. Hiskes, J. R., UCID-17231.
13. Dunn, K. F., Angel, G. C. and Gilbody, H. B., J. Phys. B, 14, L623 (1979).

14. Peart, B., Forrest, R. A., and Dolder, K., J. Phys. B, 14, 1383 (1981).

15. Peart, B., Forrest, R. A. and Dolder, K., J. Phys. B, 14, 1655, (1981).

16. Olson, R. E., and Liu, B., J. Phys. B, 14, L279 (1981).

17. Fano, U. and Lichten, W., Phys. Rev. Lett., 14, 627 (1965).

18. Brenot, J. C., Dhunicq, D., Gauyacq, J. P., Dommier, J., Sidis, V., Barat, M., Pollack, E., Phys. Rev. A, 11, 1245 (1975).

19. Read, F. H. in Proceedings of IX Intl. Conf. on the Phys. of Elect. and Atomic Collisions. Invited paper p. 176, Seattle, (1975).

20. Dolder, K. T., in Electronic and Atomic Collisions, Invited papers ed. by G. Watel (North Hollamd, Amsterdam, 1978), pp 281-294.

21. Dolder, K. T. and Peart, B., Rep. Prog. Phys., 39, 693 (1976).

22. H. B. Gilbody, "Collisions Between Positive Ions," Proceedings of the 12th International Conf. on the Physics of Electronic and Atomic Collisions (ICPEAC) Gatlinburg, USA (1981).

23. Physics of Atomic Collisions, 2nd Ed., by J. B. Hasted, American Elsevier (New York) 1972 p. 723.

24. Langmuir, I. and Kingdon, K. H., Proc. Roy. Soc. Ser. A, 107 61 (1925).

25. Q Machines, Motley, R. W., Academic Press (1975).

26. Rynn, N., Rev. Sci. Instr., 35, 40 (1964).

27. Rynn, N., and D'Angelo, N., Rev. Sci. Instr.,-31 (1960).

28. Hashmi, M., Van der Houven Van Oordt, A. J., and Wegrowe, J.-G., Nucl. Fusion, 10, 163 (1970).

29. Spitzer, L. Jr., Physics of Fully Ionized Gases, Interscience, New York, 1962. p. 139.

30. Selected Values of the Thermodynamic Properties of the Elements, Hultgren, R., Desai, P., Hawkins, D., Gleiser, M., Kelley, K., Wagman, D., Editors. Am. Soc. Metals. (1973).

31. Nishikawa, K., Wakatani, M. Tuda, T., Tange, T. and Hatori, T., IPP-Rev-1 (1981).

32. Spectra-Mat, Inc., Standard 250 Ion Source.

33. Lambert, M., Thomas, J. P. and Buchet, J. P. in Low Energy Ion Beams, 1977, ed. by Stephens, K. G., Wilson, I. H. and Moruzzi, J. L. The Institute of Physics, Bristol, (1978). pp. 103-108.

34. Data Reduction and Error Analysis for the Physical Sciences, P. R. Berington, McGraw-Hill, 1969.

35. Jones, L. W. in Proceedings of the Heavy Ion Workshop, LBL-10301, Claremont Hotel, Berkeley, Oct. 29- Nov. 9, 1979 pp. 294-296.

36. Langmuir, I. and Mott-Smith, H. Phys. Rev., 28, 727 (1926).

37. Langmuir, I. Phys. Rev., 33, 954 (1929).

38. Chen, F. F., in Plasma Diagnostic Techniques, Chapter 4, ed. by Huddlestone, R. H. and Leonard, S. L., Academic Press, New York, 1965.

39. Laframboise, J. G., Univ. of Toronto, IAS, Report No. 100, (1966).

40. Laframboise, J. G. and Rubenstein, J. Phys. Fluids 19 1900, (1976).

41. Electric Probes in Stationary and Flowing Plasmas: Theory and Application, Chung, P.M., Talbot, L., Touryan, K.J., Springer Verlag, (1975).

42. Peterson, E. W. and Talbot, L., AIAA Journal, 8, 2215 (1979).

43. Chen, F. F. Etievant, C. and Mosher, D., Phys. Fluids 11, 811 (1968).

44. Hashimi, M., Van der Houren Van Oordt, A. J. and Wegrove, J. G., Nuc. Fusion, 8, 197 (1968).

45. Ruggieri, D. J., IEEE Trans. on Nuc. Science, NS-19, (1972).

46. Wiza, J. L., Nuc. Inst. and Methods 162, 587 (1979).

47. Fricke, J., Muller, A. and Salzborn, E., Nuc. Inst. Meth., 175, 379 (1980).

48. Rinn, K., Muller, A., Eichenauer, H. and Salzborn, E., to be published in Rev. Sci. Instrum.

49. Paul, A. C., EBQ Code, Transport of Space Charge Beams in Axially Symmetric Devices, UCID-8005 (1978).

50. Berkner, K. H., Graham, W. G., Pyle, R. V., Schlachter, A. S., Stearns, J. W. and Olson, R. E., J. Phys. B., 11, 875 (1978).

51. Tanis, J. A., Stalder, K. R., Stearns, J. W. and Schlachter, A. S., Bull, Am. Phys. Soc., 24, 1196 (1979).

52. Flaks, I. P., Kikiani, B. I. and Ogurtsov, G. N., Sov. Phys. Tech. Phys., 10, 1590 (1966).

53. Ogurtsov, G. N., Kikiani, B. I., and Flaks, I. P., Sov. Phys. Tech. Phys., 11, 362 (1966).

54. Berkner, K. H., Myers, B. R., and Pyle, R. V., Rev. Sci. Instrum. 39, 1204 (1968).

55. Morgan, T. J., Berkner, K. H., Graham, W. G., Pyle, R. V. and Stearns, J. W., Phys. Rev. A, 14, 664 (1976).

56. Laul, V., Rynn, N. and Bohmer, H., An Improved Method for Heating Large Tungsten Cathodes, Univ. of Calif., Irvine, Technical Report No. 77-29.

57. Pyle, R. V., in Second Intl. Symp. on the Prod. and Neutralization of Negative ions and Beams, Upton, N.Y., Oct. 6-10, 1980.

58. Proceedings of the Symposium on the Production and Neutralization of Negative Hydrogen Ions and Beams, Brookhaven National Laboratory, Sept. 26-30, 1977. BNL Report 50727.

59. Proceedings of the Symposium on the Production and Neutralization of Negative Hydrogen Ions and Beams, Brookhaven National Laboratory, Oct. 6-10, 1980. BNL Report.

60. Riviere, A. C. and Sweetman, D. R., Bull of the APS, Series II, 15, 1440 (1970).

61. Dimov, G. I., Ivanov, A. A. and Roslyakov, G. V., Sov. Phys. Tech. Phys., 22, 1091 (1977).

62. Savas, S. E., LBL Report 12771, (1980).

APPENDIX A

Langmuir Probes

Langmuir probes were used in the experiment to measure the plasma density. The theory of Langmuir probes is extensive and well known today. The simplest cases of these theories concern cold ($T_{ion} = 0$), unmagnetized plasmas with Maxwellian distribution functions for electrons. Unfortunately there are few cases in nature where all of these conditions are met. However the Langmuir probe is still one of the mose useful tools in plasma physics. One has to be careful of the interpretation of the results from Langmuir probes for the very reasons cited above. In addition to the interpretation problems of probe characteristics, many practical limitations can limit the usefulness of Langmuir probes. These include contamination, perturbation of the plasma due to the presence of the probe, and collisional effects, etc.

The probes used in this experiment consisted of tungsten wire (.015" diameter) mounted in a uranium glass probe shield. The tip of the probe usually was about 0.3 cm long. The probe design is shown in Fig. 29. The probe tip extended out of the glass sleeve. This sleeve acted to prevent condensed cesium from connecting the probe tip to the outer part of the glass, thereby preventing an apparent rise in the probe current due to increased probe area. The entire probe was mounted on the Q Machine through a Wilson seal and was movable by a motor driven assembly. The probe position was

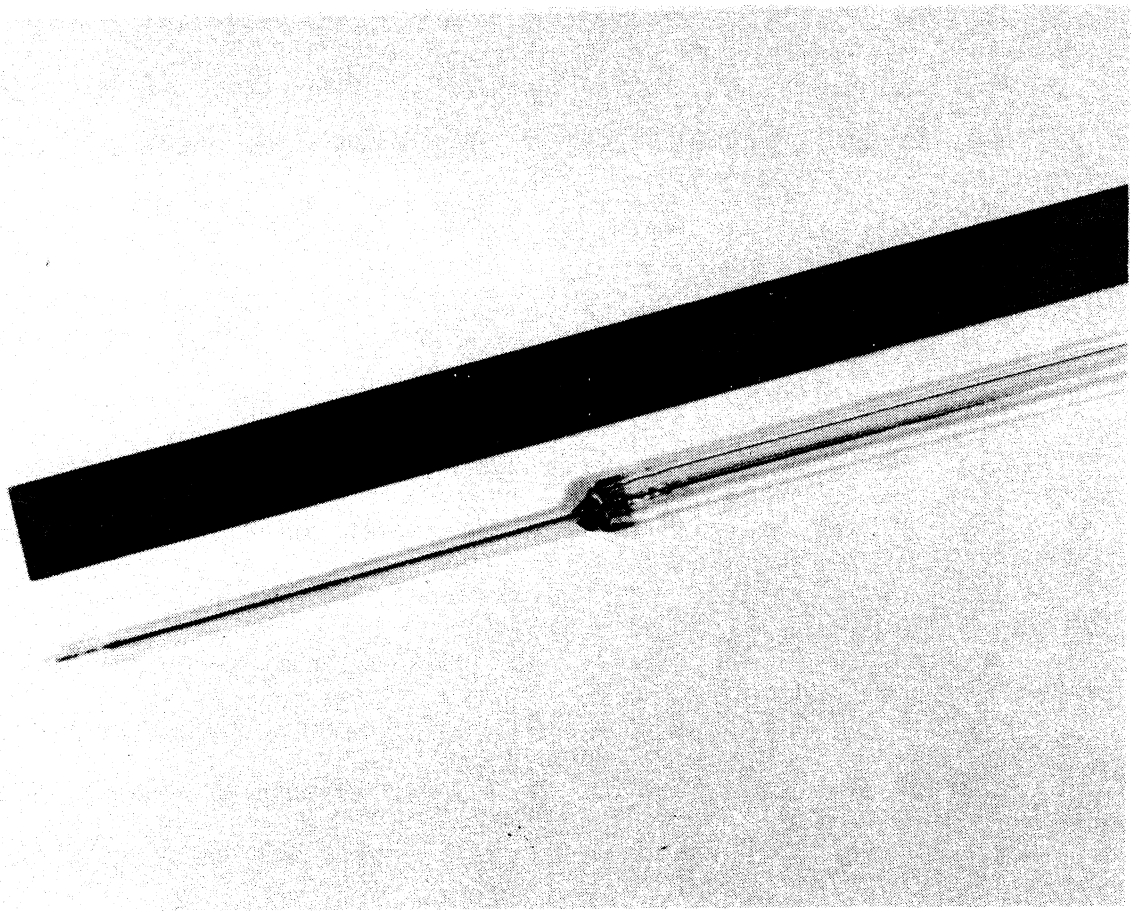

CBB 821-17

Figure 29. Langmuir probe. The glass sleeve was intended to prevent condensed cesium from altering the apparent probe size.

monitored by a potentiometer mounted on the probe mover. Digital readout of the probe position enabled the probe to be set to any position across the diameter of the plasma. Only radial probe data was taken. Recombination of the plasma was negligible and the radial diffusion of the plasma did not alter the total radial line density of the target plasma.

The probe was connected to a driver circuit which allowed the probe potential to be set by several means. The circuit is shown in Fig. 30. The voltage drop across the precision resistor R_1 in Fig. 30 was measured by a differential amplifier with a gain of 100. This voltage was proportional to the probe current. The driver part of the circuit was isolated from the probe part of the circuit by high impedance voltage followers. The probe voltage and current were then read out to an oscilliscope or analog to digital converters (ADC) for data analysis. Data was taken with the probe stationary by sweeping the probe voltage thereby yielding a characteristic current-voltage curve, or the probe potential was fixed and the probe was moved radially across the plasma.

The interpretation of Langmuir probe data has long been a subject of debate among plasma physicists. The earliest uses were due to Langmuir[36,37] [hence the name for the technique] and his pioneering efforts on the effects of the plasma sheath on electron and ion collection to a probe enabled useful parameters such as plasma density and temperature to be measured. Subsequent theories were basically refinements of the work by Langmuir and were summarized in the review by Chen.[38] These theories usually

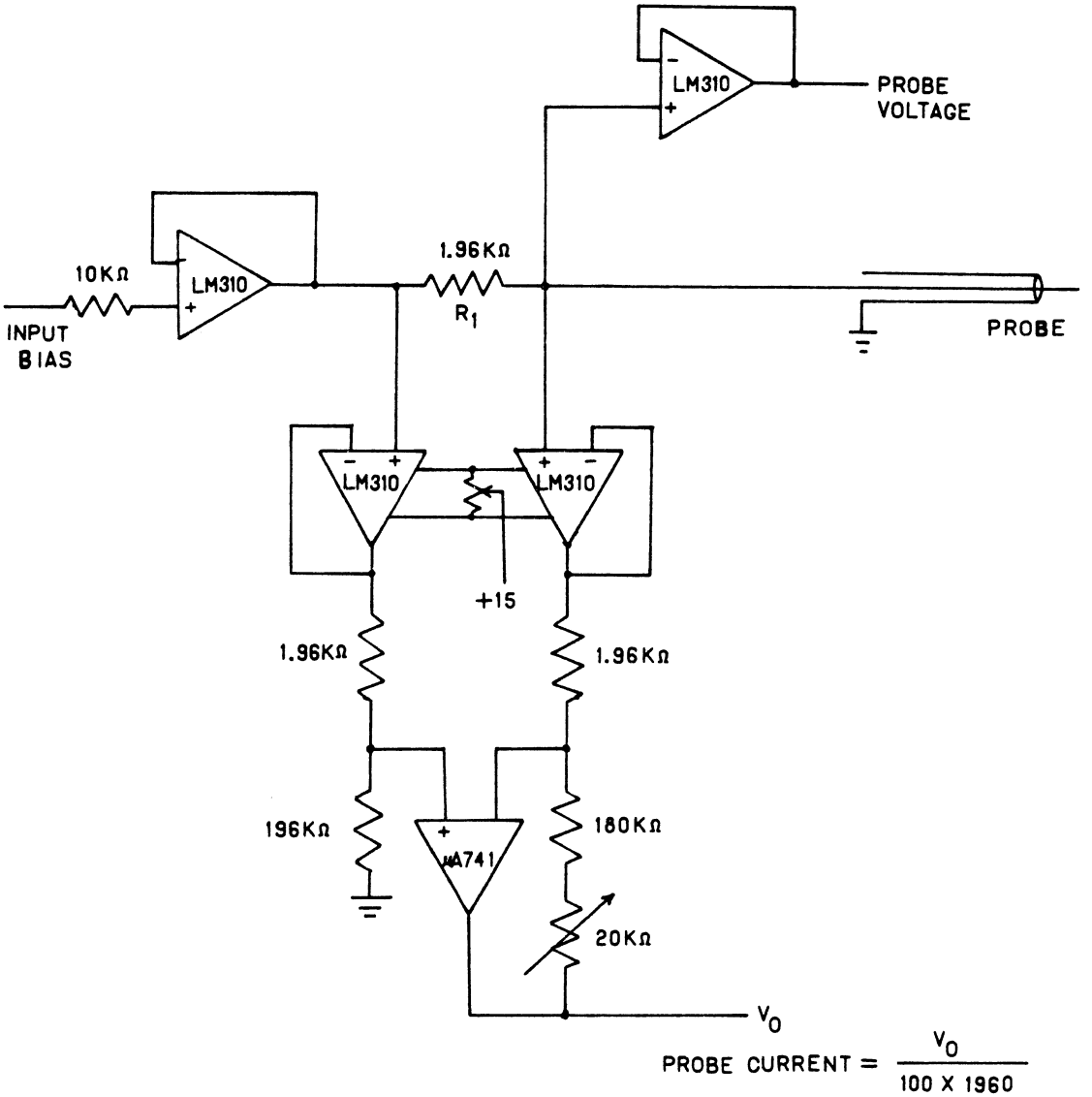

PROBE CIRCUIT

XBL 825-9869

Figure 30. Langmuir probe circuit design. Probe current was measured by the voltage drop across the precision resistor R_1. Probe bias was set by the computer DAC or the signal generator.

referred to different operating regimes of the Langmuir probes. The effects considered were collisions and magnetic field effects. The parameters that describe these effects are r_p/λ and r_p/r_L, respectively, where r_p/λ is the ratio of the probe radius to collision mean free path and r_p/r_L is the ratio of probe radius to gyroradius of a particular plasma species. Space does not allow us to present all of the different results for each set of conditions. We concern ourselves in the following with results applicable to the plasmas typically found in Q machines.

First we ask what are the typical parameters of interest for Q machine plasmas. The probes used in this thesis usually were .038 cm diameter. The magnetic field strength was typically 2 kG. Thus, using the formula

$$r_s = \frac{m_s v_s}{qB} , \qquad (A.1)$$

we have (for $E_{Cs+} = .25$ eV)

$$r_e = 8.4 \times 10^{-4} \text{ cm} \qquad (A.2a)$$

and

$$r_{Cs+} = 4.2 \times 10^{-1} \text{ cm} \qquad (A.2b)$$

Thus, for the conditions relevant to this experiment, $r_p/r_e \gg 1$ and $r_p/r_{Cs+} \ll 1$. That is, electrons are strongly affected by the magnetic field while the ions essentially act as though there were no magnetic field effects.

The Debye length is another critical parameter describing Langmuir probe operating regimes. With the Debye length defined as,

$$\lambda_D^2 = \frac{kT_e}{4\pi n_e} \qquad (A.3)$$

we have (for $kT_e = .25$ eV, $n_e = 10^{10}$ cm^{-3})

$$\lambda_D = 3.70 \times 10^{-3} \text{ cm} \qquad (A.4)$$

Thus, $r_p/\lambda_D \gg 1$. That is, the sheath surrounding the probe is small compared to probe radius. This can significantly simplify the analysis of probe characteristics.

The final parameters describing the operating regime of the probes used in this experiment are the collisional mean free paths. Usually the shortest mean free paths determine whether collisional effects need to be included. For cesium plasmas the electron-ion mean free path is

$$\lambda = \frac{1}{n\sigma_{ei}} \qquad (A.5)$$

Here, $\sigma = 7.7 \times 10^{-12}$ cm^2 at mean energies of 0.22 eV. If $n = 10^{11}$ cm^{-3} then

$$\lambda = 1.3 \text{ cm} \qquad (A.6)$$

Thus, $r_p/\lambda \ll 1$. Collisional effects are negligible for probes operating in Q machines. All other mean free paths are also large.

Thus it is concluded that the probe regime of interest can be described, for ion collection, as a collisionless, unmagnetized, thin sheath case. This regime has been studied extensively and usually the definitive work of Laframboise[39,40] is used to analyze the probe results in this regime. Laframboise' results are also used in this thesis. His results are presented as graphs on the useful correction factors as functions of the various probe parameters. It is useful to have results for all probe conditions, and thus interpolation formulas have been developed to handle the cases not explicitly covered by Laframboise. One of the analytic fitting formulas to the Laframboise results have been developed by Peterson and Talbot.[41,42] Briefly, the ion collection current density to a probe can be expressed as

$$j_i = ne\sqrt{\frac{kT_e}{2\pi m_i}}\, j_i^* \qquad (A.7)$$

where j_i^* is a Laframboise fit parameter defined as

$$j_i = (\beta + |\chi_p|)^{\alpha} \qquad (A.8)$$

and $\chi_p = \dfrac{e(V_{probe} - V_{plasma})}{kT_e}$. α and β have been determined to have the following form:

$$\alpha = \frac{a}{\ln \xi_p + b} + c\,\varepsilon^m + d \qquad (A.9)$$

and

$$\beta = e + \varepsilon\left\{f + g(\ln \xi_p)^3 - \frac{l}{\xi_p}\right\} + \frac{l}{\ln \xi_p} \qquad (A.10)$$

where the constants a, b, c, d, e, f, g, l, m are given by Peterson and Talbot. The following definitions have been used in the above formulas.

$$\xi_p = \frac{r_p}{\lambda_D} \qquad (A.11)$$

$$\varepsilon = \frac{T_i}{T_e} \qquad (A.12)$$

Thus once the electron and ion temperatures are known, and the Debye length is known, α, and β and hence j_i^* and j_i can be determined. Some iteration is necessary because initially T_e and n_e and hence ξ_p is now known precisely.

In practice the interpretation of the probe characteristics is done as follows. For a given probe position, the probe bias is swept from -10 to +10 volts. The current is measured by the probe circuit shown in Fig. 30. The current-voltage characteristic is stored in the computer for further analysis. See Fig. 31. The flat electron region at positive probe bias is due to amplifier saturation and is not due to an actual electron saturation.

To obtain the electron temperature, the ion current to the probe is subtracted from the total probe current. The floating potential

is defined as the potential where no net current flows to the probe. This is determined by interpolating between the voltages where the current crosses zero. The ion saturation region is arbitrarily chosen to be two volts less than the floating potential. A linear least-squares fit to the data below this cutoff is computed and the result gives a line which approximates the ion current to the probe for values up to the plasma potential. The extrapolated ion current then is subtracted from the total current which yields the electron current to the probe.

Since it is expected that the electrons obey a Boltzmann relation in the transition region, the logarithim of the electron current is plotted versus the bias voltage. (Actually the absolute value of the electron current is plotted since noise fluctuations sometimes yield negative electron currents when the extrapolated ion current is subtracted from the total current). This is shown in Fig. 32. It is evident that the electron current is exponential over about two orders of magnitude. A least squares fit to the data in this region yields the electron temperature and the result is displayed on the plot.

Once T_e is known, the plasma potential is computed from the well known result,

$$V_{plasma} = V_{floating} + \frac{kT_e}{2} \ln\left(\frac{m_i}{m_e}\right) \quad (A.13)$$

A crude estimate of the plasma density then is determined by the value of the extrapolated ion current at V_{plasma}. This procedure

yields densities which are accurate to within a factor of 5. Obviously a more careful analysis has to be done to know the density more accurately.

Since the electron temperature is known, an initial guess for the plasma density yields a value of ξ_p. All parameters for the Peterson-Talbot fitting formula then are known. Thus for a given probe bias, the Laframboise factor can be computed. This factor is used to compute the density when the probe bias is fixed at -10 volts and the probe is swept across the plasma column.

There have been several experiments designed to test the accuracy of the Laframboise analysis. Among these relevant to the Q machine plasmas were the experiments done by Chen, et. al.,[43] and Hashmi, et. al.[44] Chen, et. al. compared the results of their probe analysis done by the Laframboise method to the results of other independent methods. These included microwave interferometry and resonant cavity techniques. The final conclusions were that the Laframboise analysis was accurate to within 30 percent of the true plasma density. Hashmi et. al. compared the standard probe analysis technique of equating the ion saturation current at plasma potential to the random ion current in order to determine the plasma density. They concluded that the density determined by this method was accurate to within a factor of 2.5 to the density determined by laser flourescence scattering from barium plasmas. Since they did not mention the Laframboise analysis in their paper, the results subsequently can be interpreted in that light. Applying the Laframboise analysis to the given conditions mentioned by Hashmi,

et.al. the results give a correction factor of ~ 2.0. Thus it seems reasonable that the results from this experiment also tend to confirm the Laframboise analysis to approximately 25 percent. This is probably the best that can be done for the systematic errors in using probes to measure plasma density.

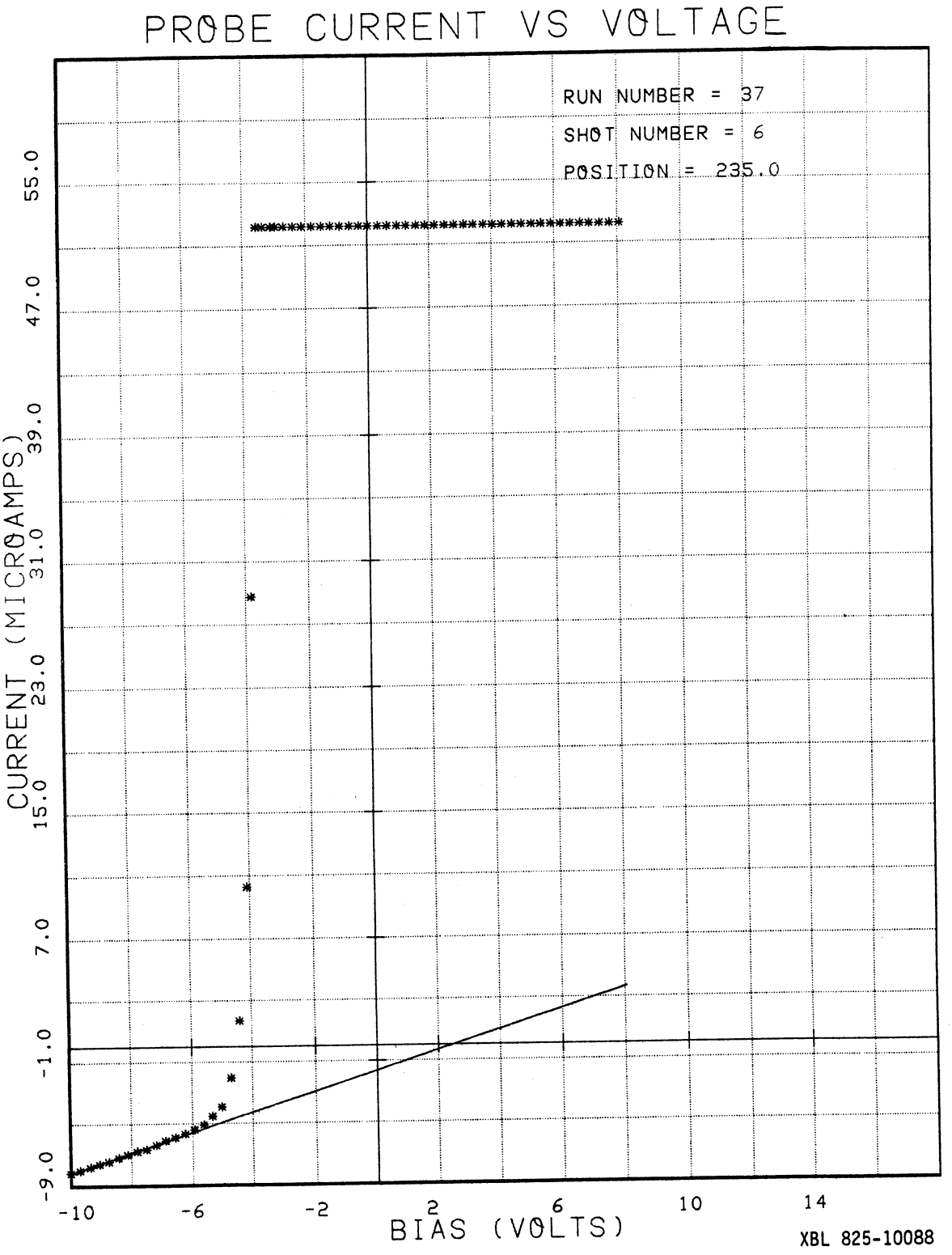

Figure 31. Probe current vs probe bias.

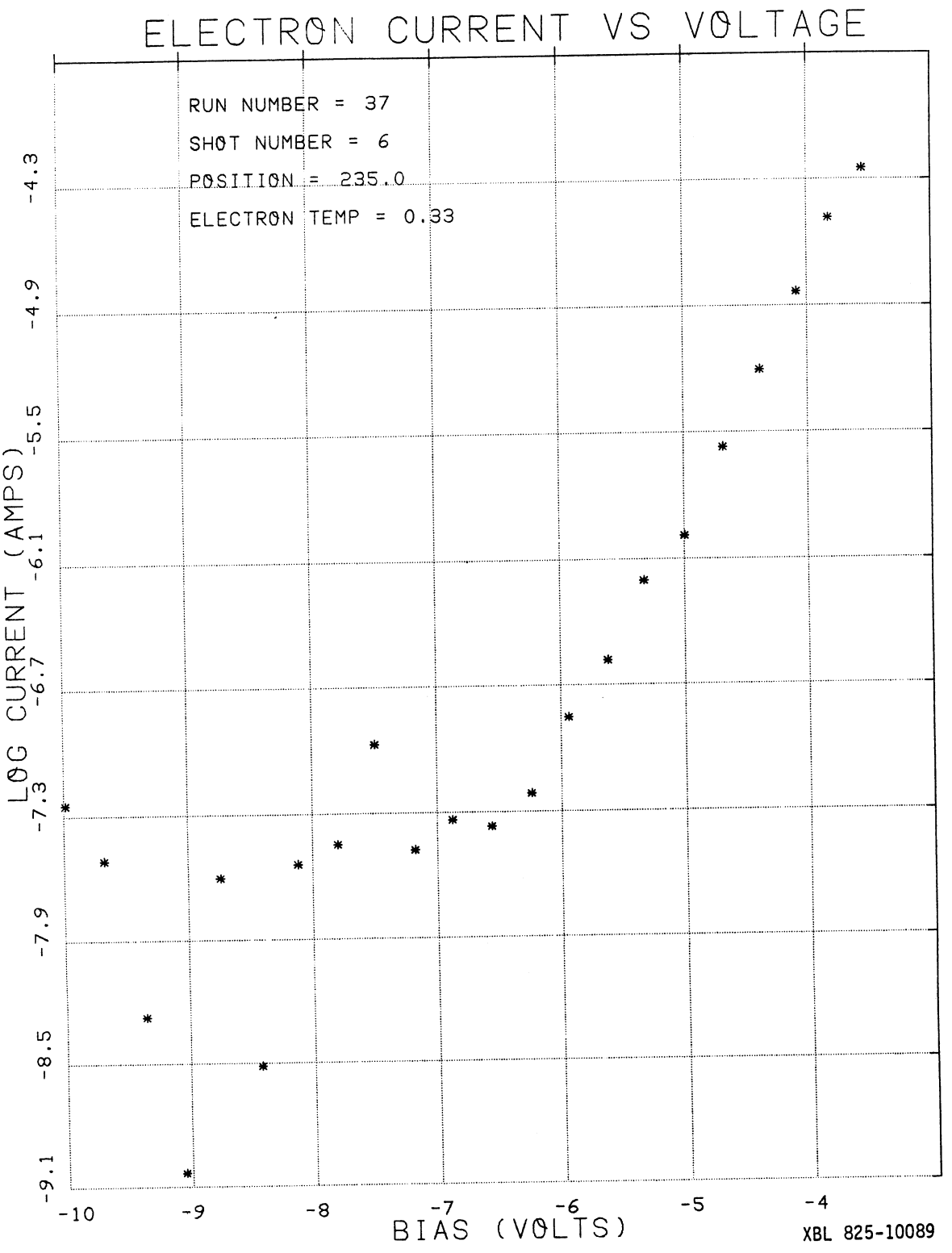

Figure 32. Electron current vs probe bias.

APPENDIX B

Secondary Emission Detector

The secondary emission detector was used in the experiment to detect the Cs^{++} component of the exiting beam. It was found that Faraday cups were not useful for Cs^{++} detection due to the small target thickness attainable with the plasma target. A Faraday cup with electrometer can measure currents down to about 10^{-14} amps. However they have long time constants and it was decided that a single particle detection was the best method for detecting Cs^{++}. Solid state detectors are not useful for detecting heavy ions with energies in the hundred kilovolt range due to their extremely small penetration into the detector. A detector capable of detecting the secondary electrons from ion bombardment of a dirty surface was desirable for several reasons.

First, an electron multiplier, with a gain on the order of 10^6, in conjuction with the initial secondary electrons emitted from the surface would give signals large enough to detect with standard particle counting techniques. Secondly, direct detection of the ions was not desirable due to the spatial gain non-uniformity, unknown active area and unknown long term contamination and damage problems with fast cesium ions. In addition, background signals due to plasma radiation and hot-plate radiation could be minimized by arranging the electron multiplier to "see" only the secondary electron emitting surface and not the plasma directly.

Secondary emission detectors based on electron multiplier technology have been reported in the literature before.[45,46,47] Most utilize single channel electron multipliers. Microchannel plates (MCP) were chosen as the electron multiplier for this experiment for several reasons. Among these are; large size (diameter = 2.5 cm), insensitivity to magnetic fields, relatively large electron detection efficiency (approximately 60 percent), high gains up to count rates of at least 2×10^4 pulses/sec, and low sensitivity to background light from the plasma target chamber.

The entire detector used was based on a design by Rinn[48] except that we replaced the single channel electron multiplier with two microchannel plates (Varian model VUW-89 16ES) in a chevron configuration. The detector array is shown in Fig. 33. The outer can was grounded and typical voltages of the secondary electron emitting surface, MCP input electrode, MCP output electrode and anode are as shown in Fig. 33.

Numerical simulation of the electron trajectories was performed to show that for reasonable starting secondary electron positions, energies and angles, the electrons would strike the active surface of the MCP. Potential maps and typical electron trajectories were computed with the aid of the code "EBQ"[49] and the results are shown in Figs. 34. We then were confident that all emitted secondary electrons would strike the chevron MCP.

Since the detection efficiency of the MCP is approximately 60 percent for single electrons, a secondary electron emission coefficient substantially larger than one is required for

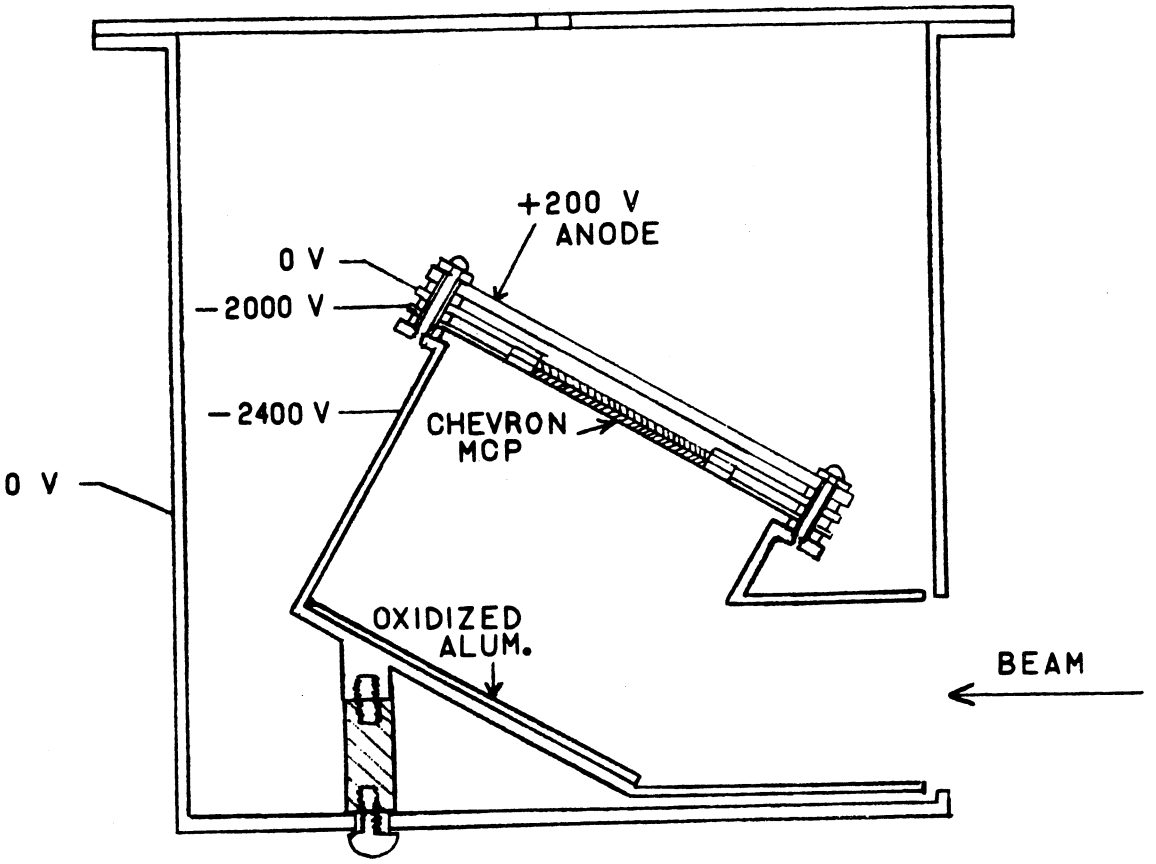

SECONDARY EMISSION DETECTOR

XBL 825-9868

Figure 33. Secondary emission detector (SED) used to detect Cs^{++}. Secondary electrons knocked off the converter surface were accelerated and focused to hit the microchannel plate electron multiplier.

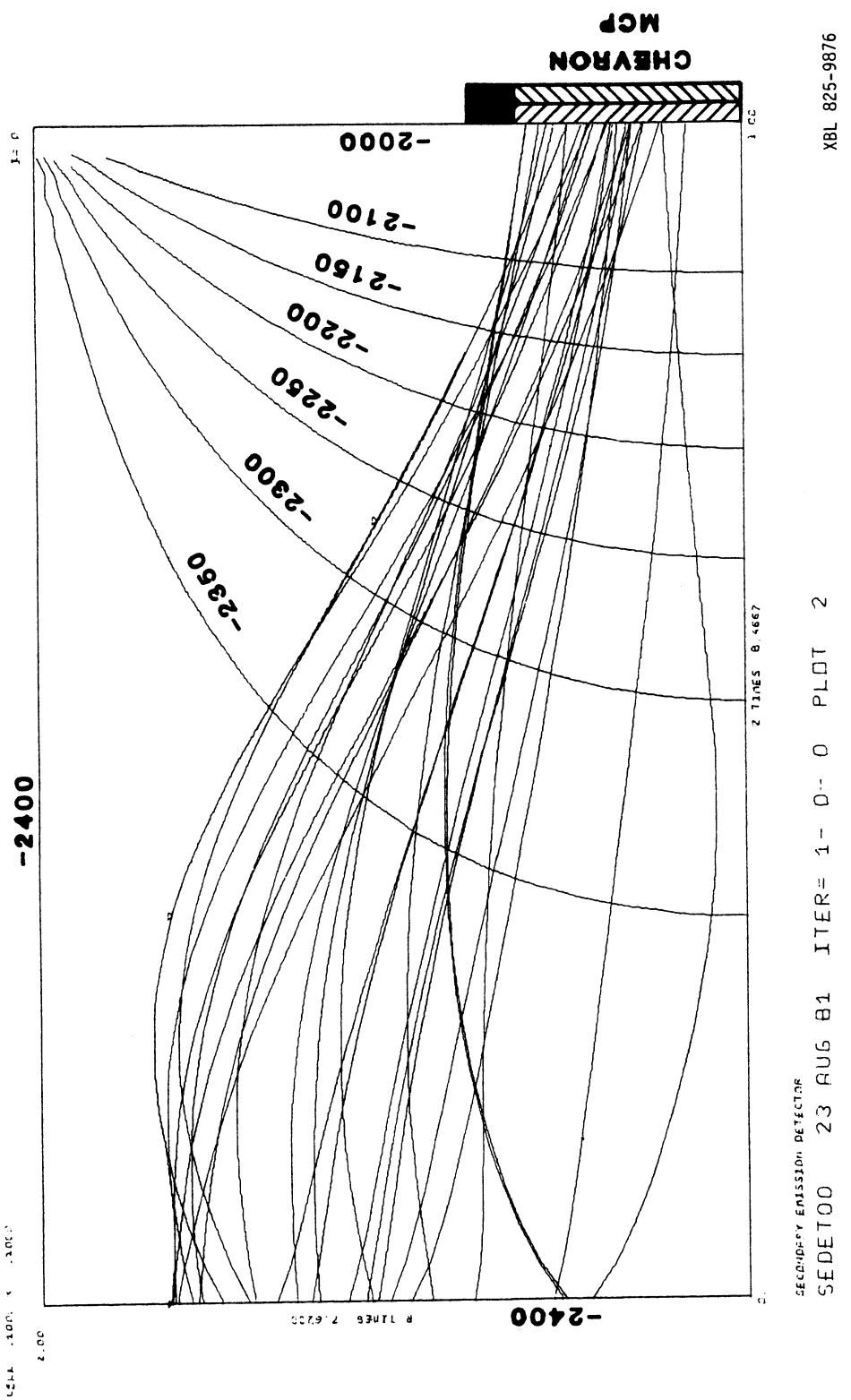

Figure 34. Potential map and electron trajectories for the SED.

100 percent overall detection efficiency of the detector. This can be seen theoretically from the following argument. Assuming uniform gain over the face of the MCP and assuming that δ electrons are emitted for each incident ion, the overall detector efficiency is given by

$$\epsilon = 1 - (1 - OAR)^{\delta} \qquad (B1)$$

where OAR is the open area ratio of the MCP. This formula assumes that any electron striking a microchannel will give rise to a pulse. Typical open area ratios for MCP's are 0.60. Thus $\epsilon > .99$ if $\delta > 5$.

No data is available for the secondary emission coefficient for cesium ions with the energies of interest here. It also is assumed that the secondary emission coefficient for Cs^{++} ions is at least as large as for Cs^{+} ions. This assumption seems reasonable on the basis of a large electron affinity for Cs^{++} ions and the low velocities of the collisions involved here. There is some experimental evidence that the efficiency of these types of detectors is independent of the charge state of the incident ion.[47] We used oxidized aluminum sheet for the secondary electron emitter. It presumably has a secondary emission coefficient substantially larger than one for cesium ions. In addition, deposited cesium from the beam and from the plasma would tend to increase the secondary emission coefficient of any surface. Also the secondary emission coefficient is an averaged quantity with an

unknown distribution function. It is possible that some ions would liberate no secondary electrons. It is assumed that this contribution is negligible.

Initial tests of the detector were performed to check the effects of varying bias voltages on the noise and signal characteristics of the detector. A pulse height analyzer (PHA) was used to measure the spectrum of pulses due to noise alone and noise plus signals. A Bendix, type 3025-B, chevron MCP was initially used for the electron multiplier. However, its gain and operating characteristics were poor, presumably due to its age and poor handling conditions. The Varian MCP's were used for all subsequent tests and the actual experiment. It was found that satisfactory operation was obtained by biasing the input MCP electrode to -2000 volts and grounding the output electrode of the second plate. It was not necessary to fix the potential of the center electrode to an intermediate voltage. A potential of -2400 volts was applied to the secondary emission plate. This caused secondary electrons of approximately 400 eV energy to strike the input MCP. All bias voltages were plateaued to show that the count rate was independent of these voltages. Output pulses were detected on the anode (+200 volts) by capacitively coupling the anode to a charge sensitive pre-amplifier (LBL type 21X1701 P-1). This pre-amp had a conversion gain of 2.25×10^{10} volts/coulomb. The feedback capacitor was raised to 47 pf to avoid pre-amp saturation, and the feedback resistor was 2.2 megohm, giving an output time constant of approximately 100 microseconds. The output of pre-amp was fed into

a standard LBL amplifier (type IIX 5505 P-1) where the pulses were shaped to linear pulses for detection by oscilloscope, PHA or single channel analyzer (SCA) for counting. Typical pulse height spectrums are shown in Fig. 35.

It was decided to test the above hypotheses concerning the secondary emission coefficient by determining the absolute overall detector efficiency. The experimental arrangement for the test is shown in Fig. 36. The movable Faraday cup could be placed in front of the detector to measure the beam intensity incident on the detector. Secondary electrons from the Faraday cup were suppressed by the solenoidal field. As the smallest measurable current is about 1×10^{-14} amps corresponding to a count rate of 6.2×10^{4}, we had to attenuate the beam that was striking the detector. This was necessary in order to assure a low enough count rate that would not depress the gain of the MCP and hence the overall detector efficiency. A slit was used to attenuate the beam. The beam was collimated by two circular holes, C_1 and C_2 in Fig. 14, Chapter 5. A pair of steering plates after C_2 allowed the beam to be bent down to correct for the upward movement of the beam in the solenoidal magnetic field. The beam could be swept vertically past the slit and thus a beam current profile could be determined. The slit was located just in front of the secondary emission detector. Several slits were tried and the best one found was a 10 micron monochromator slit. It had a constant slit width along the length of the slit and was clean and free of jagged edges. The slit width also was measured under a microscope and found to be within 2

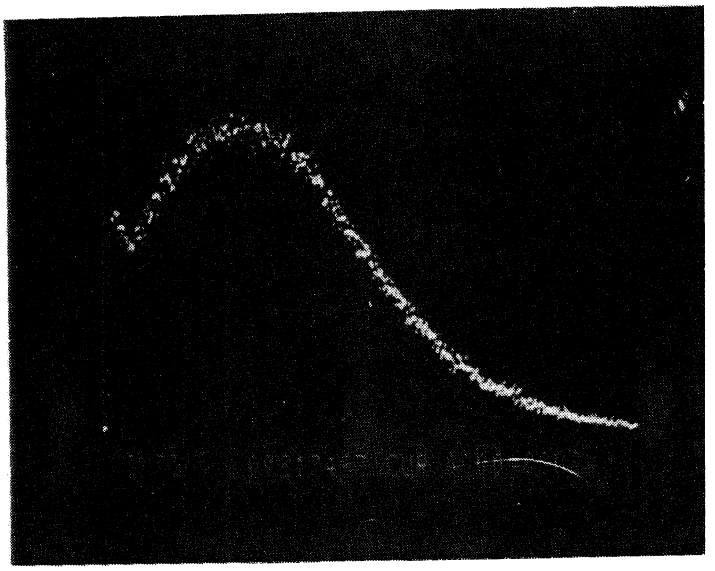

(a) with beam

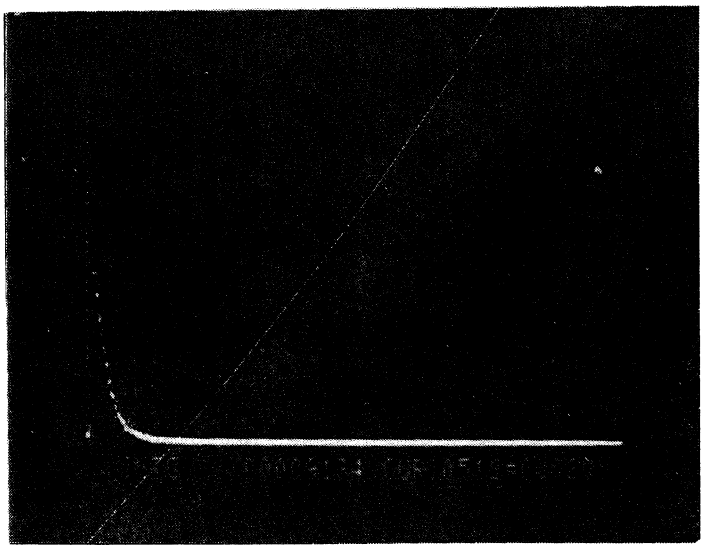

(b) without beam

XBB 825-4355

Figure 35. Typical pulse-height spectrum for the SED. Count rate was approximately 1000 counts/sec.

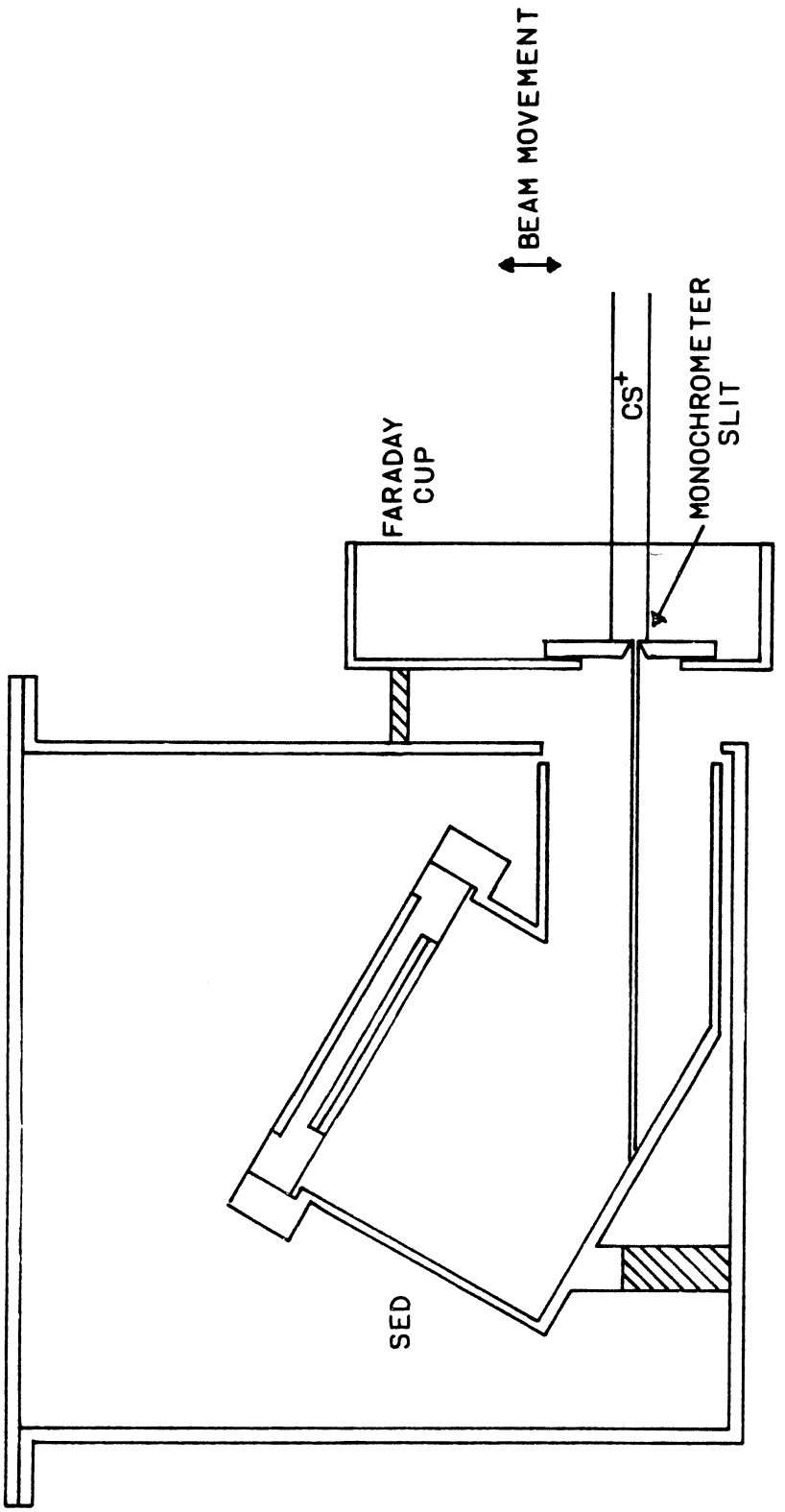

Figure 36. Experimental arrangement for determination of SED efficiency.

percent of the advertised width. A typical beam profile is shown in Fig. 37. Since the beam was circular and it was swept past the slit, the current to the secondary emission detector should vary parabolically as a function of steering plate voltage. The current density is determined by dividing the secondary emission detector counts by the area of the rectangle defined by the intersection of the slit and the beam spot. That is,

$$j = \frac{\dot{N}}{2a\sqrt{1 - \left(\frac{x}{a}\right)^2}\, dx} \qquad (B.2)$$

Where dx = slit width, a = beam radius, and x = position of the center of the beam relative to the slit, and $\dot{N}$ is the detected count rate.

It can be seen from Fig. 37 that the current density of the beam was uniform to within about 10 percent. The overall detector efficiency then is determined by the following formula,

$$\epsilon = \frac{j\ \pi\ a^2\ x\ 1.6\ x\ 10^{-19}}{I(amp)} \qquad (B.3)$$

where I is the total beam current measured in the Faraday cup.

The beam intensity was varied by changing the cesium ion source filament current. Thus, overall detector efficiency could be determined as a function of count rate. This is shown in Fig. 38. It is seen that the detector is 100 percent efficient within ± 15 percent up to a count rate of 2×10^4 counts/sec. Above this rate the detector efficiency drops monotonically, presumably due to the

Figure 37. Beam profile of incident beam. Solid line is a least squares fit to the equation $\alpha\sqrt{1-(\frac{X-\beta}{\gamma})^2}$. The solid squares represent the current density of the beam.

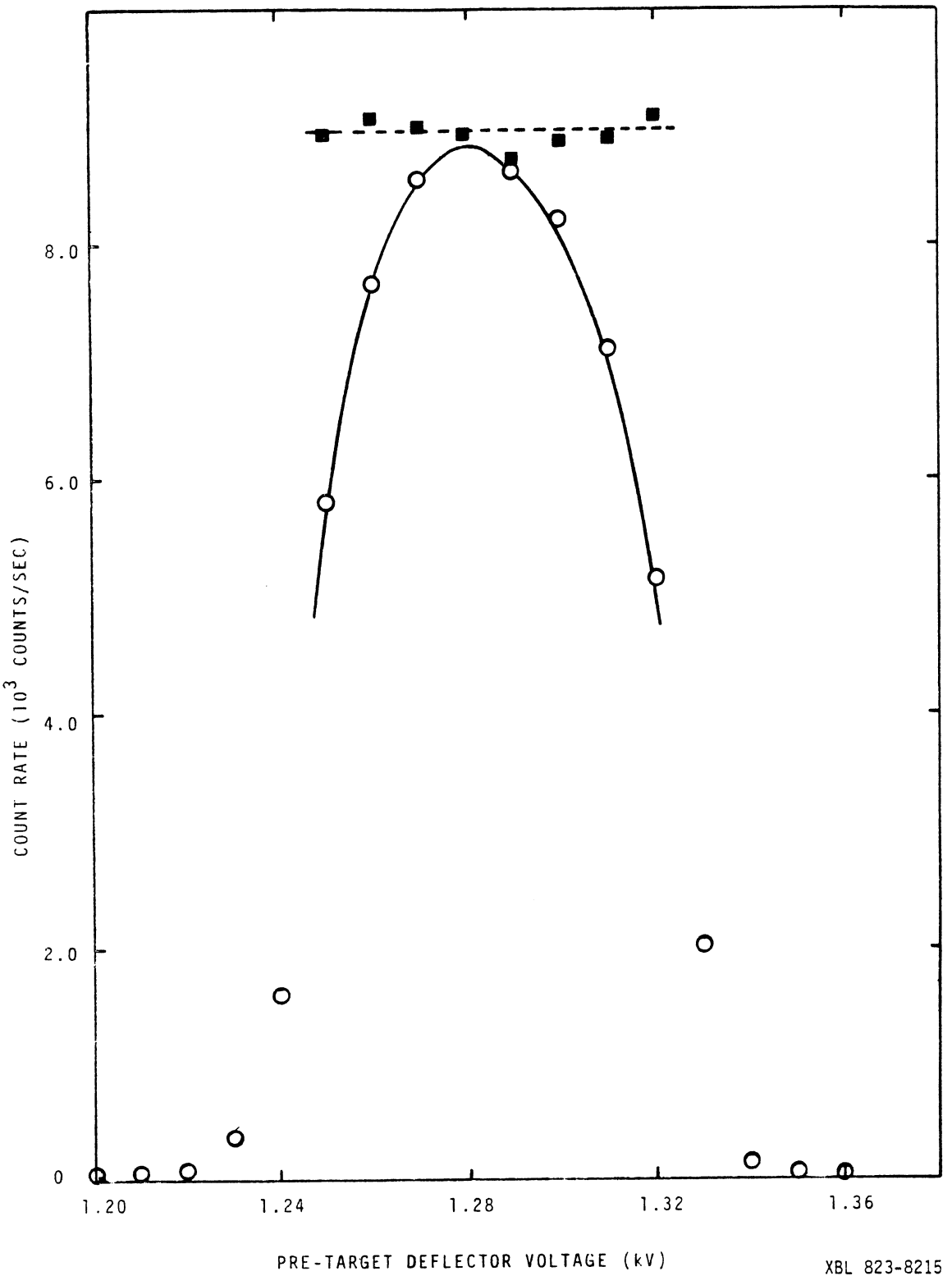
8.0
6.0
4.0
2.0
0
COUNT RATE (10^3 COUNTS/SEC)
1.20
1.24
1.28
1.32
1.36
PRE-TARGET DEFLECTOR VOLTAGE (kV)
XBL 823-8215

Figure 37

Figure 38. Count rate efficienty of the SED as a function of the incident beam current. Solid line shows 100 efficiency at count rates below 20,000 counts/sec and drops off at higher rates due to gain depression of the MCP.

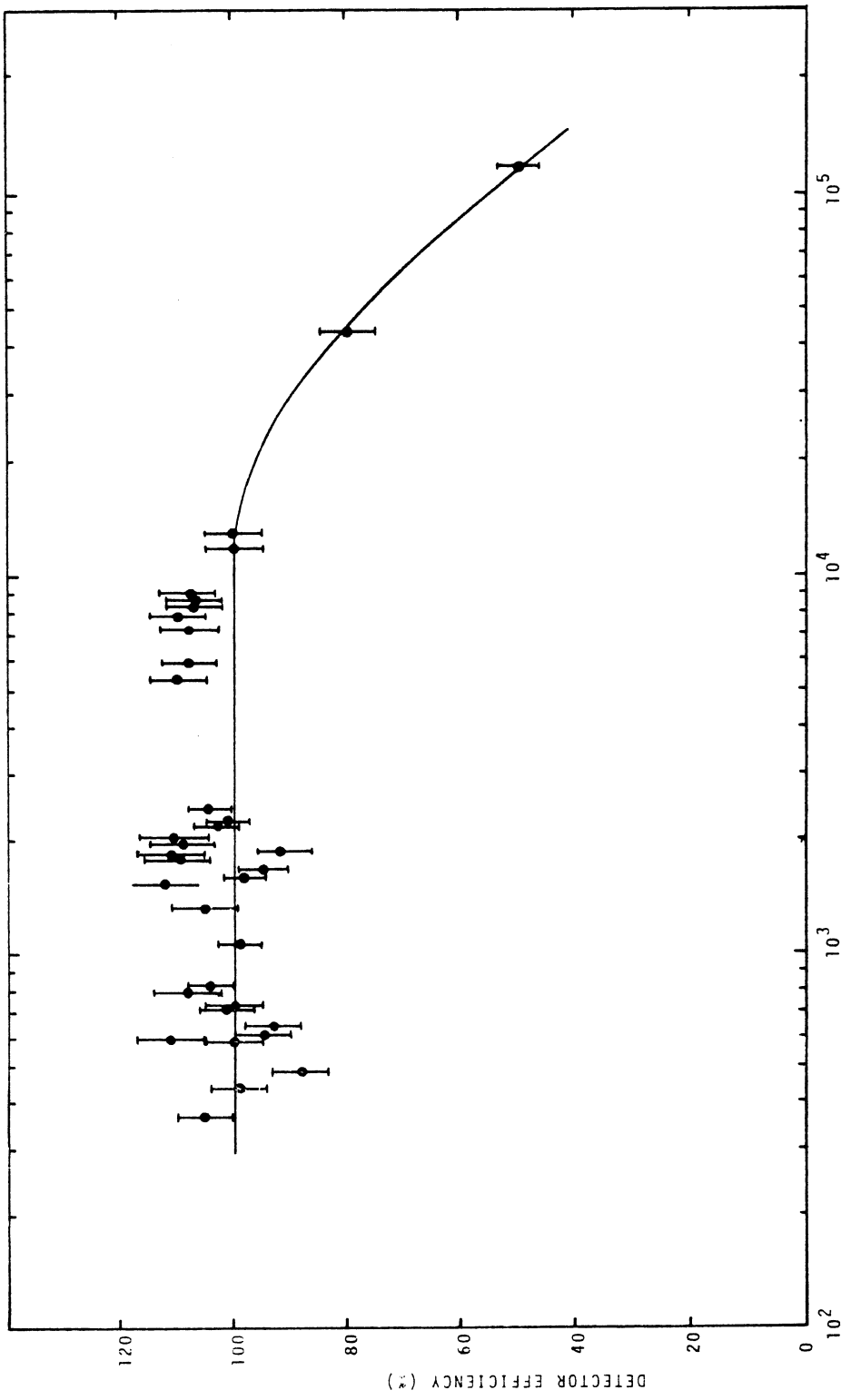
DETECTOR EFFICIENCY (%)
120
100
80
60
40
20
0
10^2
10^3
10^4
10^5
COUNT RATE (COUNTS/SEC)
XBL 823-8214

Figure 38

decreased MCP gain when the electron current in the microchannels becomes comparable to the strip current of the MCP.

The detector also was checked for the effect of the plasma on it. There was no effect due to the magnetic field. The magnetic field strength at the position of the detector was measured with a Hall probe to be approximately 25 gauss when the central solenoidal field strength was 2 kilogauss. The outer can was made of soft iron to attenuate this field even further. MCP's are known to be relatively insensitive to magnetic fields due to their small microchannel diameters.

The hot plate was turned on to check for any possible stray light effect on the detector. A slight periodic noise increase was found when the plasma chopper was rotating. It was guessed that this was due to light from the hot plate being periodically reflected toward the SED as the chopper rotated. A limiter, which had a hole of 3 inches diameter to pass the plasma, provided sufficiently good blocking of the periodically reflected light and eliminated this modulated noise problem.

The only effect on the noise of the detector was found to be gas pressure. The ambient analysis pressure was in the low 10^{-7} torr range, and the noise counts were very low here. As the cathode was heated the hot plate outgassed and caused the pressure to rise to as high as 10^{-5} torr. The noise was fairly significant at these high pressures. This is presumably due to ion feedback effects on the MCP operation. Under actual operating conditions the analysis chamber pressure usually was below 10^{-6} torr and no significant noise problems were found.

APPENDIX C

Cs^+ + Xe Experiments

A similar class of reactions to the Cs^+ + Cs^+ system could be studied without the aid of the plasma target. Since Cs^+ is electronically similar to Xenon, it was decided to try to measure Cs^{++} and Cs^0 production cross sections as well as the ionization of Xe in Cs^+ + Xe collisions. In addition, these cross sections were used to confirm detector collection efficiency and transmission efficiency of the entire plasma target-analysis chamber configuration. Initial experiments measuring Cs^{++} and Cs^0 formation and all experiments related to the ionization of Xe were carried out in another beamline of the accelerator system. An ionization gas cell of the parallel plate type was used for the initial experiments. The apparatus was described in detail by Berkner et. al.[50] for experiments looking at the ionization of rare-gas targets by high energy multi-charged ions. The results for the ionization of Xe by Cs^+ impact have been reported by Tanis et. al.[51] The ionization cross section is 1.8 x 10^{-15} cm^2 at 50 keV Cs^+ energy and rises slowly with energy to about 2.4 x 10^{-15} cm^2 at 150 keV. Previous work done on this system has been reported by Flaks et. al.[52,53] The agreement is not good if the trend of the two sets of data are compared. Unfortunately the range of energies for the two experiments do not overlap.

The data is shown in Fig. 39. Also shown are the final results for the cross section for production of Cs^{++} and Cs^0 in

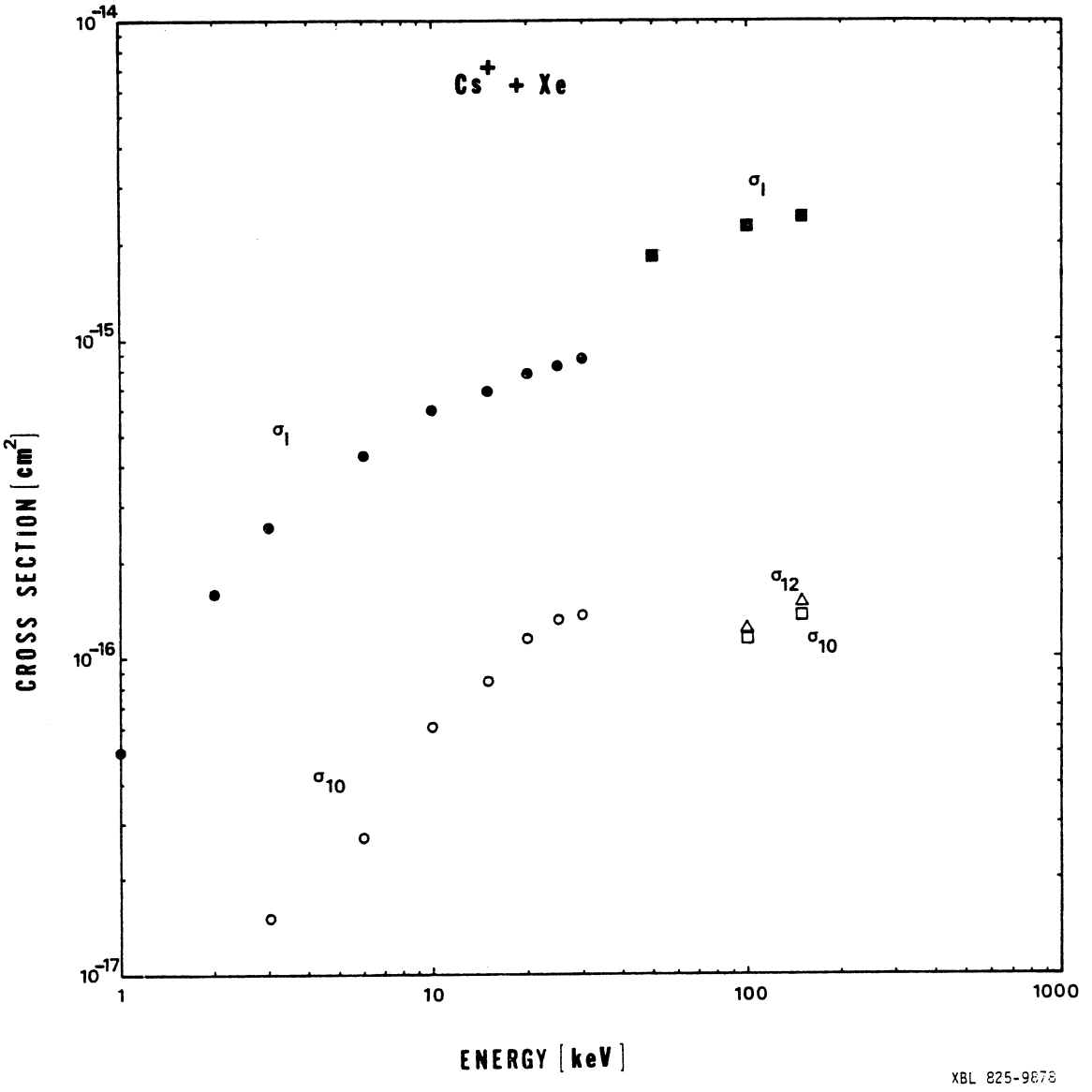

Figure 39. Experimental results for the Cs^+ + Xe experiments. ● - Ref. 52, O - Ref. 53, Δ,□,■, - Ref. 51.

collisions with Xe. Again the agreement with the data of Flaks et. al. is not good but the shift in the trend is opposite than in the ionization measurement.

Final measurements on the production of Cs^{++} and Cs^{0} were carried out in the one meter-diameter chamber which acted as part of the beamline for the plasma target experiment. The reasons for this change was that the scattering of the incident Cs^{+} ion beam in the original parallel plate gas cell was too severe to account for all of the beam. This is a neccesary condition for being able to measure projectile charge transfer and ionization cross sections. It was decided that a tighter geometry with a larger angular acceptance was neccesary to measure these cross sections. Therefore a gas cell was placed in the chamber and Faraday cups were used to measure the charged components of the exiting beam. A pyroelectric ceramic[54] was used to detect the Cs^{0} beam. The beam components were separated after the gas cell by a set of electrostatic deflection plates. Apertures in the gas cell were interchangeable and were large enough to pass the entire beam as it traversed the cell. The angular acceptance of the detectors was 3.2 degrees half angle measured from the center of the gas cell to the Faraday cups. Previous experiments done with gas cells of the type used for this phase of these experiments have been described by Morgan et. al.[55] The improved geometry was sufficient to collect all of the exiting beam. Both σ_{12} and σ_{10} were measured. The experiments were done at 100 keV and 150 keV Cs^{+} energies. The results also are shown in Fig. 39. The cross section for Cs^{++} formation is

1.2×10^{-16} cm^2 at 100 keV Cs^+ energy and 1.5×10^{-16} cm^2 at 150 keV Cs^+ energy. The cross section for neutralization of Cs^+ is slightly lower at the same energies but follows the same trend.

These results are discouraging when compared to the results of Flaks et. al. However if σ_{12} is plotted using the center of mass energy then the results are consistent with the measurement of σ_{12} with $Cs^+ + Cs^+$ reactions. We then can say that the $Cs^+ + Xe$ system should act similarly to the $Cs^+ + Cs^+$ system. No explanation presently exists for the discrepancy between the results of these experiments and the results of Flaks et al.

These cross sections were used to check transmission efficiency of the overall system and to check detector collection efficiency of the secondary emission detector. A movable gas cell was designed to simulate the presence of the plasma as far as collisions were concerned. Xenon was chosen as the working gas since the value of σ_{12} was known from the above experiments.

The gas cell is shown in Fig. 40. The geometrical length of the cell was 5 cm, corresponding to the radial size of the plasma. It was attached to a tube (0.75" O.D.) which was welded to a flange such that a capacitance manometer and a gas inlet connector could be attached to the tube. A small tube ran from the gas inlet connector to the bottom of the large tube near the gas cell. This insured that the gas cell and capacitance manometer were at the same pressure when the gas flow was steady. That is, no conductance corrections had to be made.

Figure 40. Movable gas cell used to simulate the presence of the plasma target.

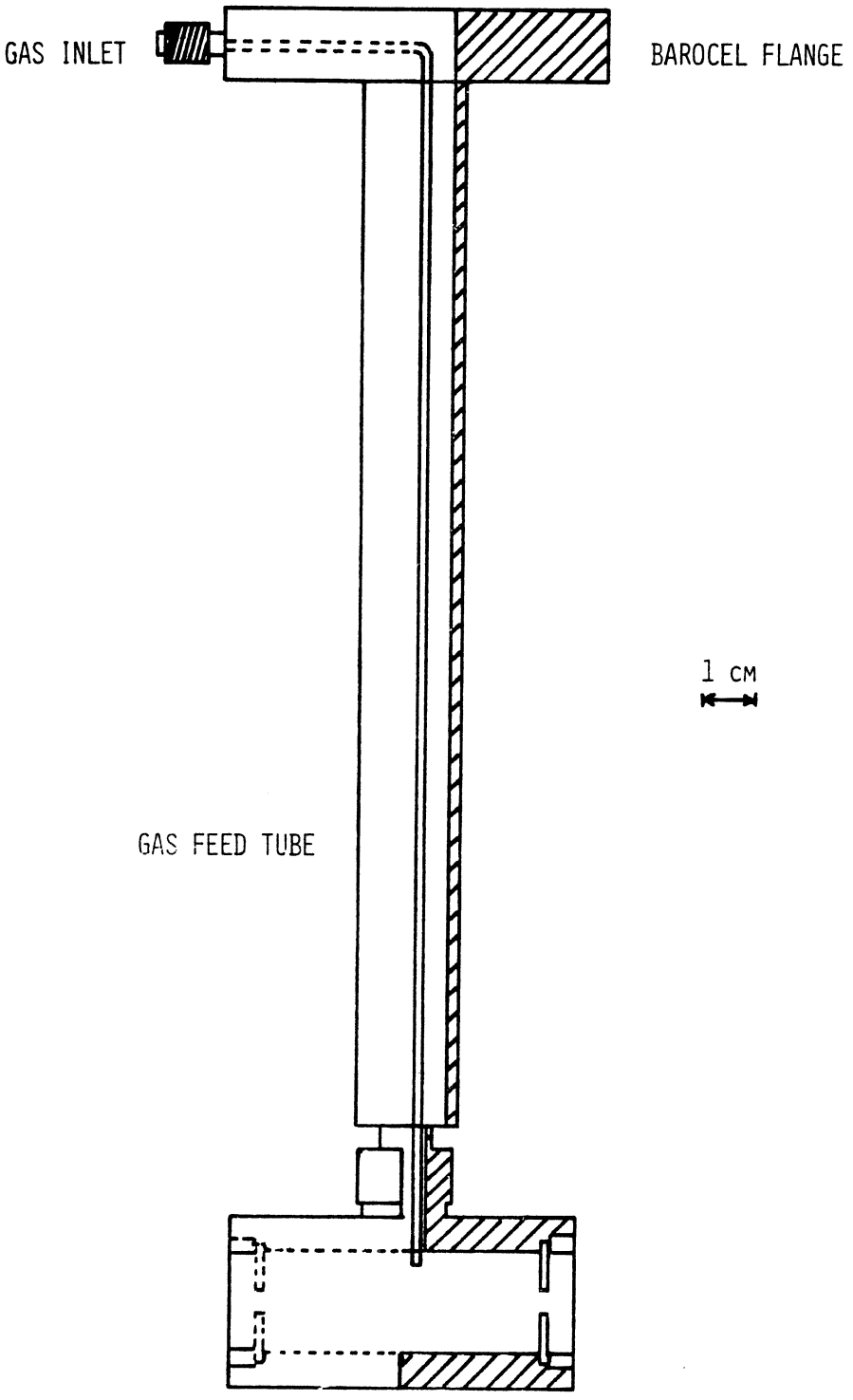
GAS INLET
BAROCEL FLANGE
1 CM
GAS FEED TUBE
MOVABLE GAS CELL
XBL 825-9871

Figure 40

The large diameter tube was mounted to a Wilson seal which allowed the gas cell to be moved vertically and also rotated. The flange with the Wilson seal was connected to the plasma vacuum chamber with a stainless steel bellows and there were four adjustment rods which allowed the gas cell to be tilted such as to allow for the upward movement of the beam in the magnetic field.

Alignment of the gas cell could not be done optically since the beam traveled in a curved path. Therefore all gas cell alignments were done by monitoring the incident ion beam current and moving the gas cell with the adjustment rods until the beam current was the same with and without the gas cell present. This was accomplished by tuning up a given energy beam and then dropping the gas cell approximately into position. Minor adjustments of the pre-target deflection plates and the magnetic field as well as the position of the gas cell was usually sufficient to let all of the beam get through the cell. The entrance aperture of the gas cell was 0.200" diameter and the exit aperature was 0.250" diameter. These aperatures were large enough to not interfere with the beam yet small enough to have a small conductance which allowed the gas in the cell to reach pressures measurable with the capacitance manometer.

The initial experiments with the movable gas cell were performed with 150 keV Cs^+ beams so as to compare with the experiments done earlier. The first trials were done with a detector array which was not similar to the final detector array in the actual plasma target experiments. Since the final detector array used a secondary

emission detector to detect Cs^{++}, it was decided to use this array in the gas cell experiments. Since the pressures in the target and analysis regions were too large to operate the SED in the normal mode when the gas cell was operating at the highest pressures, another way to detect Cs^{++} had to be devised. This was done by connecting all leads to the SED together and hooking an electrometer to the emitter electrode. Thus the SED could also be operated as a Faraday cup.

The beam was swept vertically past the gas cell with the aid of the pre-target deflector plates with and without Xenon in the gas cell. The Cs^{+} and Cs^{++} currents were monitored and the results are shown in Fig. 41. This showed that there was a plateau region for Cs^{++} detection which confirmed that fact that all Cs^{++} was being collected. Operating in the plateau region, the gas cell pressure was varied from zero to 5 millitorr. The Cs^{++} current was measured as a function of gas cell pressure. The fraction of the incident beam converted to Cs^{++} was computed from the equation

$$F^{++} = \frac{I_{Cs^{++}}/2}{I_{Cs^{+}(p=0)}} \qquad (C.1)$$

Where $I_{Cs^{+}(p=0)}$ is the incident beam current measured with zero gas pressure in the gas cell. The beam current was measured

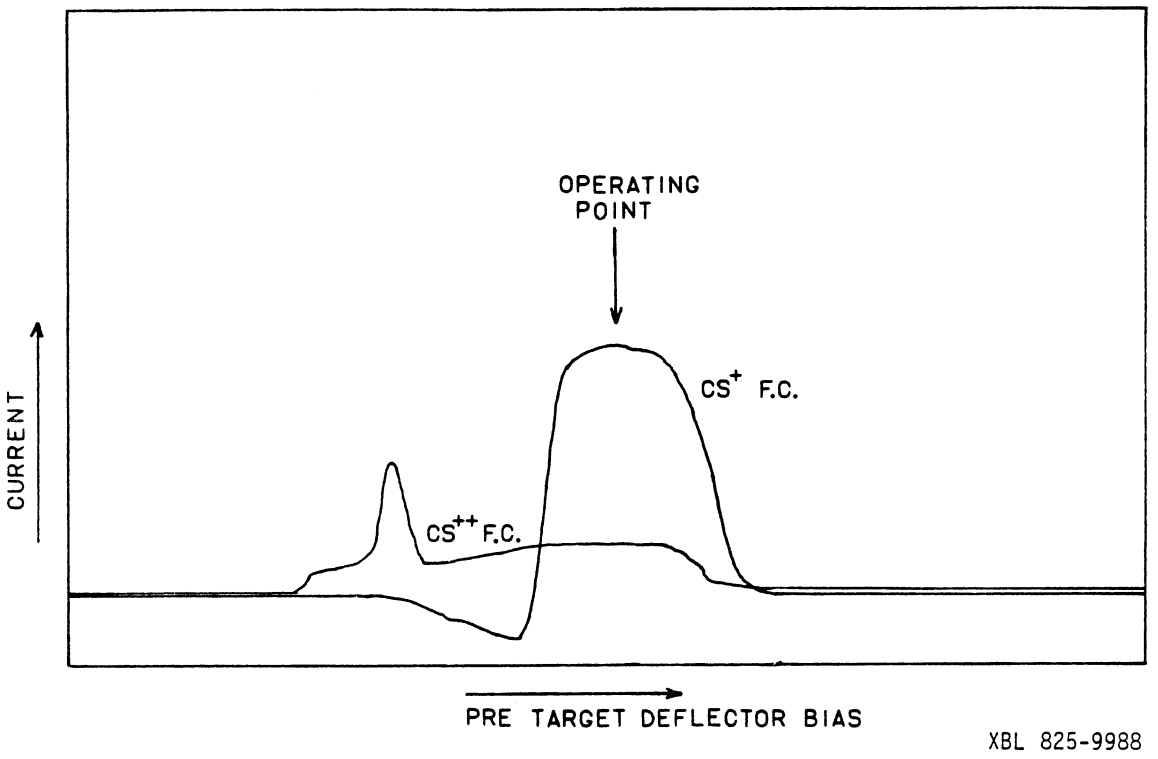

Figure 41. Beam currents as a function of pre-target deflector voltage. Note plateau region for Cs^{++} and Cs^{+} currents.

Figure 42. F^{++} fraction as a function of Xe gas pressure showing linear growth of the fraction for low pressures. Measured cross section is within 20 percent of the result measured in the original experiments.

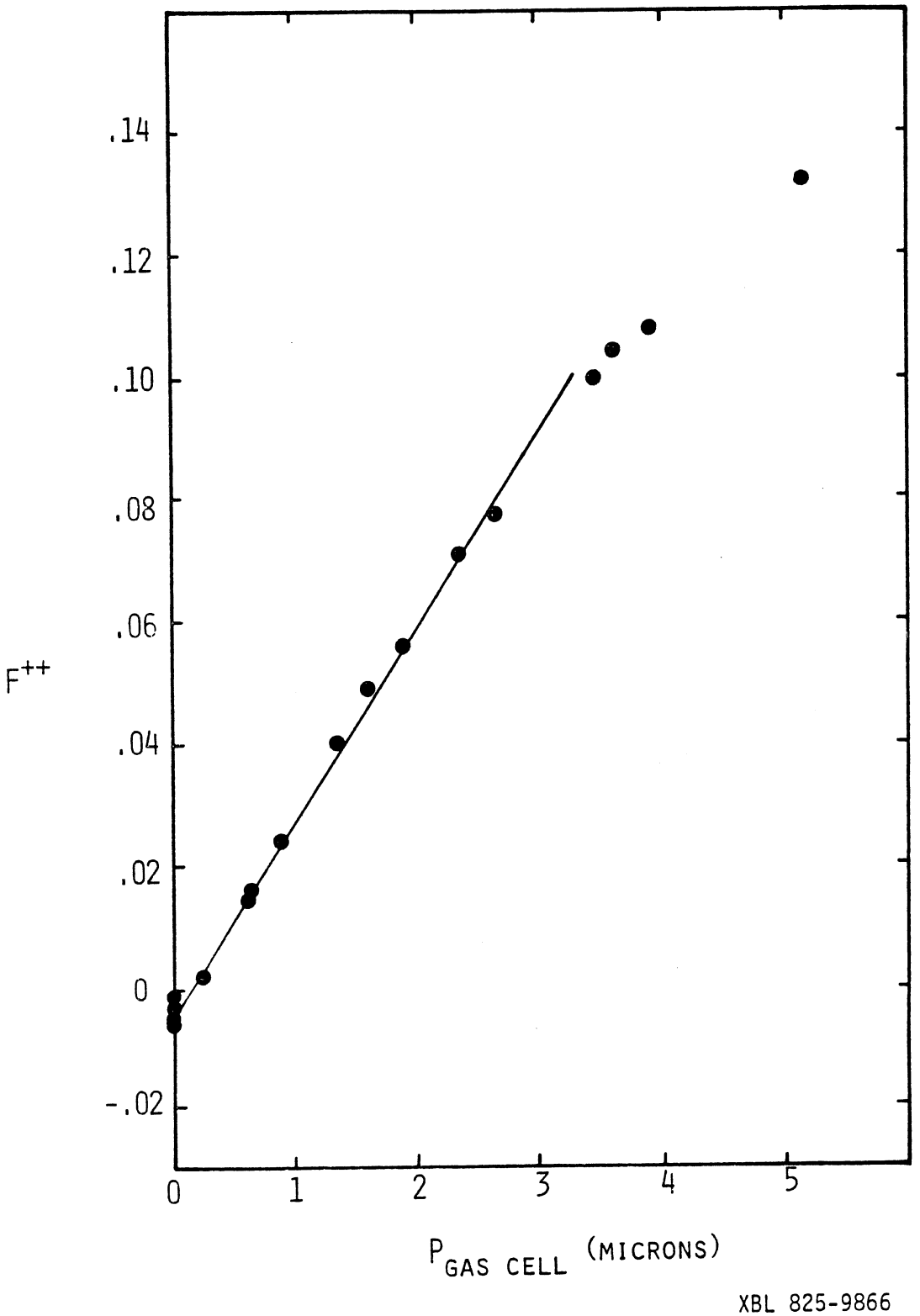

XBL 825-9866

Figure 42

frequently to confirm that the incident beam was constant. The results are shown in Fig. 42. The slope of the line is the cross section, σ_{12}. The value measured by this method agreed to within approximately 20 percent of the value measured with the separate gas cell experiments. This was decided to be sufficiently good agreement between the two results to assume that the detector array was working correctly for this energy beam (150 keV). The experiments were not repeated at lower energies, but it was assumed that all detector collection efficiencies and transmission efficiencies were the same using the properly scaled magnetic fields and pre-target deflector voltages.

Final tuning parameters for each energy were determined by tuning up the beam with the gas cell in place. Thus there was a unique set of tune parameters (magnetic field, deflector voltage) for each energy. This insured that the beam traversed the plasma on the same trajectory for each energy.

APPENDIX D

Beam Trajectory Calculations

Beam trajectories were calculated to make sure all beam components were collected. Since the magnetic field was nearly uniform inside the coils, but had an appreciable fringe component, a map of B_z vs r was measured in the plane of the beam fan. The measurements were done with a Hall probe. The results are shown in figure 35. This profile was used in conjunction with the equations of motion to confirm that the Cs^{++} and Cs^{+} components of the beam were separated enough at the detector to resolve them. A code was written which integrated the equations of motion when the initial beam energy, mass, charge state and divergence were given, collisions were allowed to take place along the trajectory where the plasma was located. Angular scattering effects could be accounted for.

The equations of motion for a charged particle in a magnetic field are described by the following equation:

$$m \frac{d^2 \underline{r}}{d t^2} = \frac{q}{c} \underline{V} \times \underline{B}, \qquad (D.1)$$

We assume $\underline{B} = B(x,y)\ z$

and $\underline{r}(t) = x(t)\ x + y(t)y$

Then, with the initial conditions given as

$$x(o) = x_o,\ y(o) = y_o$$

$$V_x(o) = V_{xo},\ V_y(o) = V_{yo}$$

The equations (D.1) were integrated numerically and x(t), y(t) were returned as output.

A typical result is shown in Fig. 43. This shows the envelope of the emerging beam. It can be seen that the Cs^{+} and Cs^{++} components of the existing beam were separated at the position of the detector. This lent confidence to the technique of using the plasma confining magnetic field for the beam separator.

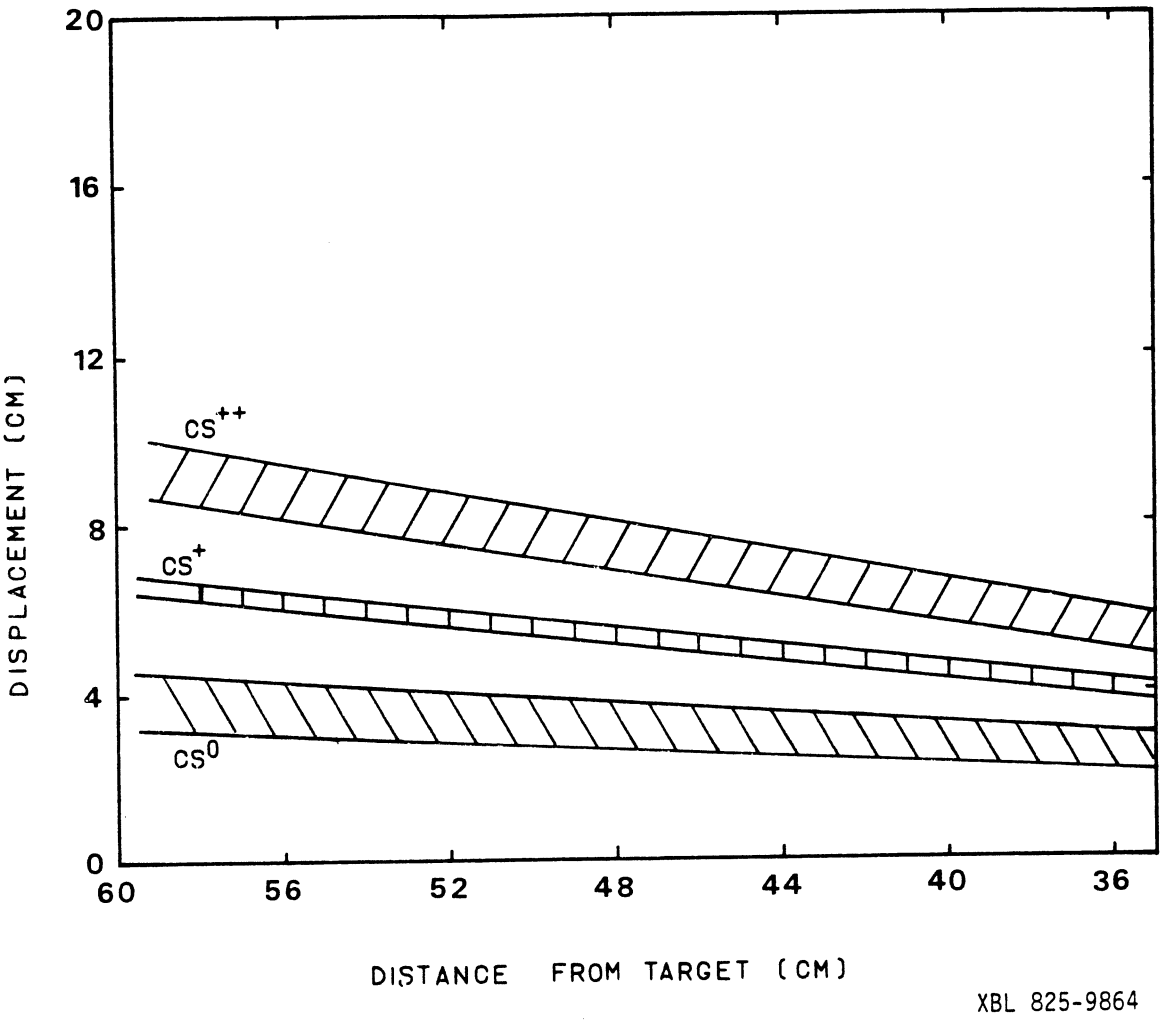

Figure 43. Calculated results for the trajectories of the beam components as the beam traverses the plasma target and hits the detector array.

APPENDIX E

Hot Plate Design

The plasma was formed at the hot plate by thermal ionization of cesium atoms and thermionic emission of electrons. This required the hot plate to be at a temperature of approximately 2800 K. The standard method for heating large areas to these temperatures is to use an electron bombardment arrangement. The design of this hot plate was based on the previous work of Laul et al.[56] A Lanthanum Hexaboride (LaB_6) cathode served as a source of electrons. This cathode was initially heated by electron bombardment from a tantalum filament. The procedure for heating the cathode to operating temperatures is described in Chapter 3. A drawing of the hot plate assembly is shown in figure 44.

The surface ionizer was made of 0.25" thick tunsten plate. It was 2" in diameter. This plate was held in a tantalum tube by four 0-80 moly screws. This assembly was bolted on to the entire hot plate assembly as shown in Fig. 44. Thus, the entire LaB_6 cathode and heater filament were enclosed by the tantalum hot plate holder. Power was supplied to the heater filament by two molybdenum rods (0.25" diameter) and the LaB_6 holder was supported by four molybdenum rods. These six rods were insulated from the stainless steel hot plate assembly by alumina tubes (I.D. = 0.25", length = 3") and the tubes were held in place by two stainless steel support blocks which were adjustable by eight set screws in the stainless steel hot plate assembly.

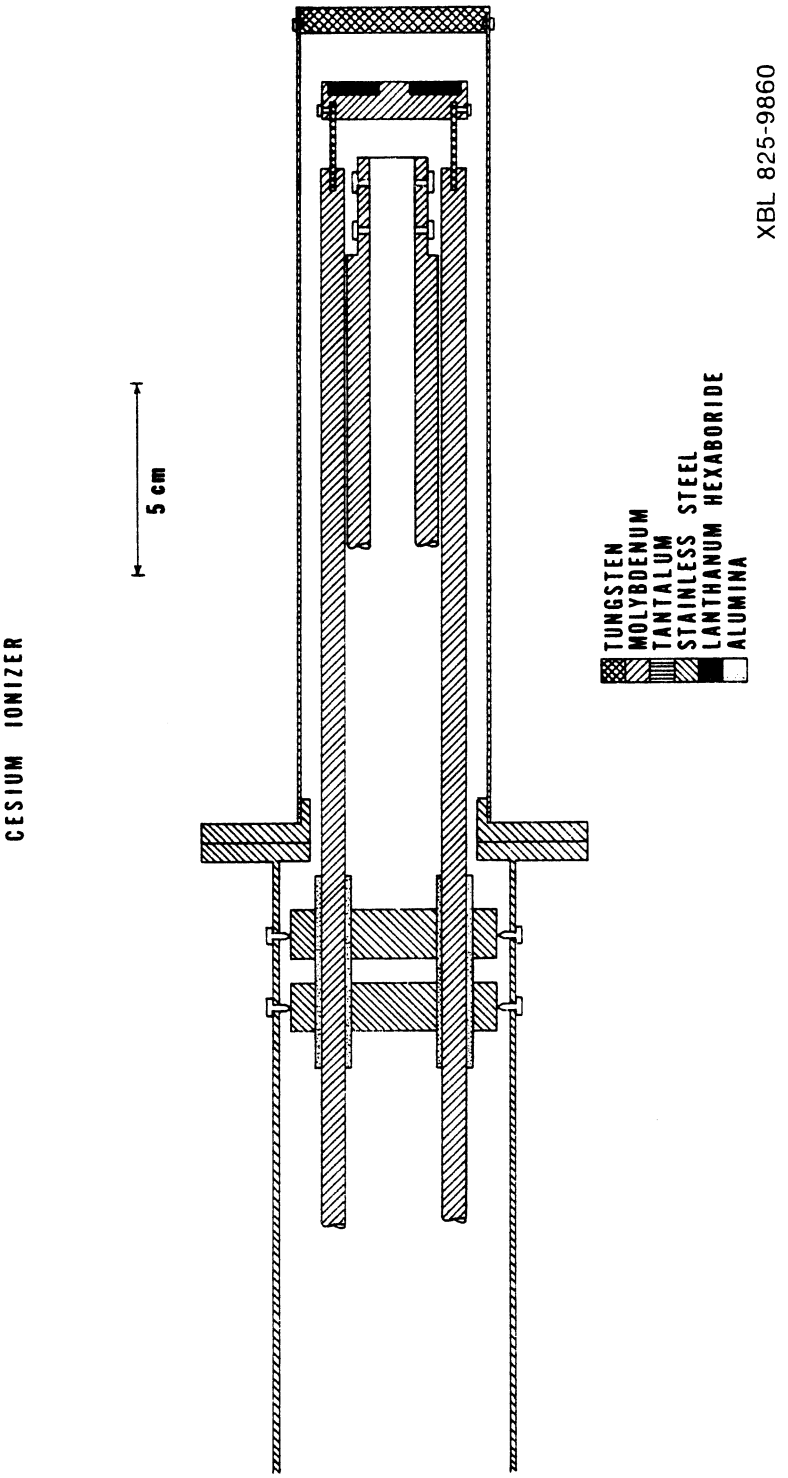
CESIUM IONIZER
5 cm
TUNGSTEN
MOLYBDENUM
TANTALUM
STAINLESS STEEL
LANTHANUM HEXABORIDE
ALUMINA
XBL 825-9860

Figure 44

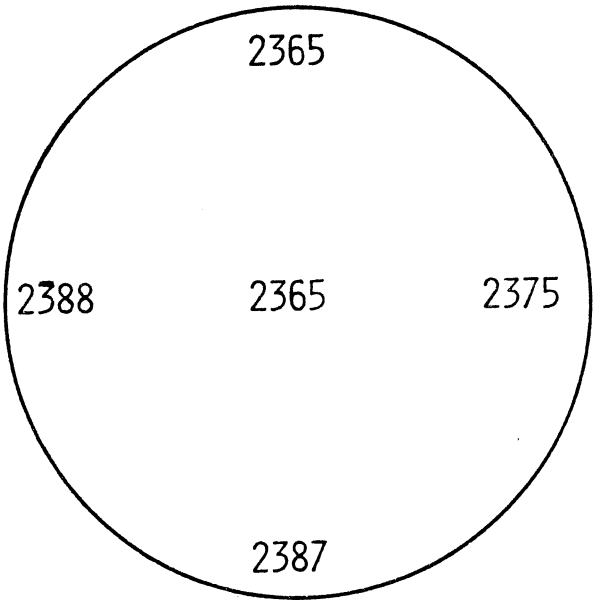

HOT PLATE TEMPERATURE DISTRIBUTION (K)

XBL 823-8719

Figure 45. Low power temperature variation over the surface of the tungsten hot plate.

A minor improvement of Laul's basic design was made on the molydenum LaB_6 holder. Laul used a grooved molybdenum block which had a LaB_6 slurry pasted into the grooves. This was chosen as the first design for this hot plate, but was later improved such that a solid sintered LaB_6 disk could be held by the molybdenum block. This avoided long bakeout periods of the LaB_6 slurry and also provided a larger and more uniform emissive surface. The molybdenum LaB_6 holder originally had a hole in the center of it for axial beam injection. One tungsten hot plate also had a 0.200" hole in the center for this purpose. The axial beam injection method was eventually abondoned and the tungsten hot plate was replaced by a new hot plate with no hole. The molybdenum LaB_6 holder was left alone and thus had a hole in it. No adverse effects were noted on the plasma profile most of the time. The cathode design was intentionally azimuthally symmetric which minizes $\underline{E}x\underline{B}$ radial plasma drifts. Radial temperature varations only lead to azimuthal drifts.

Temperature uniformity of the tungsten hot plate was measured with an optical pyrometer. Typical low power temperature measurements on the surface of the tungsten hot plate are shown in Fig. 45. The uncertainty is estimated to be ± 5K.

APPENDIX F

Other Applications of Plasma Targets

Initially it was thought that the Q machine plasma target might be useful to study other ion-ion collisions. In particular, the study of D^- collisional detachment processes in plasmas is of importance to the production of intense neutral beams for magnetic confinement plasma heating.

All neutral beam heating systems on present day magnetic confinement experiments are based on positive ions. The positive ions are accelerated from a plasma source and neutralized in a gas cell neutralizer by charge exchange reactions. The efficiency of this neutralization process drops off rather drastically with energy above about 200 keV D energy. Future magnetic confinement schemes may require higher energy neutral beams and the most efficient way to produce these would be to start with negative ions and then strip the electron off the ion after acceleration. Currently work is being done to find the most efficient way to produce enough D^- ions for a practical ion source.[57] Any improvement in the neutralization efficiency is important for the overall system efficiency and plasma targets are a candidate for a useful neutralizer.

The production and neutralization of intense D^- beams have been the topic of several conferences.[58,59] All system components have been discussed in these proceedings. Neutralizers based on plasma targets have been a topic of interest for several years.

Some experimental work has been done in recent years to look at the problems of these targets.

Riviere and Sweetman[60] were the first to propose the use of plasma targets for D^- neutralizers. Due to the Coulomb interaction of the plasma ions and electrons with the D^- ions, enhanced neutralization efficiencies of 85 percent were calculated on the basis of known cross sections. The optimum target thickness for the plasma target would be around 10^{15} cm^{-2}. This is substantially better than the 60 percent optimum neutralization efficiency for gas targets.

Some initial experimental work on plasma neutralizers performed at Novosibirsk[61] confirmed the enhanced neutralization efficiencies for pulsed lithium and magnesium conical plasma guns. More recently, Savas[62] has studied the neutralization efficiency for D^- beams in a pulsed, hot cathode hydrogen discharge. Unfortunately the plasma target thickness was too low to obtain optimum yields and the maximum reported neutral yield was approximately 45 percent, limited by detector performance. Yields of 78 percent were postulated on the basis of the maximum plasma line density.

Previous plasma neutralizer experiments suffered from several inconveniences which limit the actual practibility of any upgraded version. These include, 1) pulsed operation. Practical neutralizers would need to run in a steady state mode if the D^- beams were run steady state. 2) Confinement fields for the plasma cause the beam to diverge rather drasically and this would be bad

for neutral beam systems where the source and neutralizer are fairly far from the beam injection port on the magnetic confinement device.

Useful plasma neturalizers would run quasi-steady state (several seconds) and preferably would be largely free of magnetic fields which adversly affect beam quality. Is should be mentioned that photodetachment of D^- beams offer the potential for even greater neutralization efficiencies with minimal effects on beam steering. Of course the question of steady state operation of intense lasers has to be addressed.

After initiation of the experiment to determine $Cs^+ + Cs^+$ collision cross section it was thought that the Q Machine might also be a useful tool for studying D^- detachment processes. The initial idea for the target had the incident beam shot down the axis of the plasma, along the magnetic field.

This approach proved not to be useful due to several reasons. First, angular scattering made the axial injection method a poor choice since the beam could not be separated sufficiently well after the target to resolve the different charge states of the beam. Second, outgassing of the cathode could not be alleviated to such an extent as to guarantee the purity of the incident beam which was to cross the plasma target. Third, some steering of the beam inside the cathode due to the electron bombardment system for heating the cathode proved to be deleterious to axial injection.

Thus it was decided to turn the plasma target 90 degrees to allow for perpendicular injection of the beam. This was the final geometry for all plasma target studies. Unfortunately, this

Figure 46. Plasma profiles for various magnetic fields.
(a) B=2.7 kG, (b) B=2.4 kG, (c) B=2.1 kG (d) B=1.8 kG.
(e) B=1.6 kG, (f) B=1.3 kG, (g) B=1.0 kG (h) B=0.7 kG.

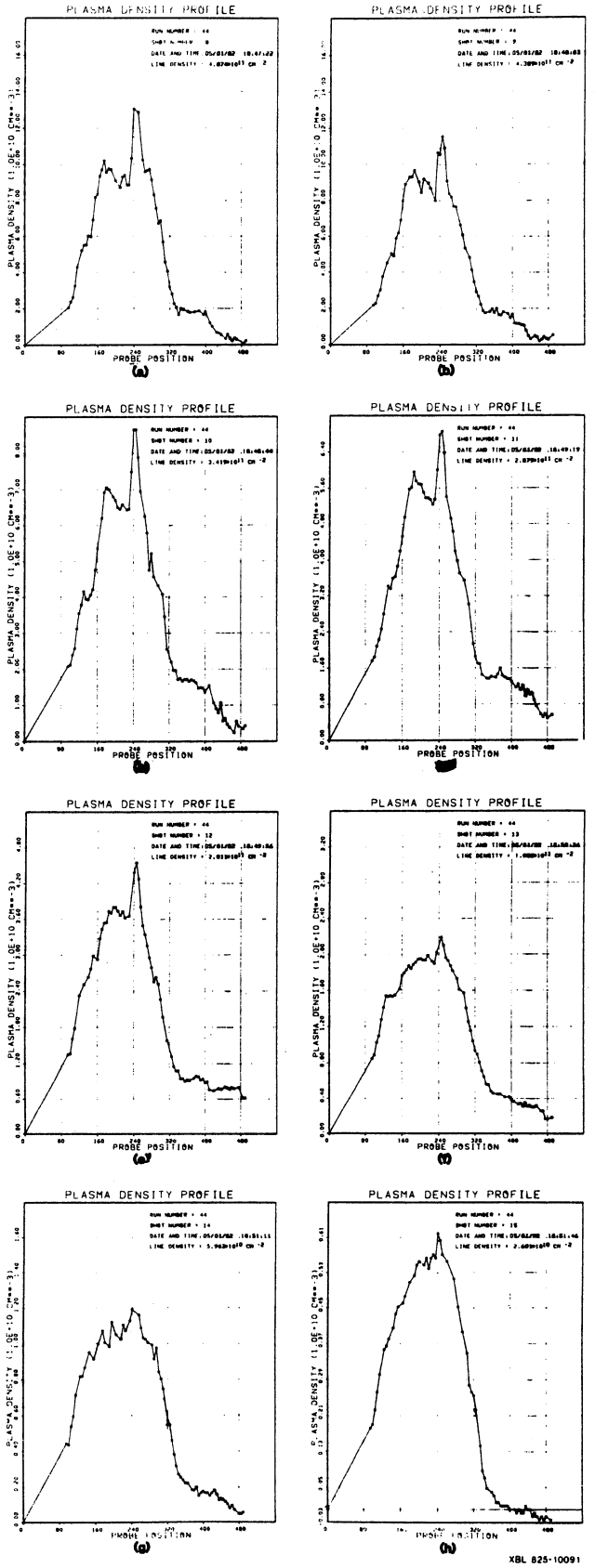
PLASMA DENSITY PROFILE
PLASMA DENSITY (1.0E+10 CM**-3)
PROBE POSITION
(a)
PLASMA DENSITY PROFILE
PLASMA DENSITY (1.0E+10 CM**-3)
PROBE POSITION
(b)
PLASMA DENSITY PROFILE
PLASMA DENSITY (1.0E+10 CM**-3)
PROBE POSITION
(c)
PLASMA DENSITY PROFILE
PLASMA DENSITY (1.0E+10 CM**-3)
PROBE POSITION
(d)
PLASMA DENSITY PROFILE
PLASMA DENSITY (1.0E+10 CM**-3)
PROBE POSITION
(e)
PLASMA DENSITY PROFILE
PLASMA DENSITY (1.0E+10 CM**-3)
PROBE POSITION
(f)
PLASMA DENSITY PROFILE
PLASMA DENSITY (1.0E+10 CM**-3)
PROBE POSITION
(g)
PLASMA DENSITY PROFILE
PLASMA DENSITY (1.0E+10 CM**-3)
PROBE POSITION
(h)
XBL 825-10091

Figure 46

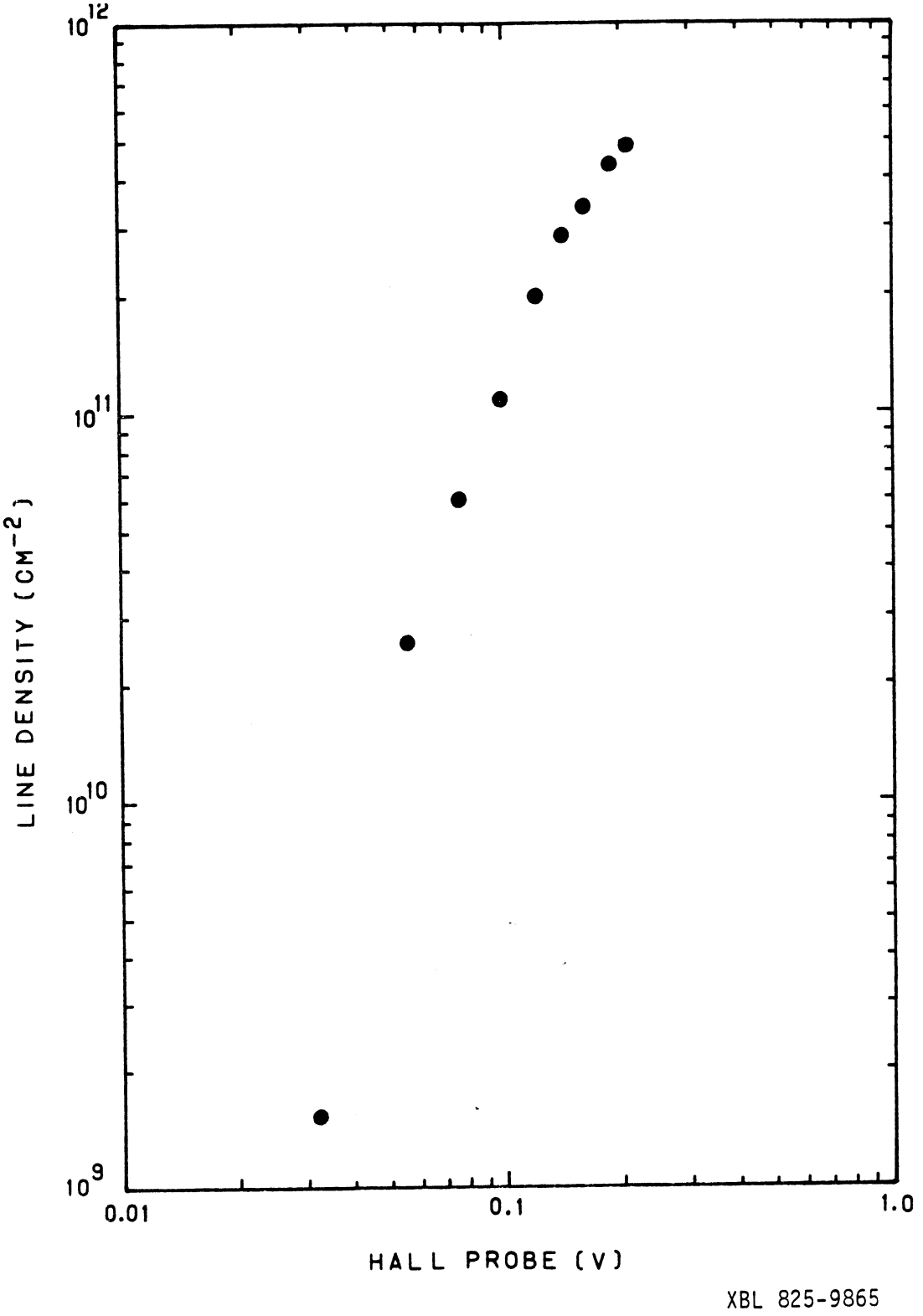

Figure 47. Integrated radial line density vs B. 1 volt = 13 k Gauss.

geometry proved to be bad for D^- detachment studies since the magnetic confinement field used for separating the charge states of the beam was too strong and the radius of curvature of the relatively light deuterium ions was too small to get the beam out of the plasma target chamber and into the analysis chamber for detection. The experiment was successful for incident cesium ions because the deflection of these heavy ions was small enough to get the entire beam envelope into the analysis chamber.

Some experiments were performed to see if the plasma would operate well with fields substantially lower than usual. The usual field strength for the cesium beam experiments was about 3 kgauss. A field strength of 400 gauss would be sufficient to analyze a 250 keV deuterium beam. Initial runs at the low fields were plauged by poor cathode alignment which led to poor operation of the hot plate. Electrons from the LaB_6 were not aimed correctly at the hot plate, so the space charge of the electrons caused the hot plate temperature to lower significantly and this reduced the plasma density to very low values.

Upon a more careful alignment to the cathode, it was possible to study the behavior of the plasma over a farily wide range of magnetic fields. One run was made to study the effects of changing magnetic fields on plasma profile and integrated radial line density. The results are shown in Fig. 46. The plasma in this case was fairly peaked in density. This presumably was due to a slight misalignment of the cathode and/or a hot spot on the tungsten surface. As the field was lowered from 2.6 kgauss, the peak density

became lower and the integrated radial line density became lower. The radial line density as a function of magnetic field is shown in Fig. 47. the electron bombardment power was held constant in this experiment, so the hot plate temperature presumably was constant as the field was changed. The hot plate temperature was not measured however. The line density is a strong function of magnetic field. Since the hot plate temperature was fixed, the ionization probability was fixed and therefore the electron emission from the hot plate had to be drastically reduced. This could only happen if the plasma potential became more negative, thereby inhibiting electron emission. This was confirmed by observing the floating potential at the peak in the density profile as a function of field strength. As the field was lowered the floating potential, and hence the plasma potential became more negative. This explains why the plasma density was so small for low fields. Physically, the lower fields resulted in poorer radial ion confinement. More ions were lost to the wall (or limiter) and this caused the plasma potential to drop. The cathode operated well in magnetic fields as low as 400 gauss. Below this field, the cathode drew too much current, probably due to increased anode area at the lower fields.

It was not deemed appropriate to try to run the plasma in a mirror configuration. This might be thought to be a better configuration, since the D^- beam conceivably could be injected in the low field region while the ionizer could be run in the high field region. The reason for this is that in the low field region,

enhanced radial ion loss would tend to lower the plasma potential there. Since the parallel electron conductivity is large, this would directly affect the plasma potential and sheath near the hot plate ionizer. Thus the electron emission from the hot plate would be inhibited, resulting in lower plasma densities. No attempt was made to run the plasma with lighter ions such as lithium which would have run better with the low fields.